Investigating the Density Dependence of the Nuclear Symmetry Energy using Heavy Ion Collisions

Simon Gannon

Thesis submitted in acccordance with the requirements of the
University of Liverpool for the degree of
Doctor in Philosophy

August 3, 2017

Abstract

A topic of fundamental importance and much current interest in nuclear physics is the determination of the equation of state for asymmetric nuclear matter. Determining the equation of state is indeed essential for understanding many problems in nuclear physics and a range of phenomena and processes in astrophysics, including neutrons stars, supernovae, and nucleosynthesis in high-mass stars.

Directed and elliptic flows of neutrons and light charged particles were measured for the reaction ^{197}Au $+^{197}$ Au at 400AMeV incident energy within the ASY-EOS experimental campaign at the GSI laboratory in Darmstadt (Germany). This reaction system was shown to probe densities in excess of double the nuclear saturation density. The experimental apparatus consisted of the Large Area Neutron Detector LAND, 8 rings of the CHIMERA multidetector, the ALADIN Time-of-Flight Wall, and the MICROBALL array. The last three detector systems were used for event selection and determination of the impact parameter and reaction plane for each event. The KRATTA triple telescope array was also used to measure isotopic composition and flows of light charged particles.

The elliptic flow of neutrons and hydrogen isotopes was extracted and the experimental ratio v_2^n/v_2^{Ch} was compared against predictions of the modified UrQMD transport model. The value of the power law coefficient, $\gamma = 0.72 \pm 0.19$, which describes the density dependence of the nuclear symmetry energy was de-

termined from a linear interpolation between the model predictions for values of $\gamma = 0.5$ and $\gamma = 1.5$. This measurement represents a new and more stringent experimental constraint on the strength of the symmetry energy at supra-saturation densities. It is consistent with the previous value extracted from an earlier FOPI-LAND experiment, but has achieved considerably smaller uncertainties. This measurement favours a moderately soft to linear density dependence of the nuclear symmetry energy.

Acknowledgement

I wish to thank the Science and Technology Facilities Council (STFC) for their financial support and my supervisors Prof. Marielle Chartier, Dr. Roy Lemmon, and Dr. David Joss for their guidance, support and understanding during the course of my PhD. I would also like to thank Dr. Paolo Russotto and Prof. Wolfgang Trautmann for their invaluable assistance with my analysis of the ASY-EOS data and Janet Sampson for helping me with computing problems. Special thanks to Emily, Matthew, Diane and John Cunliffe (and their chocoholic poodle Timmy) for allowing me the use of their home to finish writing my thesis. Finally, my thanks go to my family for their continued support and encouragement throughout my education and PhD.

Contents

1 Introduction

A topic of fundamental importance in nuclear physics is the determination of the Equation of State for Asymmetric Nuclear matter. Determining the equation of state is essential for understanding many problems in nuclear physics and a range of phenomena and processes in astrophysics including neutrons stars, supernovae, and nucleosynthesis in high mass stars. The ASY-EOS experiment [1] was conceived to place tighter experimental constraints on the strength of the symmetry energy at supra-saturation densities.

1.1 The Symmetry Energy and the Nuclear Equation of State

The nuclear Equation of State (EOS) describes the relationship between the energy, pressure, temperature, density and isospin asymmetry of nuclear matter [1]. The equation of state is made up of a symmetric component which is independent of isospin asymmetry, $\frac{E}{A}(\rho, 0)$, where ρ is the density of nuclear matter, and an asymmetric component which is related to the square of the isospin asymmetry, δ and the value of the nuclear symmetry energy, E_{sym}, [2] [3] [4]:

$$\frac{E}{A}(\rho, \delta) = \frac{E}{A}(\rho, 0) + \delta^2 E_{sym}(\rho) \tag{1.1}$$

After several decades of experimental measurements constraints have been placed on the symmetric component of the equation of state for densities up to 4.5 times the saturation density [5], see Figure 1.1.1, although it can be seen in Figure 1.1.1 that there are still several different theoretical symmetric equations of state which are consistent with the experimental constraints.

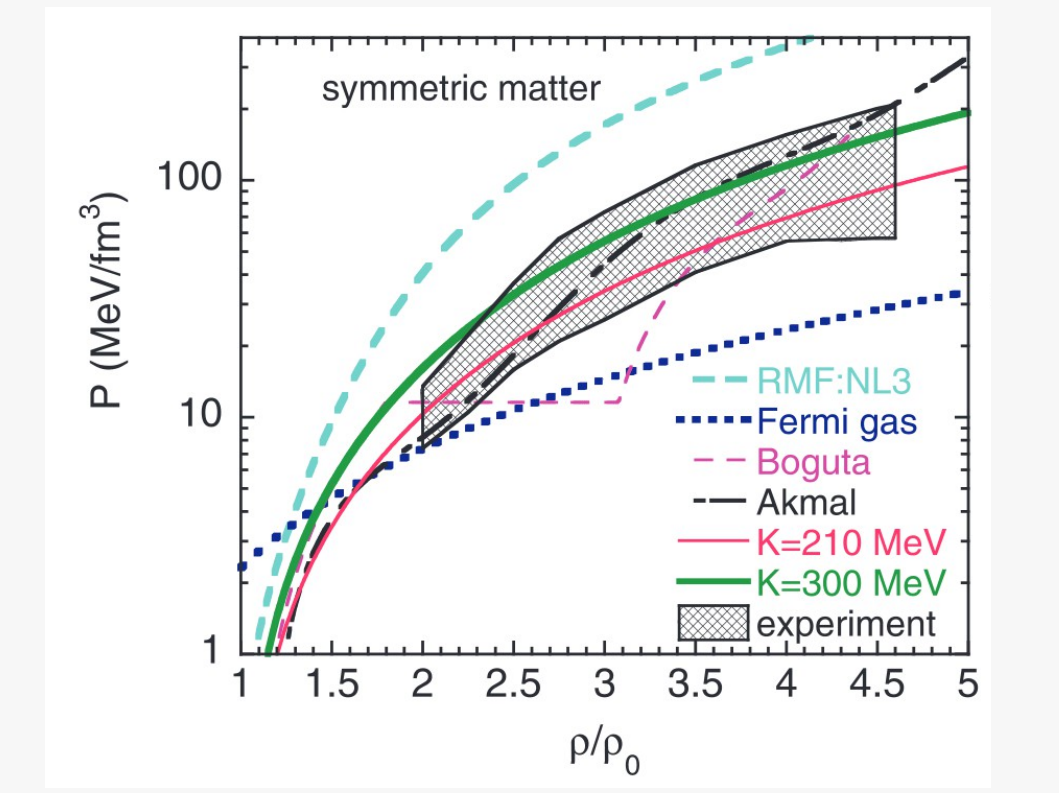

Figure 1.1.1: Figure adapted from [5]. The plot shows the experimental constraints from flow data on the zero temperature symmetric component of the symmetric nuclear equation of state from saturation density up to 4.5 times saturation density. Also shown are the theoretical predictions of various symmetric equations of state. P is the central pressure in the heavy ion collisions ($1\text{MeV/fm}^3 = 1.6 \times 10^{32}$ Pa).

Asymmetric nuclear matter refers to nuclear matter which contains unequal numbers of protons and neutrons. The degree of asymmetry is parameterized by the isospin asymmetry (δ) which is expressed by:

$$\delta = \frac{\rho_n - \rho_p}{\rho_n + \rho_p} \tag{1.2}$$

Isospin asymmetry can also be defined for an atomic nucleus as:

$$\delta = \frac{N - Z}{A} \tag{1.3}$$

where ρ_n and ρ_p refer to the density of neutrons and protons in the nuclear matter, respectively. The alternative definition in equation 1.3 can only be used for an atomic nucleus and uses the neutron number, N, proton number, Z, and the nucleon number, A.

The symmetry energy, $E_{sym}(\rho)$, can be defined as the difference between the binding energies of symmetric nuclear matter and pure neutron matter. The density dependence of the nuclear symmetry energy can be characterized in different ways:

$$E_{sym}(\rho) = S_v + \frac{L}{3}(\frac{\rho - \rho_0}{\rho_0}) + \frac{K_{sym}}{18}(\frac{\rho - \rho_0}{\rho_0})^2 \tag{1.4}$$

In this formulation the quantities L and K_{sym} are used to characterize the density dependence of the symmetry energy. L is the slope parameter and K_{sym} is the curvature parameter. The saturation density is $\rho_0 = 0.16$ fm^{-3} and is equal to the density found in atomic nuclei. These parameters are related to several features of nuclei and nuclear matter. S_v is the value of the symmetry energy at saturation density. Figure 1.1.2 shows existing experimental constraints on the values of S_v and L.

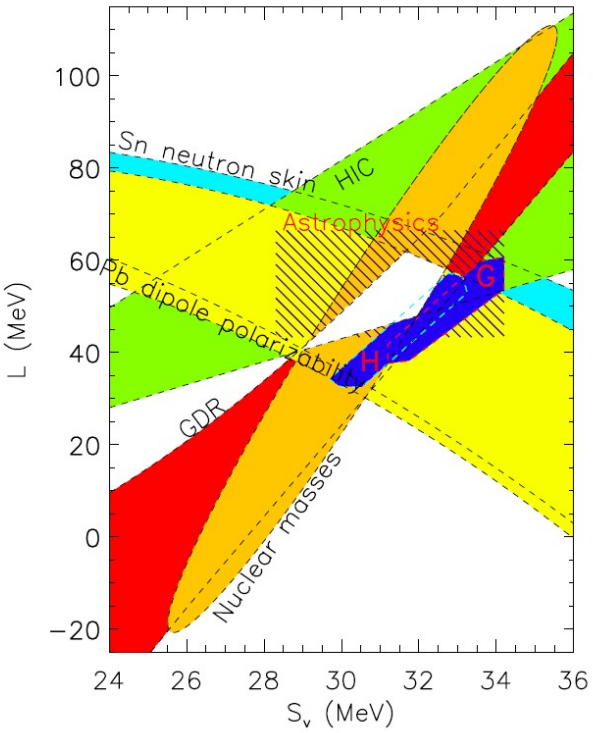

Figure 1.1.2: Adapted from [6]. Figure shows constraints on the S_v and L parameters of the symmetry energy. The orange region is from [7], blue band [8], yellow band [9], red area [10], and the green region is from isotope diffusion in heavy-ion collisions [11]. The hatched region is from mass and radius observations of neutron stars [12] [13]. The blue regions marked H [14] and G [15] are from neutron-matter constraints.

Another parametrisation of the symmetry energy uses a power law and can be expressed as:

$$E_{sym}(\rho) = E_{sym}^{pot} + E_{sym}^{kin} = 22\text{MeV}(\frac{\rho}{\rho_0})^{\gamma} + 12\text{MeV}(\frac{\rho}{\rho_0})^{\frac{2}{3}} \tag{1.5}$$

E_{sym}^{pot} and E_{sym}^{kin} are the potential and kinetic contributions to the total value of the symmetry energy. A high value of γ means that the symmetry energy increases strongly with density, this is referred to as a "stiff" symmetry energy ($\gamma = 1.5$). If E_{sym} has a weak dependence on density then it is called a "soft" symmetry energy ($\gamma = 0.5$). See figure Figure 1.1.3. These values of γ represent reasonable lower and upper values for γ that are consistent with experimental

constraints on the symmetry energy for low density and saturation density nuclear matter.

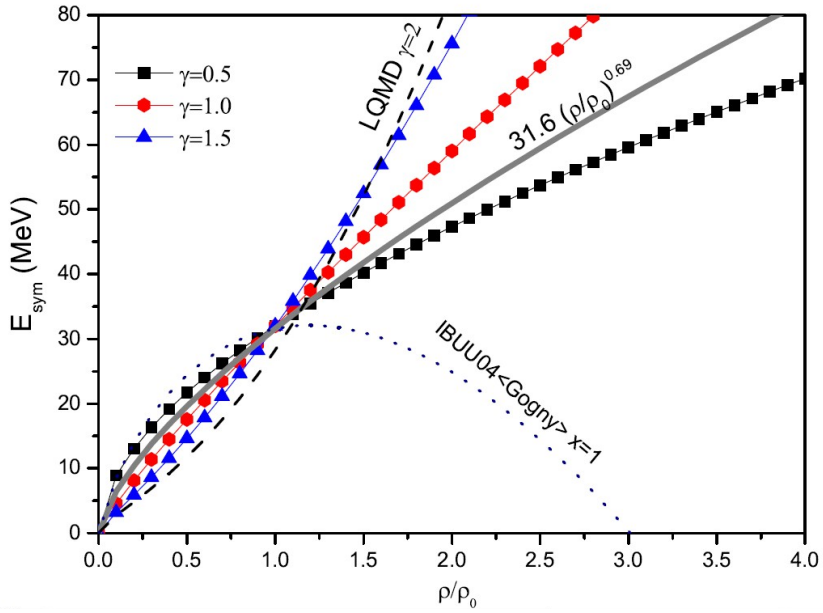

Figure 1.1.3: Adapted from [16] and [17] . Figure shows several predictions for the density dependence of the nuclear symmetry energy. The result using $\gamma = 0.69$ (solid grey line) is obtained from isospin diffusion data using the IBUU04 [18] transport code. The stiff (dashed grey line) and super soft (dotted grey line) parameteriszations using the IBUU04 and LQMD [19] transport codes are obtained from π^-/π^+ production ratios. Also shown are the predictions of UrQMD for three different parameterizations of the potential term.

Experimental constraints have so far mostly been placed on the asymmetric component of the symmetry energy at densities below saturation density by measurements in neutron-rich nuclei of Giant Monopole [20], Giant Dipole [10], and Pygmy Dipole resonances [21], measurements of isospin diffusion [22] and isotopic ratios of reaction fragments [23] [24] in heavy-ion reactions. The symmetry energy is therefore more tightly constrained at densities up to saturation and this is reflected in Figure 1.1.4 which shows that there is less variation in the model predictions at these densities.

Experimental constraints on the symmetry energy from heavy-ion collision experiments are shown in Figure 1.1.4. The constraints are represented by the shaded region which extends from saturation density down past half-saturation density. In contrast to the symmetry energy at saturation density there is very little experimental data, and no strong constraints on the strength of the symmetry energy, at higher densities. The lack of constaints at high nuclear density means that there is a strong divergence seen in the theoretical models for the density dependence of the symmetry energy (see Figure 1.1.4 and Figure 1.1.3).

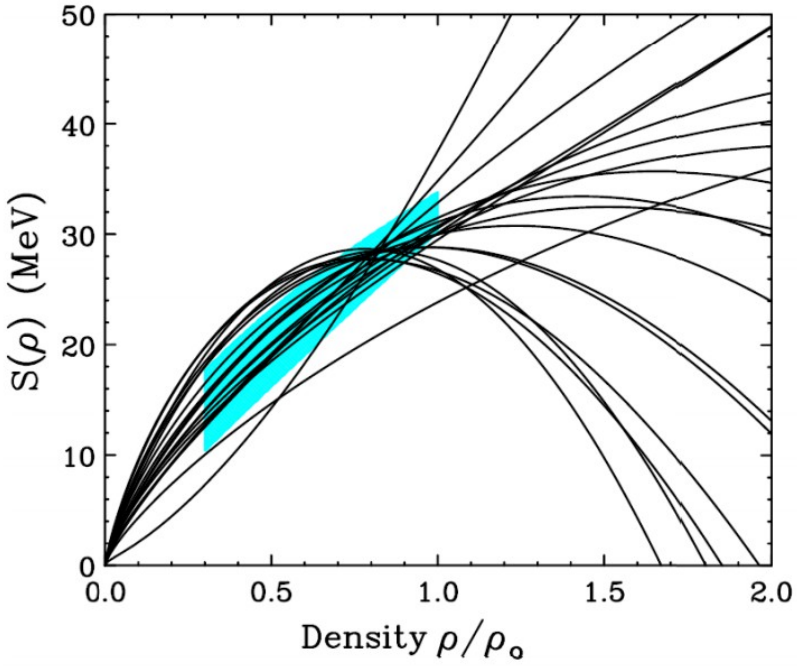

Figure 1.1.4: Adapted from [25]. Figure shows the predictions for the density dependence of the nuclear symmetry energy using Skyrme interactions [26]. Also shown in the blue shaded region are the experimental constraints on the symmetry energy from heavy ion collision experiments.

This absence of data at higher densities is due, in part, to difficulties involved in making such measurements. In order to study the symmetry energy at supra

saturation densities heavy-ion collisions must be employed to create a region of high-density nuclear matter and then any observables must be interpreted using a transport code. New observables needed to be proposed to investigate the behaviour of the symmetry energy at high densities. As a result there are very few experimental measurements at supra-saturation densities which have been obtained so far. The consequence of this is that there is still a wide variation in the model predictions for the high-density strength of the symmetry energy.

1.2 High-Density Probes of the Symmetry Energy

In the previous section some experimental observables were mentioned, such as dipole resonances and neutron-skin thickness in nuclei, which are sensitive to the strength of the symmetry energy at densities below the saturation density but these observables cannot be sensitive to the symmetry energy at high densities because such densities are not reached in terrestrial nuclei.

In order to place constraints on the symmetry energy at high densities it is necessary to make observations of dense nuclear matter. One way to do this is to observe astrophysical phenomenon such as neutron stars [12] [27]. The only way to study high-density nuclear matter in the laboratory is to use heavy-ion collisions to create the high-density region.

Observables sensitive to the nuclear symmetry energy were proposed and developed in recent years which involve the detection of the products of these heavy-ion reactions such as isotopic ratios, neutron/proton ratios [28] [29] [30] [31], neutron and proton elliptic flow and directed flow ratios [32] [33] [34] [35] [36], π

ratios and flows [37] [38], K ratios and flows [39], and Σ ratios and flows [40].

The top panel of Figure 1.2.1 shows that the densities reached in heavy-ion collisions at intermediate energies are high enough to probe the symmetry energy at supra-saturation densities. The density dependence of the symmetry energy for several of the parameterizations that were used for these calculations is shown in Figure 1.2.2. The model predictions shown in the lower panel of Figure 1.2.1 and Figure 1.2.3 indicate that neutron/proton and π^-/π^+ production ratios are sensitive to the strength of the symmetry energy at high densities.

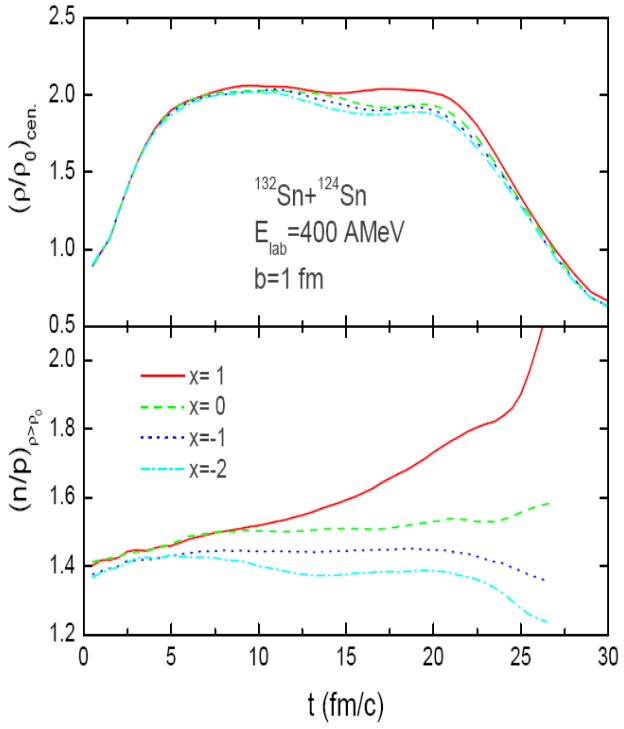

Figure 1.2.1: Adapted from [35]. The top panel is a plot of density against time, where t=0 is the start of the collision (1 fm/c = 3.3 x 10^{-24}s). The figure shows that the model predictions for the densities reached in ^{132}Sn +^{124}Sn heavy-ion collisions at 400 AMeV are around two times the saturation density. The bottom panel shows the predictions of the proton/neutron production ratios as a function of time for this reaction. The x parameters correspond to different predictions on the symmetry energy by different microscopic nuclear many-body theories using different effective interactions. Lower values of x represent predictions for a stiff symmetry energy and higher values are for a softer symmetry energy. [35].

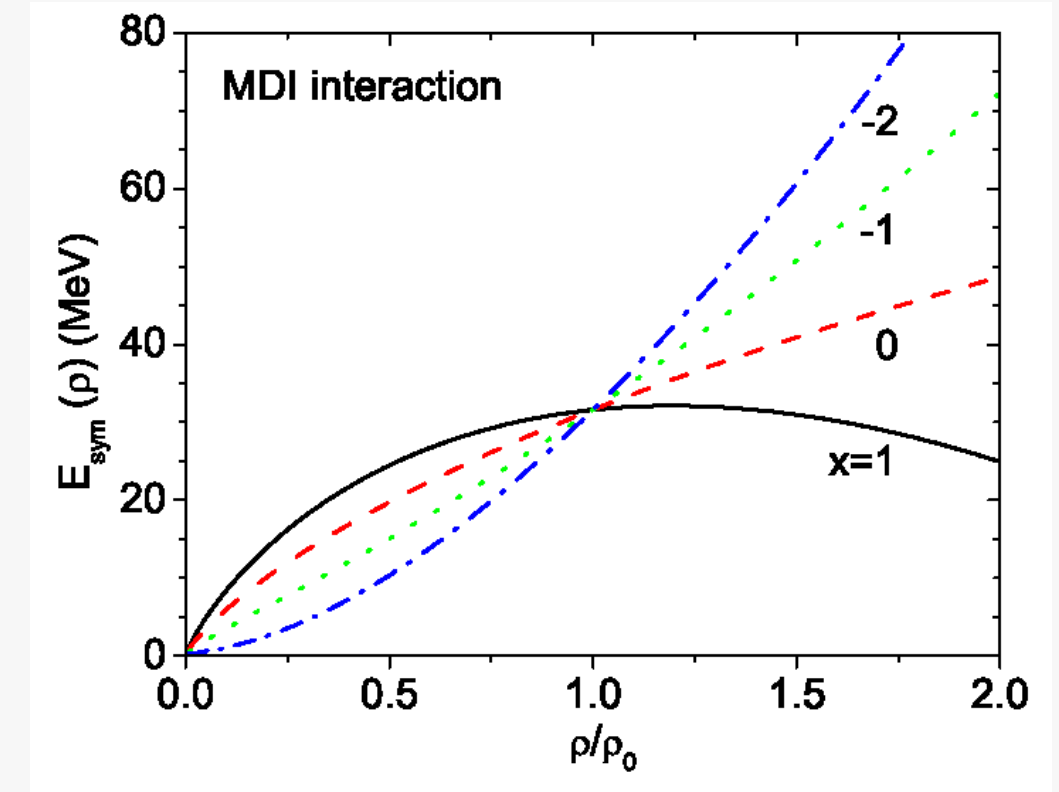

Figure 1.2.2: Adapted from [35] the figure shows the model predictions for the density dependence of the symmetry energy for several parameterizations of the momentum- and isospin-dependent single nucleon potential (MDI). Lower values of x represent a stiffer density dependence of the symmetry energy.

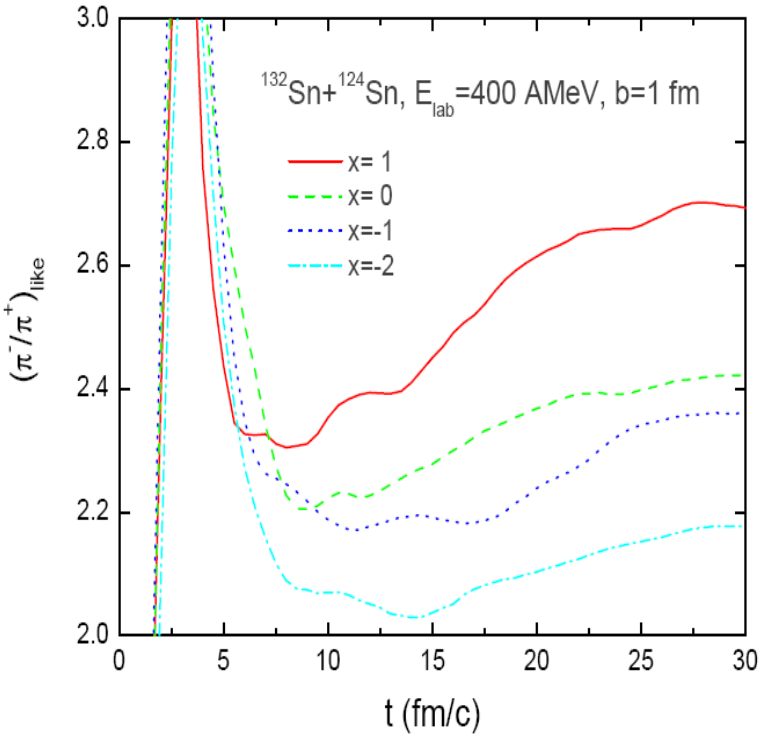

Figure 1.2.3: Adapted from [35] the figure shows the model predictions for the pion production ratio in ^{132}Sn +^{124}Sn heavy-ion collisions at 400 AMeV. π^-/π^+ can be defined as the ratio of the number of π^- particles to π^+ particles produced in the collision.

The observables which were used to measure the density dependence of the symmetry energy in the ASY-EOS experiment are the directed flow and elliptic flow of charged particles and neutrons, these variables will be discussed at length in the next chapter.

1.3 Author's Contributions

The analysis of the data from the ASY-EOS experiment was not a task designed to be undertaken by a single person and as such it is important to describe in which stages of the analysis I was involved. The ASY-EOS apparatus consisted of five detector systems - LAND, CHIMERA, ALADIN TOF Wall, MICROBALL and KRATTA (see chapter 3). Almost all of my work focused on analysing data

from the LAND detector. I was involved in all stages of the analysis - calibration, corrections, particle identification and clusterisation, extraction of flow parameters (see chapters 4 and 6).

The LAND detector has been operated at GSI for several decades and the procedures for the calibration and analysis of LAND are well established. However it was not possible to follow these procedures for much of the analysis process due to the malfunction of some new timing electronics components used during this experiment.

More senior members of the ASY-EOS international collaboration, P. Russotto and W. Trautmann, coordinated the data analysis effort at several laboratories (Catania, GSI, Krakow and Liverpool/Daresbury) and devised new procedures which allowed us to extract the measurements of flow from LAND despite the malfunctions.

As much of the analysis used these new procedures my primary task was to implement the new analysis procedures in parallel to the analysis conducted by P. Russotto. I contributed to the calibration and timing corrections and performed my own analysis in which I used clusterisation procedures to identify detected particles and extract the elliptic and directed flow for neutrons and charged particles. Finally I compared these measurements against model predictions and extracted a value for γ which was used to characterize the density dependence of the nuclear symmetry energy.

2 Relativistic Heavy-Ion Collisions

As stated earlier a way to study the symmetry energy at supra-saturation densities is using relativistic heavy-ion collisions between isospin asymmetric nuclei [16]. When two such nuclei collide a region of high density nuclear matter is created where nucleons from the projectile nucleus collide with those in the target nucleus - this will be referred to as the overlap region. In each collision we can separate the nucleons of the two nuclei into two categories, spectator nucleons which are not directly involved in the collision and participant nucleons which are located in the overlap region of the two nuclei and form part of the high-density region during the collision.

2.1 Impact Parameter

The impact parameter, b, is a quantity that is defined, for each collision, as the length of the vector which goes between the centre of the target nucleus and the trajectory of the projectile nucleus, and which is perpendicular to the beam axis [41], see Figure 2.1.1. The nucleus is an extended object composed of many interacting particles and the size of the impact parameter will determine how many of the constituent particles are directly involved in the collision, and on the number of spectator nucleons which can influence the way the collision evolves over time.

Therefore the size of the impact parameter will have a significant effect on the evolution of any heavy-ion collision. For example, more central collisions with smaller values of b will involve greater transfer of energy and momentum [42] than is the case in peripheral collisions which have large b values.

This means that there will be large fluctuations in the observables from each event depending on the value of the impact parameter and so any comparison of the observations from heavy-ion collisions to theoretical models will require that events are selected which fall within a narrow range of b values.

The impact parameter cannot be measured directly and has to be estimated from measurements of global observables. A global observable is determined by using all or most of the detected particles. The global variables used to estimate the impact parameter in the ASY-EOS experiment are the light charged particle transverse kinetic energy ($E_{\perp 12}$), ratio of transverse to longitudinal kinetic energy of detected particles (E_{Rat}), total charge of $Z \geq 2$ products (Z_{bound}) and the Z value of the largest charged fragment (Z_{Max}).

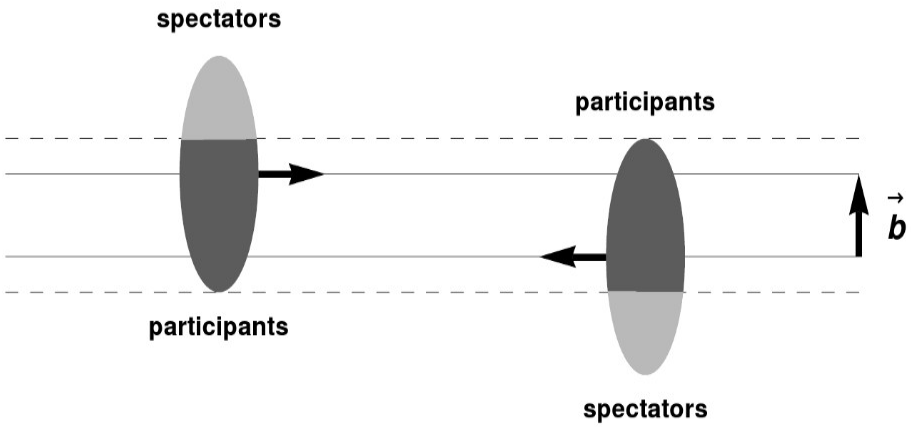

Figure 2.1.1: Schematic diagram showing the impact parameter b in a mid-peripheral heavy-ion collision.

2.2 Reaction Plane

The reaction plane is defined for each binary collision as the direction of the vector which is perpendicular to the beam axis and points from the target nucleus to the trajectory of the projectile nucleus. Like the impact parameter the reaction plane cannot be directly measured and must be estimated from global variables for each event. The reaction plane can be determined by constructing a vector, $\vec{Q}$, which is defined in equation 2.1 and illustrated in Figure 2.2.1.

$$\vec{Q} = \sum_{n=1}^{N} \vec{u_n} w_n \tag{2.1}$$

Where N is the number of detected particles being used to estimate the Q-vector, $\vec{u_n}$ is the unit vector which is parallel to the transverse momentum of the detected particle and w_n is the weighting factor. The value of the weighting factor is set as $w_n = 1$ for particles are identified as being spectator nucleons from the projectile nucleus and $w_n = -1$ for particles which are identified as being spectator nucleons from the target nucleus. Particles which are identified as coming from the overlap region of the collision are given a weighting factor of zero.

Taking the sum of the transverse momentum vectors for all detected reaction products, the resultant vector defines the reaction plane and the azimuthal distribution of the reaction products is measured relative to this vector. Azimuthal distributions show how particles are emitted from the heavy ion collision in the plane which is perpendicular to the beam axis. Such distributions are always measured relative to the reaction plane.

In order to determine the reaction plane it is necessary to identify whether a detected particle originated in the spectator nucleons of the projectile or the target nucleus, or if it came from the high density overlap region of the collision. In order to make this determination the particles rapidity, y_{lab}, is measured:

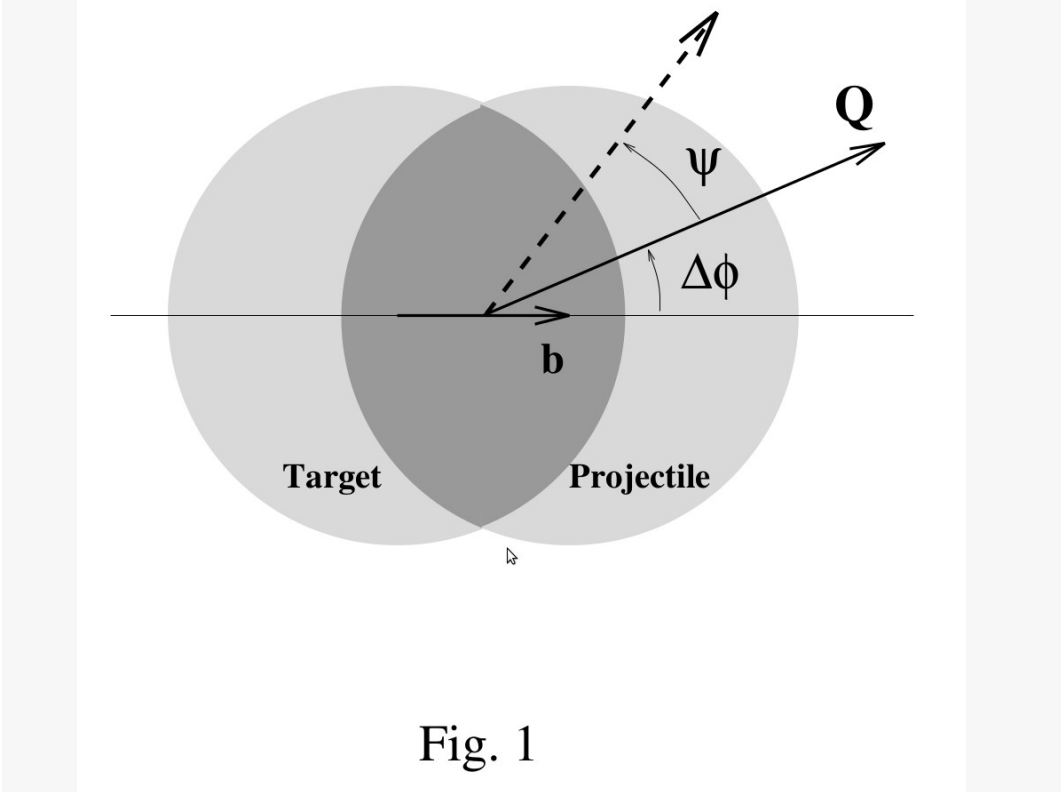

Figure 2.2.1: Adapted from [43]. Diagram of a semi-central heavy ion collision viewed along the beam axis. The Q vector defined in equation 2.1 is shown along with the impact parameter, b. You can see that the measured value of Q differs from the true value by $\Delta\phi$. The dashed line represents an emitted particle with a measured azimuthal angle of Ψ and a true azimuthal emission angle of $\phi = \Psi + \Delta\phi$.

$$y_{lab} = \frac{1}{2} ln \frac{E + p_L c}{E - p_L c} \tag{2.2}$$

Where E is the kinetic energy of the particle and p_L is the component of the particle's momentum which is parallel to the beam axis.

Particles detected in forward rapidity, such as particles coming from the projectile nucleus, are typically given a weighting factor of 1 whilst those with backwards rapidity, originating from the target nucleus, are weighted by -1. Details of the rapidity ranges used in the ASY-EOS experiment can be found in Table 6.1.1.

However for any event the measured reaction plane can differ from the true reaction plane, called the particle plane [44], see Figure 2.2.2, because the distribution of the participant nucleons in the overlap region may have a different principal axis from that of the overlap region. The consequence of this is that when azimuthal anisotropies are measured over a large number of events they will always appear smaller than the true ones because the distributions become smeared by the error, $\Delta\phi$, in the reaction plane [43].

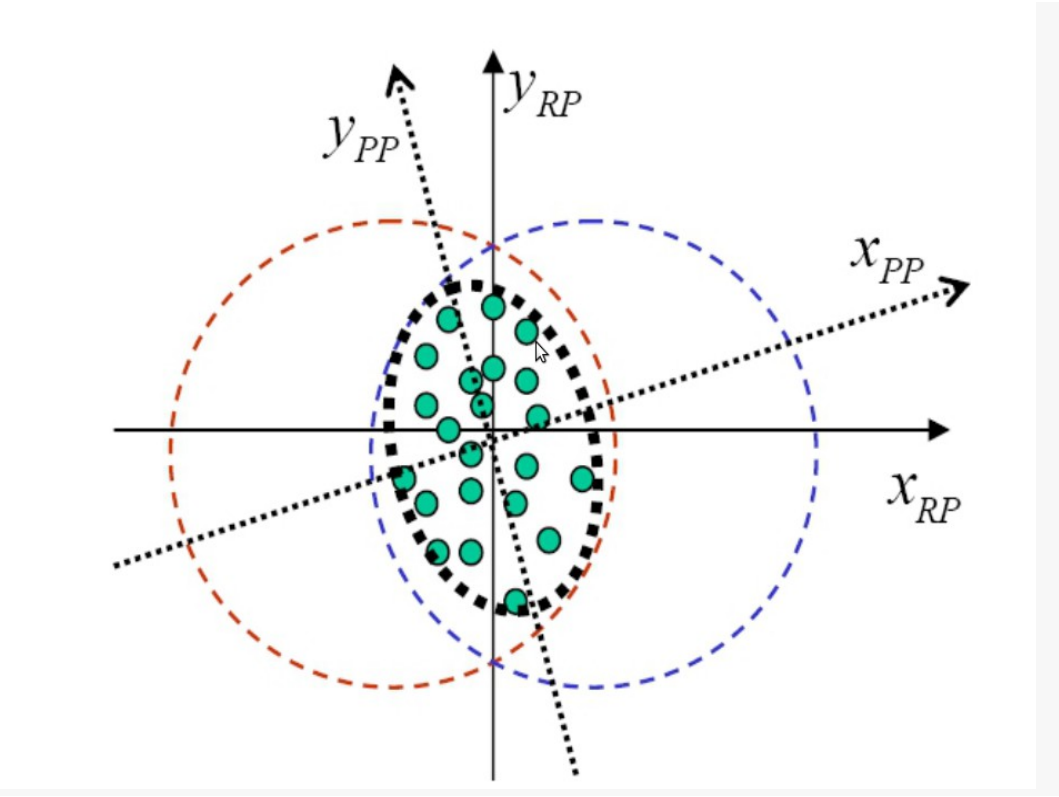

Figure 2.2.2: Schematic diagram illustrating the difference between the reaction plane and particle plane for a mid-peripheral heavy-ion collision [44].

2.3 Directed and Elliptic Flow

Flow in heavy-ion collisions is a collective motion caused by interactions between the constituents of the colliding particles which causes particles to be emitted preferentially in certain directions. Elliptic flow can be described as an anisotropic

emission pattern in which particles are emitted more strongly along a particular azimuthal axis. For example, in the case of heavy ion collisions at intermediate energies the nucleons are emitted most strongly along the axis that is perpendiclar to the reaction plane.

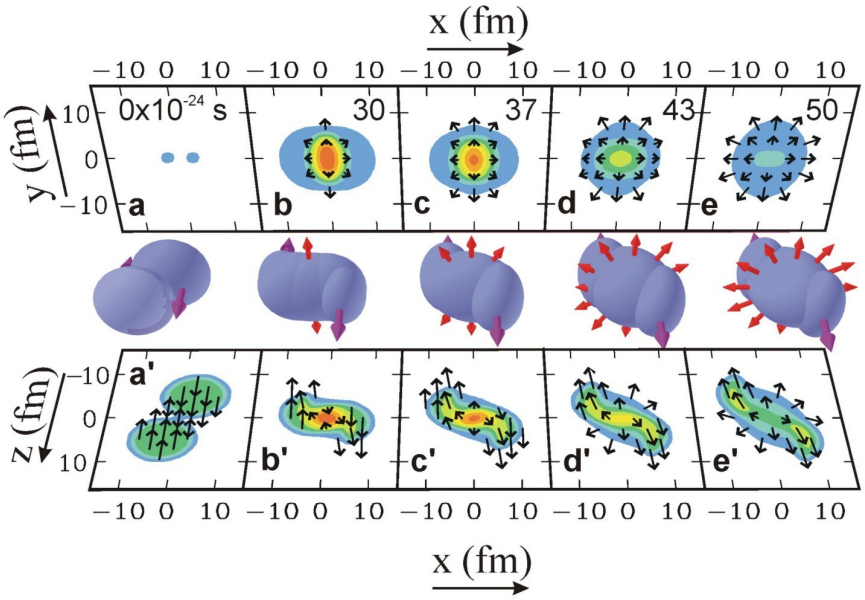

Figure 2.3.1: Adapted from the NuSYM11 lecture presented by W.Lynch. The figure shows how the high density overlap region evolves during a heavy ion collision.

In mid-peripheral heavy-ion collisions, which are collisions with an impact parameter between 5.5 - 7.5fm [16], the expansion of the high density region of nuclear matter is constrained by the spectator nucleons as shown in the diagram of Figure 2.3.1. This leads to a phenomenon called elliptic flow in which the azimuthal emission of mid-rapidity reaction products occurs anisotropically with a greater number of reaction products being emitted perpendicularly to the reaction plane. This elliptic flow can be parameterized by fitting the azimuthal

distribution of the emitted mid-rapidity particles with a Fourier expansion.

$$\frac{dN}{d\phi} = \frac{1}{2\pi}(1 + 2\sum_{n=1}^{2} v_n cos[n\phi]) \tag{2.3}$$

The first coefficient, v_1, is called the directed flow and the second coefficient, v_2, is the elliptic flow. The values of v_1 and v_2 represent the magnitudes of the directed and elliptic flow. ϕ is the azimuthal angle which is measured relative to the reaction plane of each individual collision.

The ratio of the v_2 of neutrons and protons, or neutrons and light charged particles, is predicted to be sensitive to the strength of the nuclear symmetry energy at high density. Figure 2.3.2 shows that the v_2^n/v_2^H ratio predicted in the UrQMD calculations changes significantly between the stiff and soft parameterizations of the symmetry energy. Higher values of v_2^n/v_2^H indicate that the symmetry energy has a stiffer dependence on the density of nuclear matter.

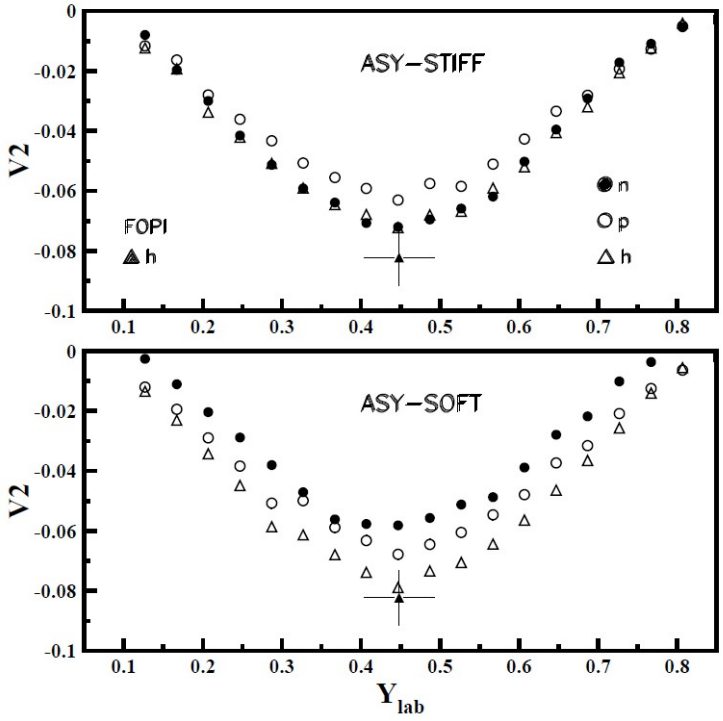

Figure 2.3.2: Adapted from [16]. Figure shows the modified UrQMD [45] [46] [47] predictions for the v_2 of protons, hydrogen isotopes and neutrons for the stiff ($\gamma = 1.5$) and soft ($\gamma = 0.5$) parameterizations of the symmetry energy. The relative strengths of v_2^n and v_2^p are reversed in each case.

In summary Figure 2.3.2 shows that simulations using the UrQMD transport model predict that the elliptic flow for neutrons is significantly larger in the case of a stiff symmetry energy than for the soft case. Therefore by comparing the ratio of the neutron and proton v_2 to the UrQMD predictions it is possible to place constraints on the value of the symmetry energy at high nuclear densities.

2.4 Ultrarelativistic-Quantum-Molecular-Dynamics (UrQMD)

Ultrarelativistic-Quantum-Molecular-Dynamics is a transport model originally designed to study particle production at high energies [48] and which was modified

for heavy-ion collisions at intermediate energies [45] [46] [47]. The modifications involved using a nuclear mean field which corresponds to a soft equation of state with momentum dependent forces [16] [49]. The modified UrQMD was used to interpret the results from the FOPI (see Section 2.5) and ASY-EOS experiments.

The density dependence of the nuclear symmetry energy can be described in terms of a potential and kinetic component [50] using the power law which is first outlined in equation 1.5:

$$E_{sym}(\rho) = E_{sym}^{pot} + E_{sym}^{kin} = 22\text{MeV}(\frac{\rho}{\rho_0})^{\gamma} + 12\text{MeV}(\frac{\rho}{\rho_0})^{\frac{2}{3}} \tag{1.5}$$

The parameter γ determines how strongly the symmetry energy depends on density, a larger γ value means a stronger density dependence which is called a "Stiff" symmetry energy. Lower γ means a weaker density dependence and corresponds to a "Soft" symmetry energy. The UrQMD predictions are made for two choices of $\gamma = 0.5$, which represents a soft dependence, and $\gamma = 1.5$ which is a stiff density dependence, see figure Figure 1.1.3.

Constraints can be placed on the strength of the symmetry energy by comparing the results from experiment against UrQMD predictions for both the soft and stiff parameterisation of the symmetry energy which have been filtered for the acceptance and conditions of the experiment. It is then possible to use a linear interpolation to extract a value of γ from the data.

2.5 The FOPI Experiment

The FOPI experiments conducted at GSI used the LAND (see Section 3.5) and FOPI Phase 1 detectors [51] to measure collective flow observables for neutrons and isotopes of hydrogen [52]. These experiments were not originally designed to probe the symmetry energy using elliptic flow ratios but the data were re-analysed [53] and compared against the predictions of the UrQMD model in order to determine constraints on the symmetry energy. The UrQMD model used in this re-analysis was modified for use with heavy-ion collisions at intermediate energies [45] [46] [47].

In the FOPI experiment LAND was used to detect neutrons and light charged fragments from the heavy-ion collisions. The FOPI forward wall [51] was used to estimate the impact parameter and reaction plane of each event thus allowing azimuthal distributions relative to the reaction plane to be produced for neutrons and light charged particles which were identified by LAND. These azimuthal distributions exhibited the anisotropies which were described in the previous sections as directed flow and elliptic flow.

The v_1 and v_2 flow values extracted from the FOPI reanalysis are shown in Figure 2.5.1. Figure 2.5.2 shows the v_2 ratio for neutrons and hydrogen isotopes which are compared against the UrQMD predictions. The modified UrQMD code was used to produce predictions of the v_2 ratio for a soft ($\gamma = 0.5$) and hard symmetry energy ($\gamma = 1.5$). The experimental data were then compared against the UrQMD predictions using a linear interpolation between the predicted values of v_2 for $\gamma = 0.5$ and $\gamma = 1.5$ to extract a value for γ from the data.

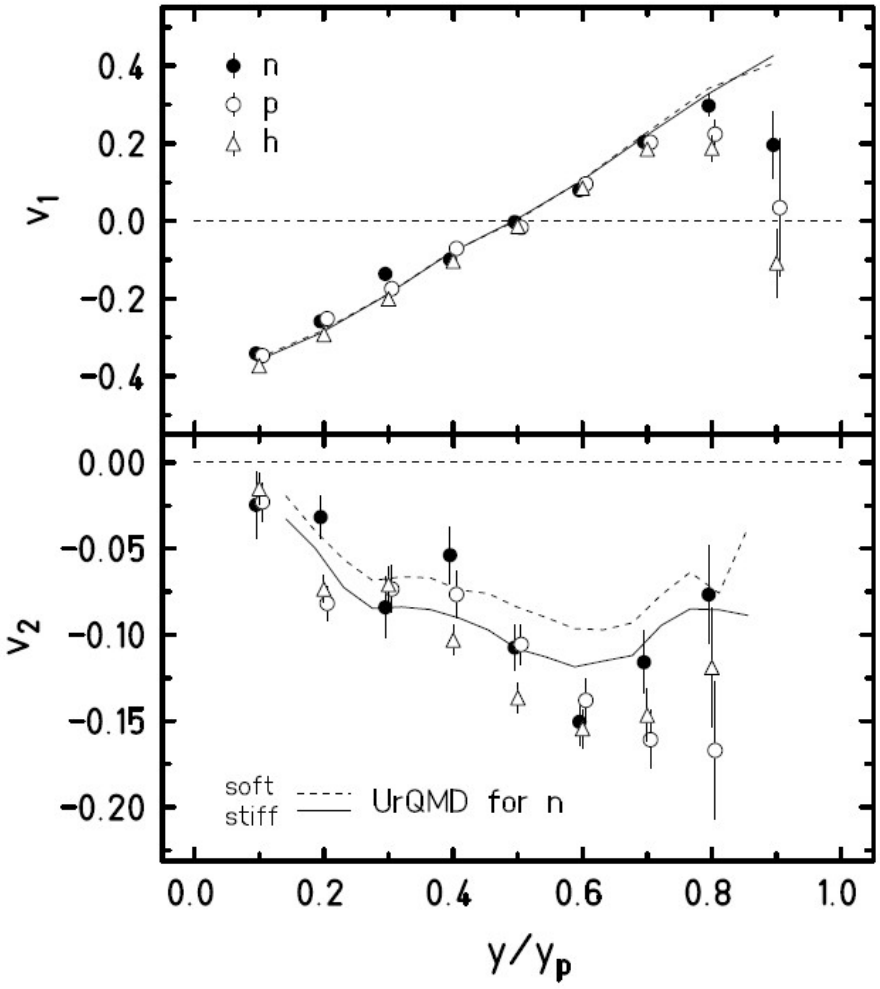

Figure 2.5.1: Top panel shows the v_1 values against normalized rapidity for protons, charged particles and neutrons measured in the FOPI experiment. The UrQMD predictions for stiff ($\gamma = 0.5$) and soft ($\gamma = 1.5$) symmetry energy are shown as solid and dashed lines respectively. The lower panel shows the same plot for v_2 measurements. The figure is taken from [53]. Normalized rapidity is defined as y_{lab}/y_p, where y_p is the rapidity of the projectile nuclei.

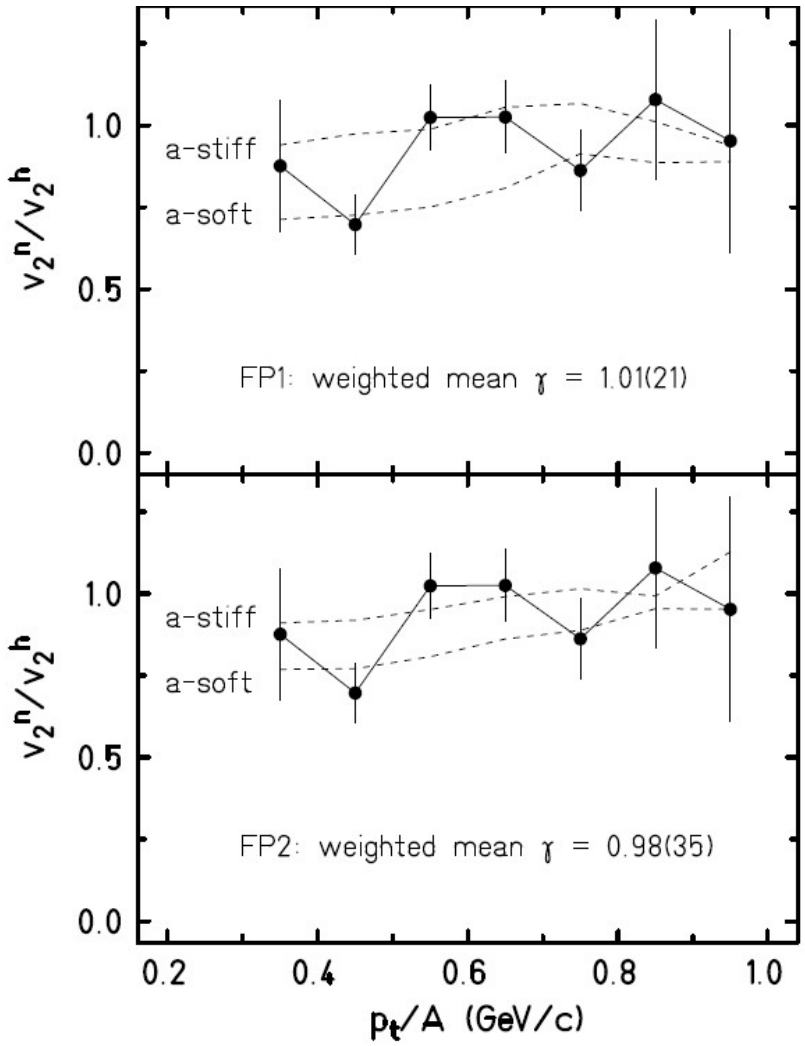

Figure 2.5.2: The plot shows the ratio of v_2 for neutrons and hydrogen isotopes, integrated over a rapidity range of $0.25 \leq y/y_p \leq 0.75$, as a function of transverse momentum per nucleon. These results are compared against the UrQMD model predictions which are obtained using the FP1 and FP2 parameterisations in the top and bottom panels respectively. The figure is adapted from [53]. FP1 and FP2 are different parameterisations of the UrQMD transport model which are used to simulate the heavy ion collisions. FP1 and FP2 are expected to under-predict and over-predict the magnitude of the elliptic flow respectively and so the most probable value for γ should be between the values returned by these two parameterizations. Details of FP1 and FP2 can be found in reference [54]

.

The values of γ derived from the linear interpolations are 1.01 ± 0.21 for the FP1 parameterisation and 0.98 ± 0.35 for FP2. In addition to these measurements the v_2 ratio for neutrons and protons was also extracted and yielded $\gamma = 0.99 \pm 0.28$ and $\gamma = 0.85 \pm 0.47$ for FP1 and FP2 respectively. This is significant because the results give similar values for γ even when interpreted using different paramaterisations of the UrQMD code.

These measurements were combined to give a final value of γ from the FOPI data of $\gamma = 0.9 \pm 0.4$. This result was consistent with fragmentation studies of nuclear matter below saturation density [21] [55] [11] which favour a moderately soft symmetry energy but it is acknowledged that the limited statistics in the FOPI experiment limit the constraints which can be placed on the symmetry energy. Following these results further experimental work was suggested to reduce the uncertainties and place tighter constraints on the symmetry energy at supra saturation densities [53].

3 The ASY-EOS Experiment

This Chapter describes the equipment used to produce the beam, and the detector systems used to select and take measurements of the collisions between the beam and the target nuclei, in a new experiment performed at the GSI Helmholtz Centre for Heavy Ion Research near Darmstadt, Germany, in 2011. The ASY-EOS experiment was conceived to probe the density dependence of the nuclear symmetry energy at high densities by measuring the elliptic flow of both hydrogen and neutrons in ^{197}Au + ^{197}Au heavy-ion collisions at 400 AMeV.

As mentioned in the previous chapter, an earlier experiment using the LAND and FOPI detectors took measurements of neutron and hydrogen elliptic flows [56] for Au + Au systems but was not originally designed to place constraints on the symmetry energy due to the limitations of theoretical models at the time [1]. Subsequent developments in theoretical modelling allowed the data from the FOPI experiment to be re-analysed with a focus on measuring the symmetry energy but poor statistics meant that no strong conclusions could be drawn from the data.

The ASY-EOS experiment was proposed to make similar measurements of the neutron/hydrogen elliptic flow ratio for the same ^{197}Au + ^{197}Au system but with the aim of improving upon the statistics of the FOPI experiment by a factor between 20-30 in order to place more stringent constraints upon the symmetry energy at high densities.

3.1 The GSI Heavy-Ion Accelerator Facility

The ASY-EOS experiment was performed at the GSI heavy-ion accelerator facility. The schematic diagram in Figure 3.1.1 shows the major components of the GSI facility. The heavy-ion beam originates from ion sources at the start of the UNIversal Linear ACcelerator (UNILAC). The UNILAC accelerates the ions to 18 AMeV and injects the beam into the Heavy Ion Synchrotron (SIS) which has a maximum bending power of 18 Tm. The UNILAC and SIS18 accelerators are capable of accelerating any stable ion from hydrogen up to uranium and can reach energies of between 1-4.5 AGeV, depending on which ion species is being accelerated. After the SIS18 the beam can be injected into the FRagment Separator (FRS) which can be used to produce secondary radioactive ion beams. However, the ASY-EOS experiment used a stable beam of ^{197}Au which was delivered directly from the SIS18 to the ASY-EOS setup in Cave C of experimental hall II.

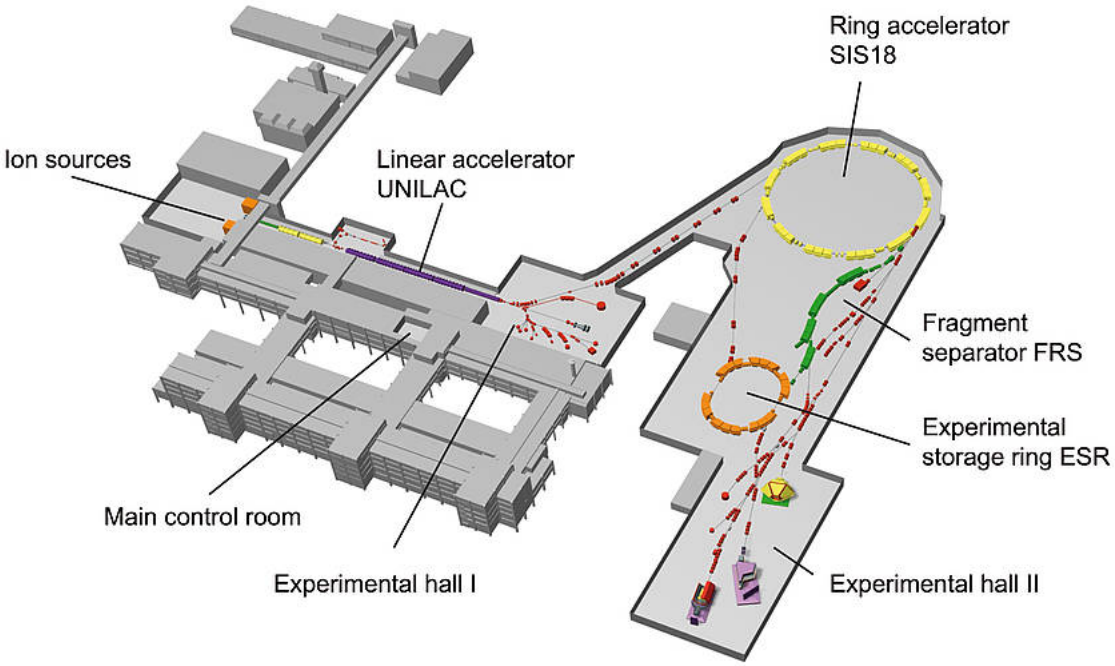

Figure 3.1.1: Schematic overview of the GSI heavy-ion accelerator facility in Darmstadt (Germany).

3.2 Overview of the Experimental Apparatus

The 400 AMeV ^{197}Au heavy-ion beam entered Cave C in a vacuum tube and the Start detector, which was located just upstream from the ALADIN Dipole magnet [57], was used to register the arrival time of each ion. After the beam passed through the Start detector it entered the ALADIN magnet which is a permanent fixture in Cave C but was turned off for the ASY-EOS experiment. The dimensions of the cave made it necessary to locate the target and most of the detector systems downstream of ALADIN, which meant that it was not possible to place the target inside the vacuum tube. This required that the MICROBALL detector [58] be positioned around the target and used as a back-angle hodoscope to allow collisions between the beam and the target to be distinguishable from

collisions with particles in the air.

When a collision between a beam ion with a target nucleus takes place, the reaction fragments emitted at small forward polar angles were detected by 4 rings of the CHIMERA detector [59] and the ALADIN TOF Wall [57], which were both used in the determination of the reaction plane and impact parameter in addition to forming part of the good event trigger. Fragments emitted at larger polar angles, from the mid-rapidity region, were detected by LAND [60] and the Krakow array, which is also called KRAkow Triple Telescope Array (KRATTA) [61]. LAND was used to measure emission angles and energies of neutrons and charged particles from the mid-rapidity region.

Figure 3.2.1 and Figure 3.2.2 show pictures and schematic diagrams of the experimental setup.

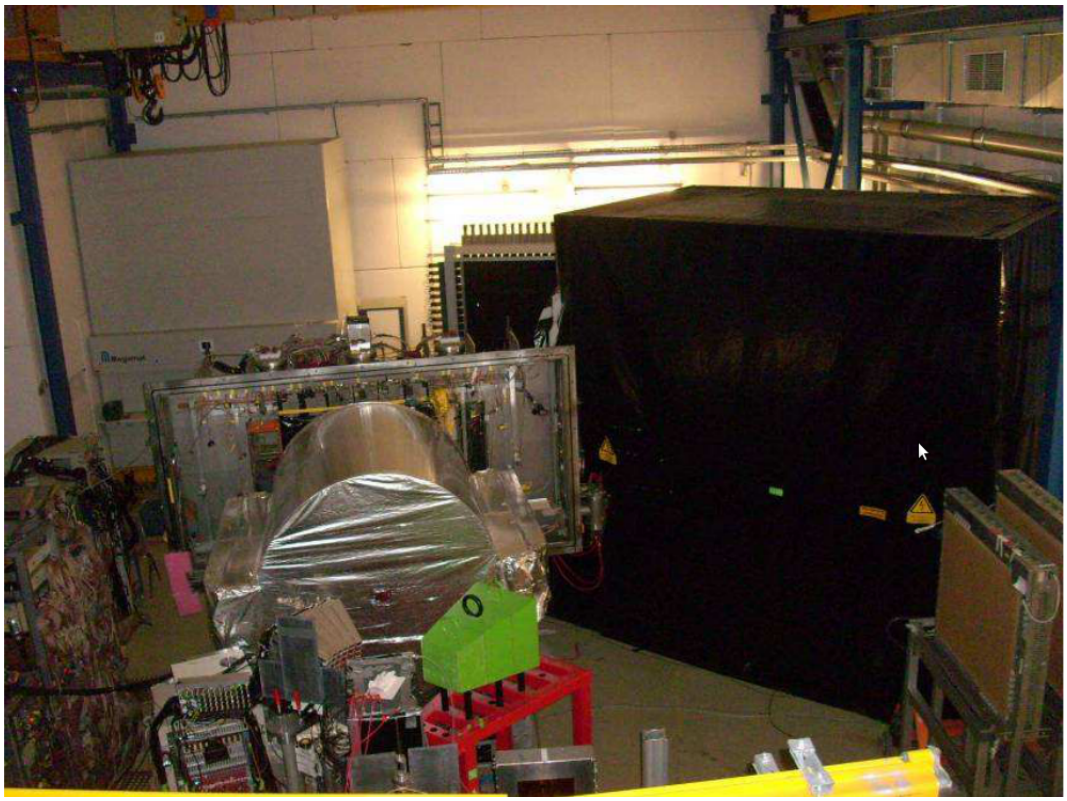

Figure 3.2.1: Photograph of the ASY-EOS experimental setup in Cave C at GSI.

The CHIMERA and ALADIN TOF Wall detector systems were positioned directly downstream from the target, after the ALADIN magnet. CHIMERA was composed of 4 rings which gave 2π coverage of azimuthal angles over a narrow range of forward polar angles and formed the main part of the system used to determine the reaction plane of each collision. The ALADIN TOF Wall was used to measure the atomic number and velocity of collision fragments emitted at small polar angles. This information was useful for the determination of the the reaction plane and impact parameter of each collision. The LAND and KRATTA detectors where positioned downstream of the target on opposite sides of the beam axis. Both detectors were located at polar angles which allowed them to measure mid-rapidity particles with high transverse momenta.

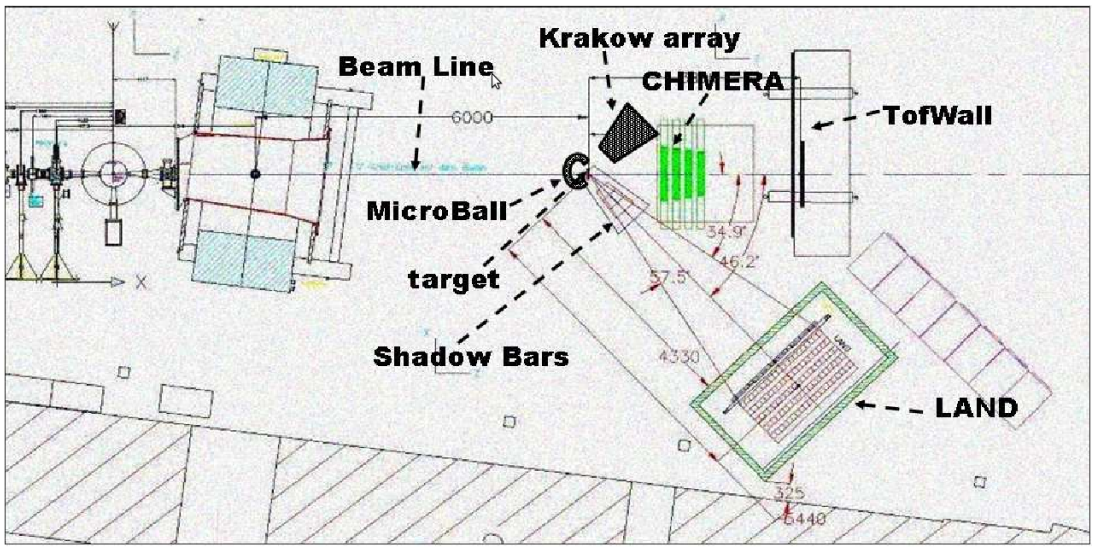

Figure 3.2.2: Schematic diagram of the ASY-EOS experimental setup in Cave C at GSI.

3.3 Event Selection

The beam intensity during the experiment was approximately 100,000 particles per second, which had around a 1-2 percent probability of interacting with the target. The result is around 1000 Au-Au collisions per second. Of these collisions we are only interested in those which have impact parameters small enough to include a significant number of nucleons in the reaction but large enough that the expansion of the high density region is still effectively constrained by the spectator nucleons.

Event selection refers to the process by which such suitable collisions are selected from the larger body of data. In the sections below I will describe the various detector systems used in the event selection process and explain their function.

The event selection was performed by the start detector, Microball, CHIMERA and the ALADIN TOF wall. A brief description of the composition and function of each of these detectors is given in the following sections.

3.3.1 Start Detector

The purpose of the Start detector is to register the time of arrival of a beam particle. This information is vital as it is needed to determine the time-of-flight of the collision fragments which are observed by all the other detectors. The Start detector is the only detector in this experiment which was located inside the vacuum pipe and consists of a single plastic scintillator foil which is read by two photomultiplier tubes.

A maximum beam intensity of 100,000 particles per second was used to ensure

that the Start detector was able to measure the arrival time of each particle. The signal from the Start detector was sent on a delay circuit and used as a common stop by the LAND TacQuila timing electronics.

3.3.2 MICROBALL

For this experiment it was necessary to locate the target downstream of ALADIN, which meant that it was not possible to place the target in vacuum. This also meant that we needed a way to distinguish collisions between the beam and the target nuclei from those with particles in the air and the beam window.

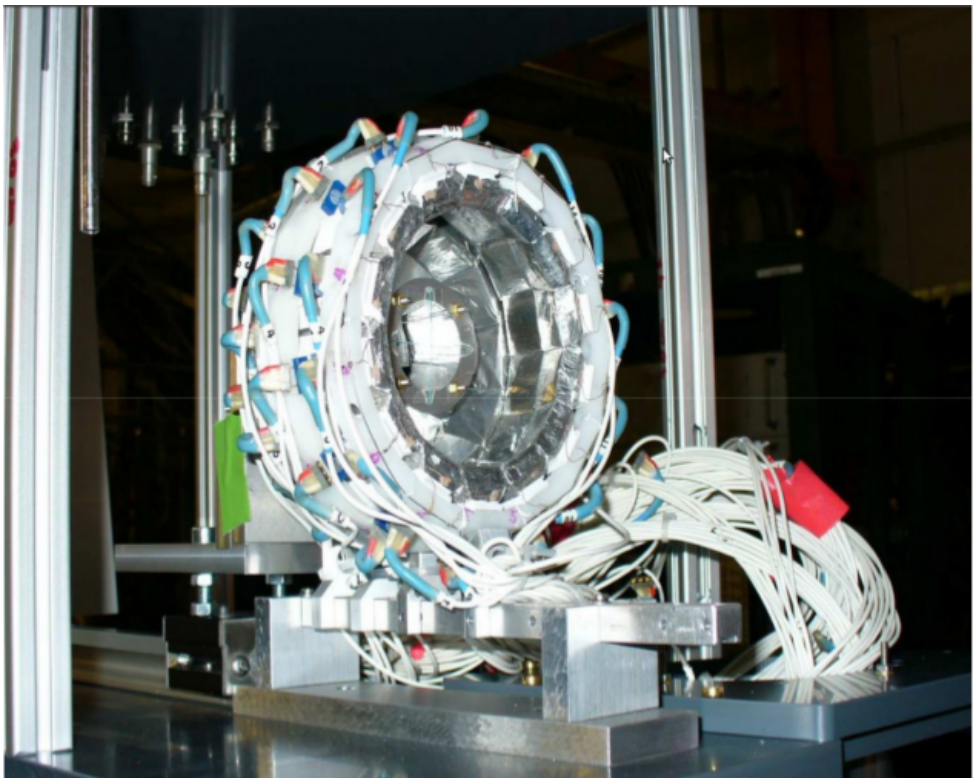

Figure 3.3.1: Part of the MICROBALL detector array used in the ASY-EOS experiment.

Air particles are far lighter than the beam particles and so these collisions produce fragments which mostly scatter forwards, whereas the mass symmetric

collisions with the target nuclei would produce a greater number of back scattered particles. Part of the MICROBALL array [58] was placed around the target and was used to measure the distribution of collision fragments with backward scattering angles on an event-by-event basis and so provided a trigger for the collisions of interest.

The part of the MICROBALL detector which was used (see Figure 3.3.1) consisted of 50 CsI(Tl) detector elements which where each 1 cm thick and arranged into 4 rings which covered polar angles between 60 and 147 degrees. For collisions between the beam and the target nuclei the azimuthal distribution of back scattered fragments could be anti-correlated with the distribution seen in CHIMERA and used to help estimate the reaction plane of the collision.

3.3.3 ALADIN Time-of-Flight Wall

The ALADIN Time-of-Flight Wall [57] was located directly downstream from CHIMERA and used to detect charged particles emitted at polar angles less than 7°. The TOF Wall is composed of 192 vertically orientated plastic scintillator paddles arranged into 2 planes. Each plane is 2.4 m wide and 1 m high. The paddles themselves are 2.5 cm wide by 1 cm thick and are read out at each end by a photomultiplier tube. The TOF Wall can measure time of flight with a resolution of about 250 ps for lithium fragments with the resolution improving smoothly to 100 ps for $Z \geq 10$. The TOF Wall was used with CHIMERA and MICROBALL to estimate the reaction plane and impact parameter for each event.

3.4 CHIMERA

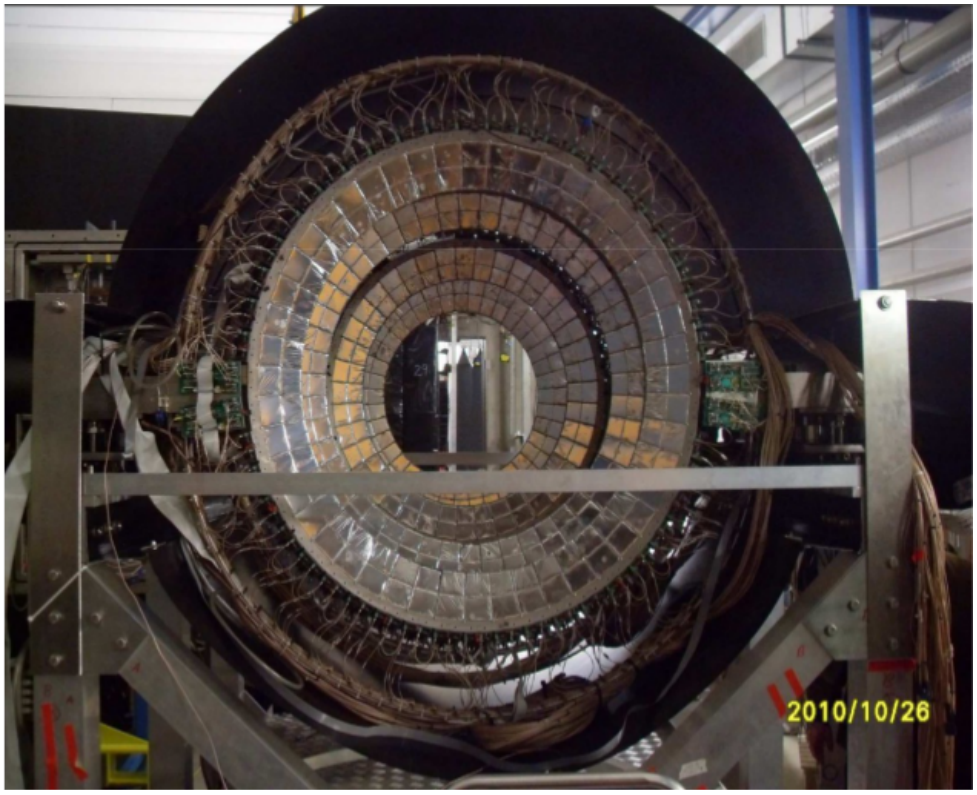

Figure 3.4.1: The 8 rings of the CHIMERA multi-detector array used in the ASY-EOS experiment.

The CHIMERA multi-detector array (Charged Heavy Ion Mass and Energy Resolving Array) [59] is a 4π detector which is operated at the LNS in Catania (Italy) and is composed of 1192 trapezoidal cells arranged into rings. 8 of these rings, containing 352 cells of 12 cm thick CsI(Tl), were transported to GSI for the ASY-EOS experiment and installed to give full 2π coverage around the beam axis over a range of polar angles from 7-20° (see Figure 3.4.1). Each ring also had 4 300 μm Silicon detectors placed in front of the cells which were directly above, below and to the sides of the beam axis.

Data from CHIMERA were used in conjunction with the TOF Wall and MICROBALL to estimate the reaction plane and impact parameter for each event,

see section 2.2 for details. Events were only considered if there were at least 4 hits in CHIMERA plus 2 hits in MICROBALL to ensure that it was a beam-target interaction.

3.5 LAND

The Large Area Neutron Detector (LAND) is capable of detecting neutrons with energies from 100 MeV up to 1000 MeV with efficiency in excess of 90% for the higher energy neutrons [60]. LAND was placed 5 m from the target and occupied polar angles in the range 35°-57°, which covers the mid-rapidity kinematic region of the collision products. This allowed LAND to measure the emission angles and energies of the neutrons and hydrogen isotopes produced in the heavy-ion collisions, from which the elliptic and directed flow were determined. LAND is not a 2π detector but is able to build up to full 2π azimuthal distributions over a large number of events because the azimuthal angles are measured relative to the reaction plane of the heavy-ion collision which has a random orientation for each event.

3.5.1 Structure of LAND

The LAND detector is constructed from 200 paddles which are arranged into 10 planes with paddles in adjacent planes being arranged perpendicularly to each other in order to provide position resolution in both horizontal and vertical directions (see Figure 3.5.1). Each paddle is 2 m long, 10 cm wide and 5 cm thick and is composed of 10 layers of 5 mm thick plastic scintillator placed in between 11 layers of iron. The iron layers are each 5 mm thick except for the outer layers which are only 2.5 mm thick in order to maintain a consistent structure from the front to the back of the detector [60].

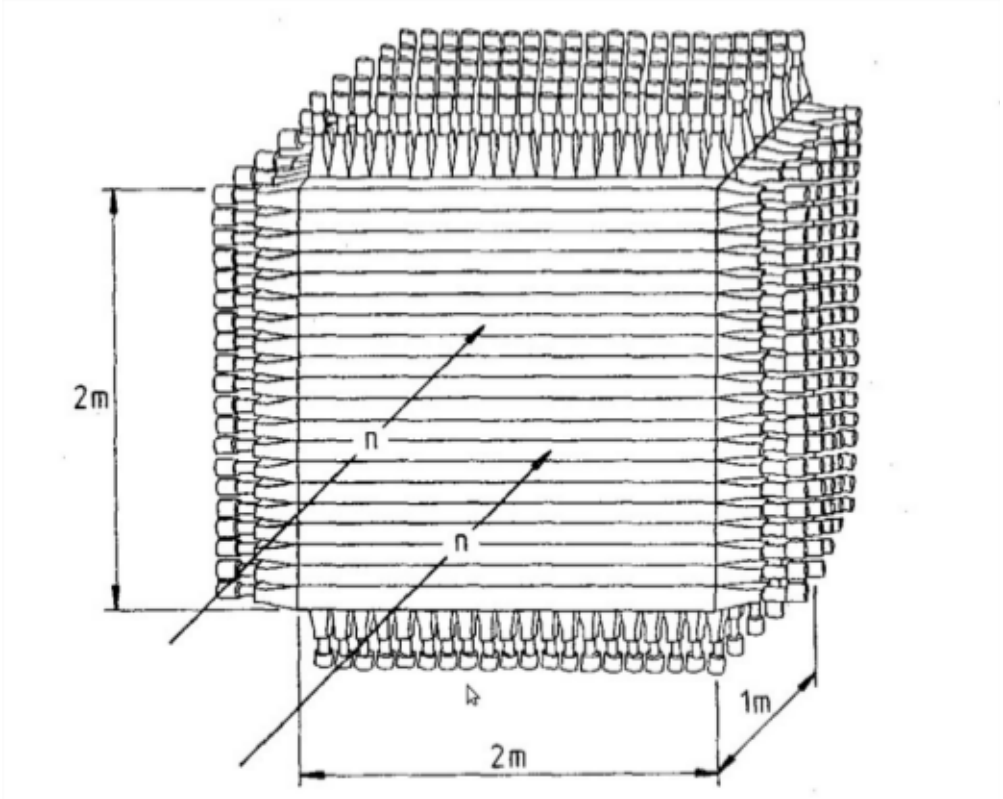

Figure 3.5.1: Schematic diagram of the structure of LAND without the VETO [60].

Interactions between high-energy neutrons and the iron layers produce secondary charged particle showers which are detected by the plastic scintillator. The layers of plastic scintillator feed into a single photomultiplier tube at each of the paddle and the signal from the photomultiplier is split into two signals (see Figure 3.5.2). One goes to a TDC via a constant fraction discriminator which operates on a common stop used to determine the time of flight for the detected particle (see below for details on the TacQuila[17] timing electronics). The second is read by a QDC which provides information on the energy. The position of the detected particle can be determined by comparing the TDC or the QDC signals of the photomultipliers at each end of the paddle.

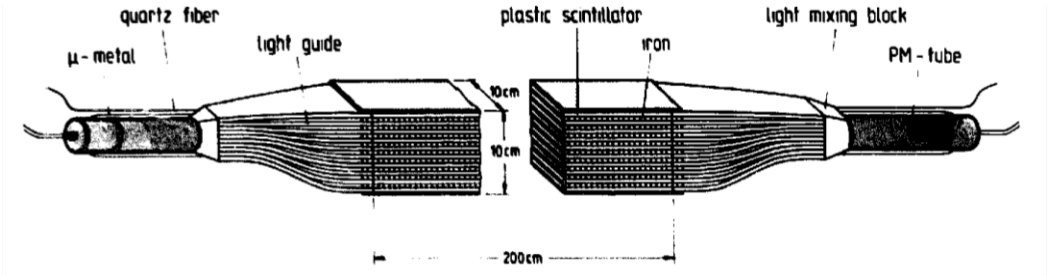

Figure 3.5.2: Schematic diagram of the structure of a paddle of the LAND detector [60].

3.5.2 The VETO Wall

For the ASY-EOS experiment it was vital that LAND be able to distinguish between neutrons and charged particles. This required the use of the VETO wall. The VETO is a plane of plastic scintillator paddles which is positioned in front of LAND and covers the same area. The VETO is made up of 20 paddles which are parallel to the paddles of LAND's first plane. Each of the VETO paddles is a strip of the same plastic scintillator used in LAND and measures 2 m long by 10 cm wide and 5 mm thick.

Neutrons will pass through the VETO without interacting whereas charged particles will deposit enough energy to be recorded (see Figure 3.5.3). Any event in LAND can then be identified as a charged particle if it is detected in coincidence with the VETO, the conditions for coincidence in the ASY-EOS experiment were defined as being hits in corresponding paddles of both the VETO and the 1st plane of LAND which were separated by no more than 10 cm in position and 1.5 ns in time.

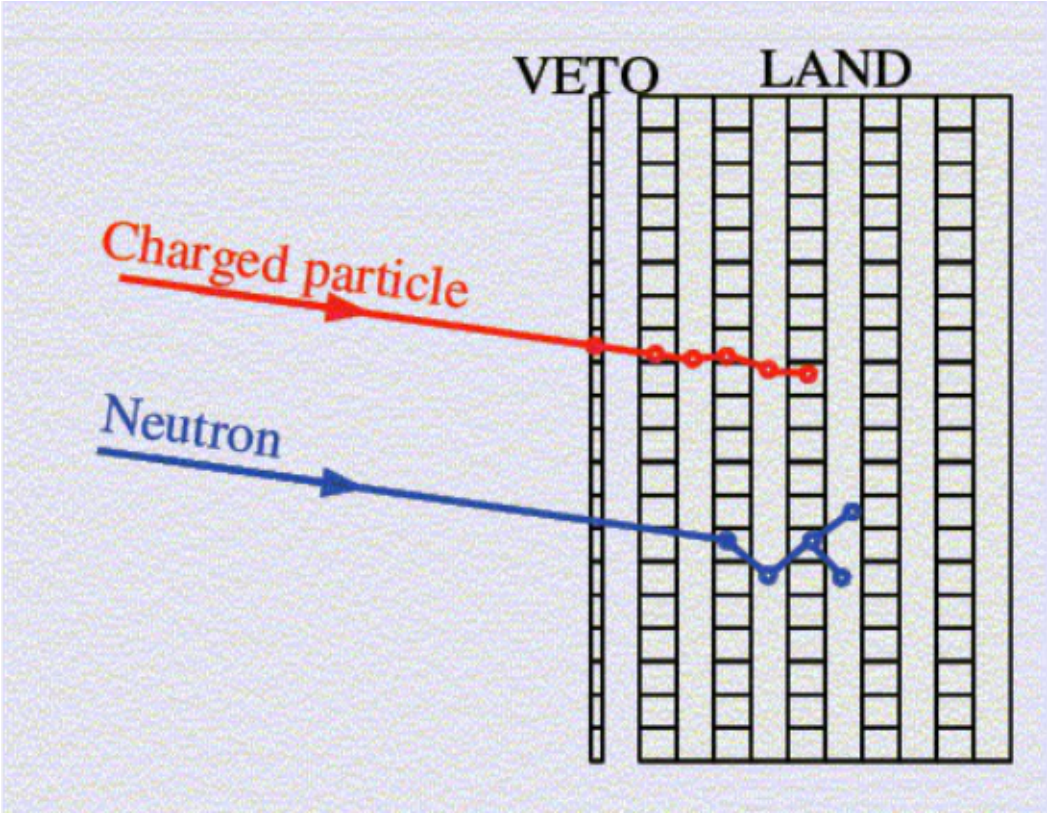

Figure 3.5.3: Schematic diagram illustrating interactions of charged particles and neutrons with LAND.

3.5.3 TacQuila[17] Timing System

During this experiment the LAND detector used a new set of timing electronics called TacQuila[17] which promised time resolution on the order of $\sigma = 10$ ps [62]. The system is called TacQuila[17] because each of the electronics boards has 16 channels plus 1 extra channel. The 17th channel is a common stop which receives its signal from the Start detector via a delay circuit. This signal stops the time measurement on all of the other channels. The value returned from the 17th channel is called tac_{17} or sometimes t17.

To measure the time at which a signal is detected in one of the LAND photomultipliers the TacQuila[17] system uses 2 TAC (Time-to-Amplitude Converter) channels and an external 40MHz clock. The first TAC channel, which can be

any of the first 16 channels on the TacQuila board, measures the time of arrival for the particle relative to the clock cycle. This means that the TDC only needs to operate over a range of 25 ns, thus allowing the very high timing resolution of this system. The first TAC channel (tac_{ch}) starts timing when the particle is detected in LAND and stops at the leading edge of the next clock cycle. A counter then records the number of clock cycles until the stop signal is received at the 17th TAC. Channel tac_{17} begins timing when this signal arrives and stops at the leading edge of the next clock cycle. See Figure 3.5.4.

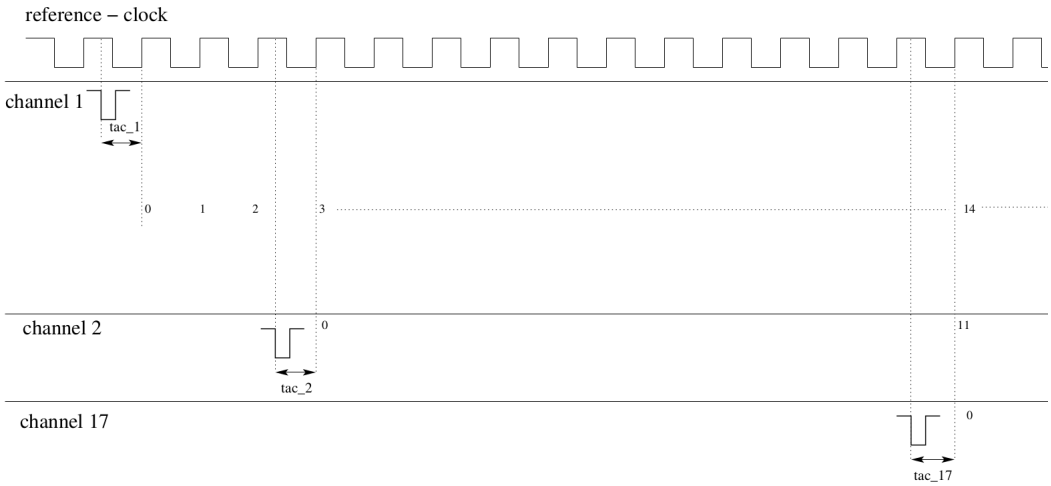

Figure 3.5.4: Timing diagram showing how the TacQuila TAC measurements are made against the external clock [62].

The calibrated values for tac_{ch} and tac_{17} are then used to calculate the calibrated time for a hit in LAND. This calibrated time ($tcal$) is the time between the signal from the photomultiplier being received and the arrival of the delayed common stop signal from the start detector:

$$tcal = tac_{ch} + \frac{counter}{frequency} - tac_{17} \tag{3.1}$$

If a tcal value is recorded for both photomultipliers of a particular paddle then these values, called $tcal_1$ and $tcal_2$, can be used to determine the time-of-flight and position of the hit within LAND. Further details of this procedure are given

in Sections 4.4 and 4.3, respectively.

3.6 KRATTA

The KRAkow Triple Telescope Array (KRATTA) [61] (see Figure 3.6.1) was used to measure the energy, emission angles and isotopic composition of the light charged reaction products. The detector was positioned 40 cm from the target covering a range of polar angles from 20-64° on the opposite side of the beam axis to LAND. KRATTA is composed of 35 modules which were arranged in a 7x5 array for the ASY-EOS experiment. Each module of KRATTA is composed of two optically decoupled CsI(Tl) crystals and three large 500 μm thick PIN photodiodes, see Figure 3.6.2.

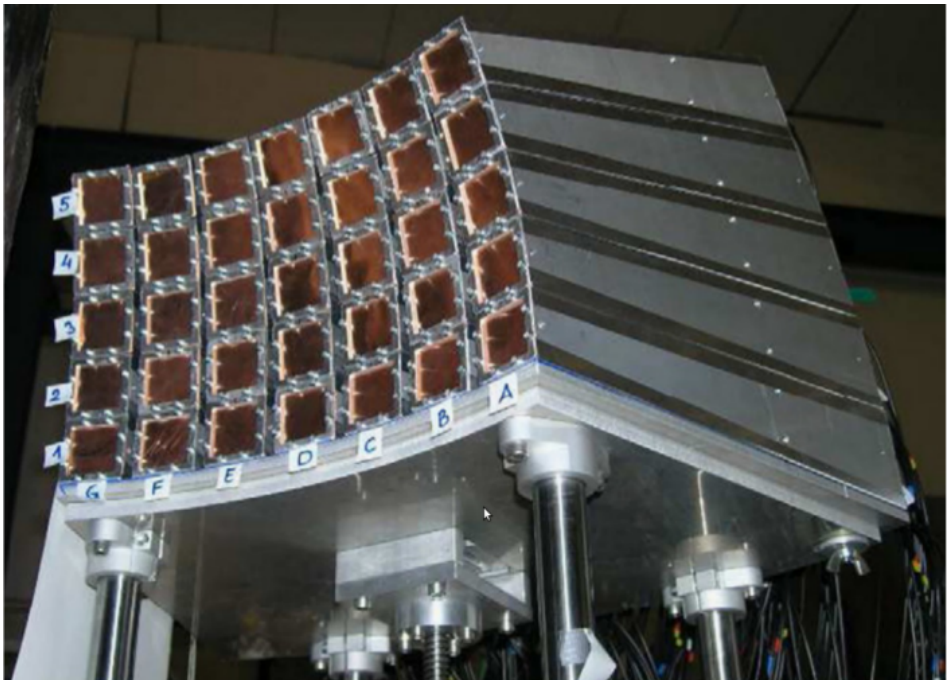

Figure 3.6.1: Image of the KRATTA detector taken in Cave C before the ASY-EOS experiment.

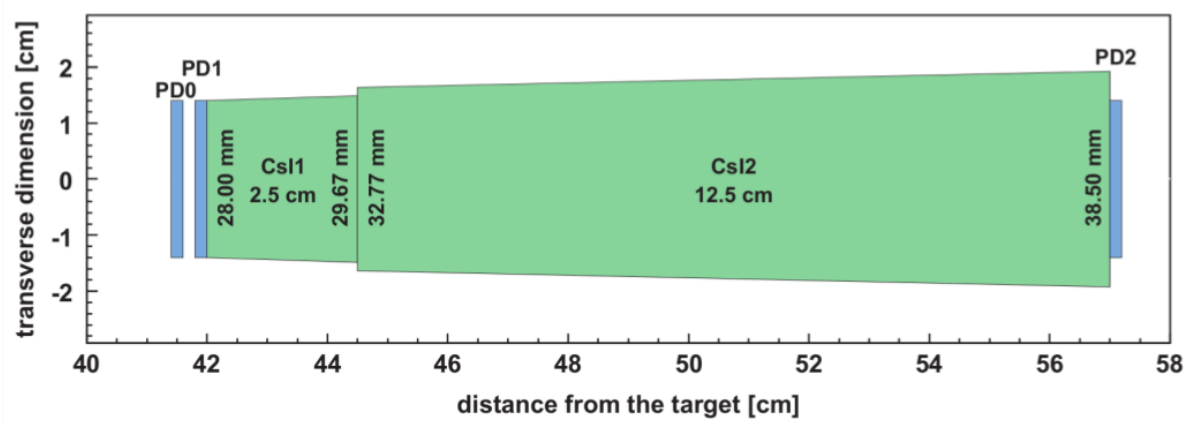

Figure 3.6.2: Schematic diagram of a KRATTA module [61].

The first photo-diode is used as a Si ΔE detector and only provides the ionisation signal, the second works in a "Single Chip Telescope" [61] configuration and reads the ionisation signal and the light output from the smaller crystal. The final photo-diode just reads the light from the larger crystal. In addition to the functions described above KRATTA was positioned so as to have a similar kinematic acceptance to LAND. This meant that it could also be used to measure the elliptic flow for light charged reaction products and corroborate the measurements of hydrogen elliptic flow made by LAND.

4 Calibration of LAND and VETO

This chapter outlines the procedures for calibrating the LAND and VETO detectors.

4.1 Cosmic Runs

The standard procedure for calibrating the LAND detector uses cosmic particles, mostly muons, which have enough energy to penetrate the concrete ceiling of the experimental cave above LAND. To ensure that only cosmic particles are recorded, a trigger is used which requires a signal to be detected in coincidence with a minimum of 5 scintillator paddles. Cosmic runs are used to generate a large number of events evenly distributed along each paddle of LAND, which can be used to calibrate the detector. Roughly 150,000 cosmics events are required to perform reliable calibrations of position, time and energy in LAND [60].

4.2 Shadow Bar Runs

During the experiment a series of runs was conducted using the ^{197}Au target and 400 AMeV beam but a solid iron block, called the Shadow Bar, was placed between the target and the LAND detector. The data from these runs were used later to perform background subtraction in the data analysis. The reason for taking background measurements with an active beam is that the neutrons produced in the heavy-ion collisions will induce secondary reactions in the apparatus and

environment surrounding LAND, which will contribute to the total background. It was therefore necessary to use the shadow bar to absorb any reaction products which were emitted directly at LAND without affecting any of the other reaction products.

4.3 Position Calibration

The position of an event in LAND can be determined from the difference in the time at which the event is detected in the two photomultipliers at either end of the scintillator paddle. For the event shown in Figure 4.3.1 the time for the scintillation light to propagate from the point of interaction of a particle with the scintillator to a photomultiplier will be given by:

$$t_1 = \frac{x_1}{v_{sc}} \quad \text{and} \quad t_2 = \frac{x_2}{v_{sc}} \tag{4.1}$$

Were v_{sc} is the propagation velocity of scintillation light in the LAND scintillator material and is equal to 15.7 $\pm$ 0.3 cm/ns [60].

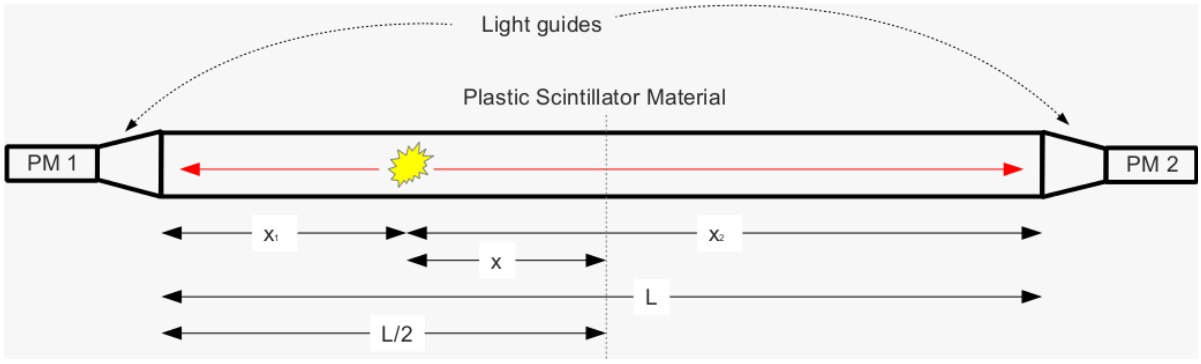

Figure 4.3.1: The figure shows scintillation light propagating through a paddle of LAND. x_1 and x_2 are the distances between the event and each photomultiplier. x is the position relative to the centre of the paddle. L is the length of the paddle (200 cm).

The position in the paddle, x, can be defined relative to the centre of the

paddle as:

$$x = \frac{t_2 - t_1}{2} * v_{sc} \tag{4.2}$$

t_1 and t_2 are not directly measured in LAND but are incorporated into the *tcal* output from TacQuila[17] (see equation 3.1). The *tcal* value is the time between when an event is recorded in the TDC and the arrival of the common stop signal which comes from the start detector via a delay circuit and so *tcal* can be expressed as:

$$tcal_1 = t_d - (t_f + t_1 + t_{pme1} + t_b) \tag{4.3}$$

where t_d is the time that the common stop signal takes to reach the TacQuila[17] board from the start detector, t_f is the time-of-flight of the detected particle from the target to LAND, t_{pme1} is the time that the electrical signal takes to reach the TacQuila[17] board from the LAND photomultiplier, t_b is the time that the beam particle takes to travel from the Start detector to the target. t_d and t_b are constant over all events and t_f will be the constant for any given event meaning that these quantities will cancel out when the difference between $tcal_1$ and $tcal_2$ is calculated.

$$tcal_1 - tcal_2 = (t_2 - t_1) + (t_{pme2} - t_{pme1}) \tag{4.4}$$

The uncorrected position, x_{uc}, in the paddle can then be determined using:

$$x_{uc} = (tcal_1 - tcal_2) * v_{sc} \tag{4.5}$$

In principle the position within the paddle can be determined using the equation 4.5 but differences in the cable lengths between the photomultipliers and the TacQuila[17] electronics boards can cause the determined position of an event to be offset by a value equal to $(t_{pme2} - t_{pme1}) * v_{sc}$.

The procedure for correcting this offset is to plot a histogram of the positions for a sample of cosmic particles and measure the mean position of the distribution, μ_c (see upper panel of Figure 4.3.2). It is assumed that the cosmic events are distributed evenly throughout the paddle so μ_c should equal zero, but the differences in the timing electronics mean that μ_c will actually be equal to the offset:

$$\mu_c = (t_{pme2} - t_{pme1}) * v_{sc} \tag{4.6}$$

A value $tdiff$ is defined for each paddle using the cosmic data. $tdiff$ is equal to half of $t_{pme2} - t_{pme1}$:

$$tdiff = \frac{\mu_c}{2v_{sc}} \tag{4.7}$$

All $tcal$ values are adjusted using the $tdiff$ value to remove the offset due to differences in the timing electronics:

$$tcor_1 = tcal_1 - tdiff \tag{4.8}$$

$$tcor_2 = tcal_2 + tdiff \tag{4.9}$$

The corrected position, x_{cor}, can now be determined (see lower panel of Figure 4.3.2):

$$x_{cor} = (tcor_1 - tcor_2) * v_{sc} \tag{4.10}$$

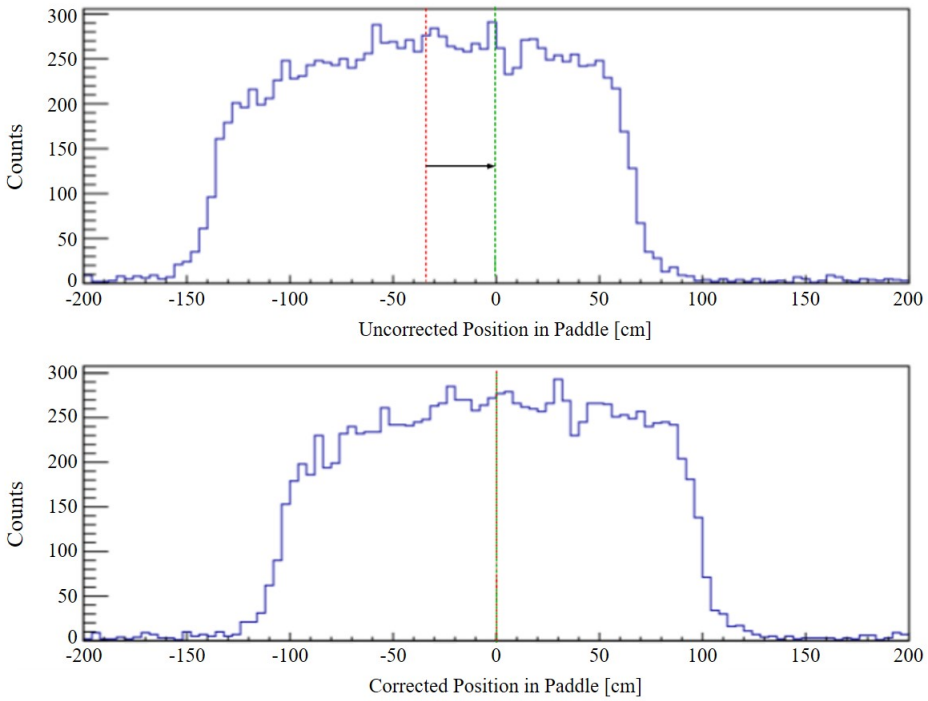

Figure 4.3.2: The upper plot shows the uncorrected position spectrum for cosmics events in LAND as determined by equation 4.5. The green line marks the centre of the paddle and the red line marks the mean of the distribution. The lower plot shows the position in LAND after the tcal values have been corrected.

4.4 Time Calibration and Synchronization

In addition to implementing the $tdiff$ correction it is also necessary to apply an additional correction, called tsync, in order to correct for the differences between the timing circuits of each of the paddles in LAND. Differences between the timing circuits of each paddle cause the time-of-flight measurements to be offset by a different value for each paddle. It is important to remove these differences from the time-of-flight data because accurate time-of-flight data are essential for the clusterization procedure in LAND.

This correction is applied by finding the difference between the timing circuit of each paddle with respect to a reference paddle, which in this experiment was paddle 107. The correction was applied by taking the time-of-flight spectra of

each paddle, integrated over a large sample of the direct unreacted beam data, and measuring the position of the beam peak for each spectrum. A correction factor, tsync, was calculated for each paddle by finding the difference between the peak of each time-of-flight spectrum and the peak of the spectrum from paddle 107.

4.5 Energy Calibration

It is also possible to measure the position of an event in a paddle using the QDC data from each photomultiplier. The position can in principle be found by taking the logarithm of the pulse height ratio for the two photomultipliers. However such a distribution will be skewed due to differences in the gain of each photomultiplier. Any differences in the gains can be equalised by producing a histogram of the logarithm of the pulse height ratios and applying a correction factor to each photomultiplier so that the distribution becomes centred on zero.

A simple test can be performed to check that the position calculated from the time data is concordant with that calculated from the energy. The position from time, hereafter referred to as pos$t$, and the position for energy, pos$e$, can be plotted against each other as shown in Figure 4.5.1. If the positions calculated are the same then you expect to see a single positive correlation between the two values but all of the plots of pos$t$ vs pos$e$ produced multiple positive correlations. The central feature of the plot (labelled B) shows the expected relationship between pos$t$ and pos$e$ but the other features shown in the plot (labelled A and C) indicate that, for some of the data, the positions calculated from energy and time do not agree. In addition it can be seen that some of the positions determined from the extracted tcal values are actually outside of the LAND detector and so must be incorrect.

After analysing the QDC and TDC data, the cause of this problem was found to be the new TacQuila[17] timing electronics. The problem was caused by the clock counter miscounting the number of clock cycles between the start and stop signals with the result that the returned value of tcal would sometimes be offset from its true value by an integer multiple of 25 ns. A siginificant fraction of the data was affected by this fault and the 25 ns shifts could occur in either direction, meaning that they could make the tcal values larger or smaller. This fault was present in the data from every photomultiplier in both LAND and the VETO detectors, in every run of the experiment.

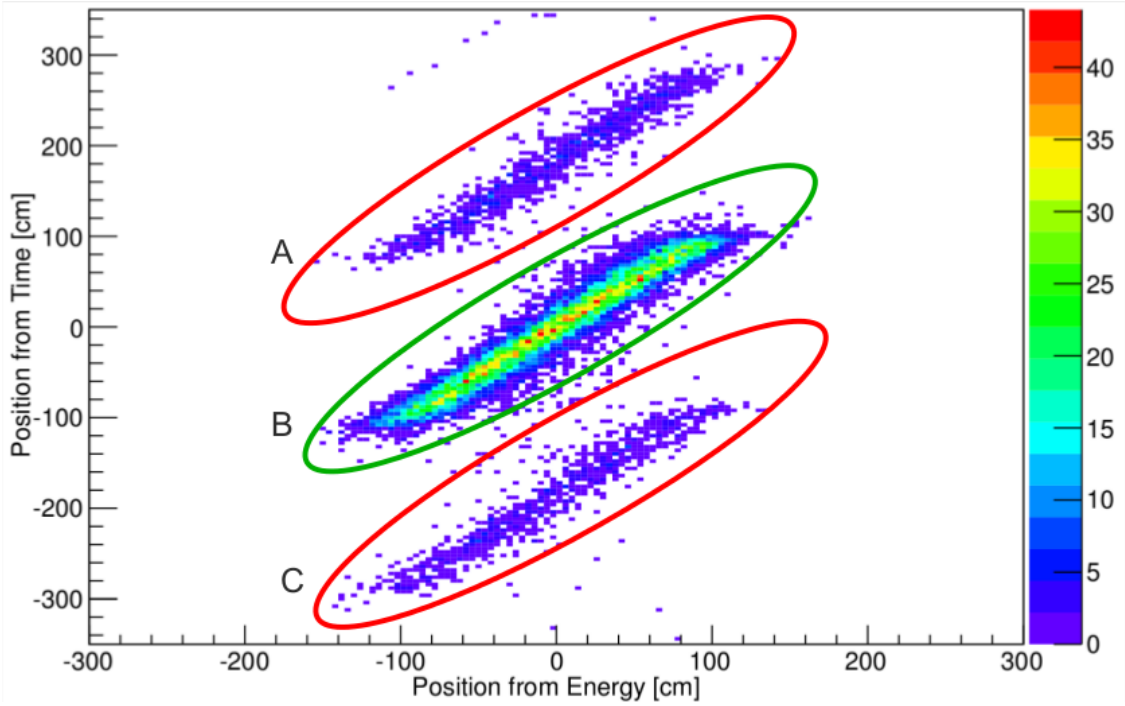

Figure 4.5.1: 2D histogram of position in LAND extracted from time measurement, pos$t$, against position from energy, pos$e$. In the region B the position determined from time is consistent with the position determined from the deposited energy. In regions A and C however the positions determined by these methods are not consistent due to a fault with the TacQuila[17] electronics.

4.6 Corrections to LAND Data

The fault with the TDC data identified in Section 4.5 resulted in significant delays to the data analysis process, whilst a procedure was developed to correct the data. The final correction procedure is outlined in this section and the development and implementation of these corrections constitutes a significant part of my contribution to the data analysis.

Because it is was the clock counter which malfunctioned, this meant that any corrupted data could be corrected by adding or subtracting a integer multiple of 25 ns to the tcal value. The most difficult part of the correction procedure was identifying which hits had been corrupted.

It is clear that any event found outside of region B in Figure 4.5.1 is likely to have suffered a 25 ns shift but it was impossible to tell from this plot which photomultiplier had been affected by the 25 ns jump because the faulty clock counter could cause either an increase or a decrease in the tcal value. An event could be shifted into section A either because $tcal_1$ had been increased by 25 ns or $tcal_2$ had been decreased by 25 ns.

In addition to this there were events in which both photomultipliers had experienced a 25 ns jump in the same direction; this meant that the position calculated for such an event would be consistent with the position from energy but the time-of-flight would be incorrect. A summary of the different ways in which the data could have been corrupted by these 25 ns jumps is displayed in Table 4.6.1.

It should be noted that time jumps larger than 25 ns are seen in the data but these constitute a much smaller fraction (less than 1%) of the data and these

PM1 time jump	PM2 time jump	Effect on position (cm)	Effect on time-of-flight (ns)
+25	0	+196.25	-12.5
-25	0	-196.25	+12.5
0	+25	-196.25	-12.5
0	-25	+196.25	+12.5
+25	+25	0	-25
-25	-25	0	+25

Table 4.6.1: The effect of the time jumps on the measured time of flight and position of a detected particle.

events have been excluded from the data analysis.

After extensive investigation of the data, a procedure was developed to correct the data using the plots shown in Figure 4.6.1 and Figure 4.6.2. Figure 4.6.1 corresponds to Figure 4.5.1 after it has been rotated clockwise by 45°. The horizontal lines drawn on the plot represent cuts. The lower cut is called tcutmin and the upper cut is called tcutmax. Any event which is not located between these cuts is identified as having a position determined from TDC data which is inconsistent with the position determined from the QDC data.

The plot in Figure 4.6.2 shows plots of the raw t17 channel value against the extracted *tcal* value for both photomultipliers of a paddle, where t17 is defined in section 3.5.3. There should be no correlation between the t17 value and *tcal*, which means that the data should be spread homogeneously over the plot area but 3 vertical features can be identified in the plot due to the 25 ns time shifts. Data in the left-hand feature have been shifted by -25 ns because the clock counter recorded 1 clock cycle more than it should have done, whereas data in the righthand feature are shifted by +25 ns due to the clock counter being incorrect by -1 clock cycle.

The plot shows that there is some relationship between the t17 channel value

and the probability that the clock counter will miscount. There appears to be an increased probability that the clock counter will count an extra clock cycle if the t17 value is high. Conversely the probability of counting one less clock cycle is increased at lower values of t17. The red graphical cuts marked on the plots are used to identify the data which has been shifted by ±25 ns. It should be noted that due to variations in the photomultipliers it was necessary to make different cuts on each PM tube. This means that 880 graphical cuts were required to correct the data from both the LAND and the VETO paddles.

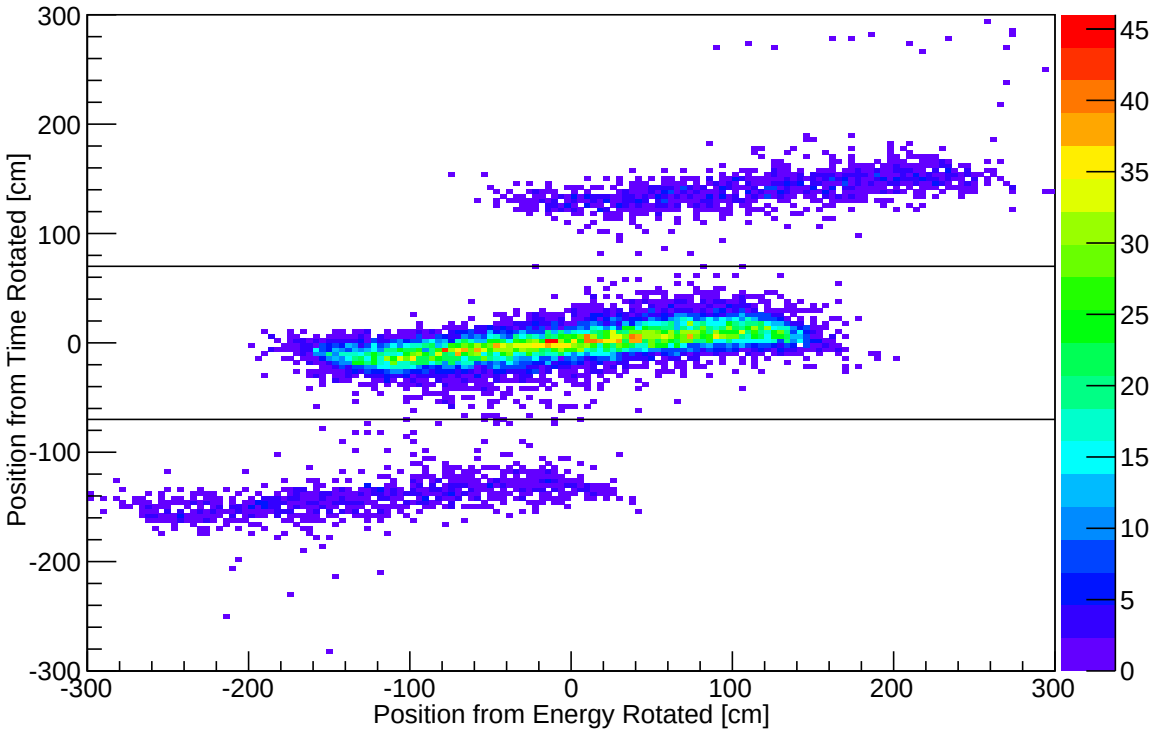

Figure 4.6.1: This is a rotated plot of Figure 4.5.1, clockwise by 45°. The horizontal lines on the 2D histogram are selection cuts. Any data located between the lines were considered to have a position determined from TDC data which is consistent with the position determined from the QDC data. The upper cut is called tcutmax and the lower cut is called tcutmin.

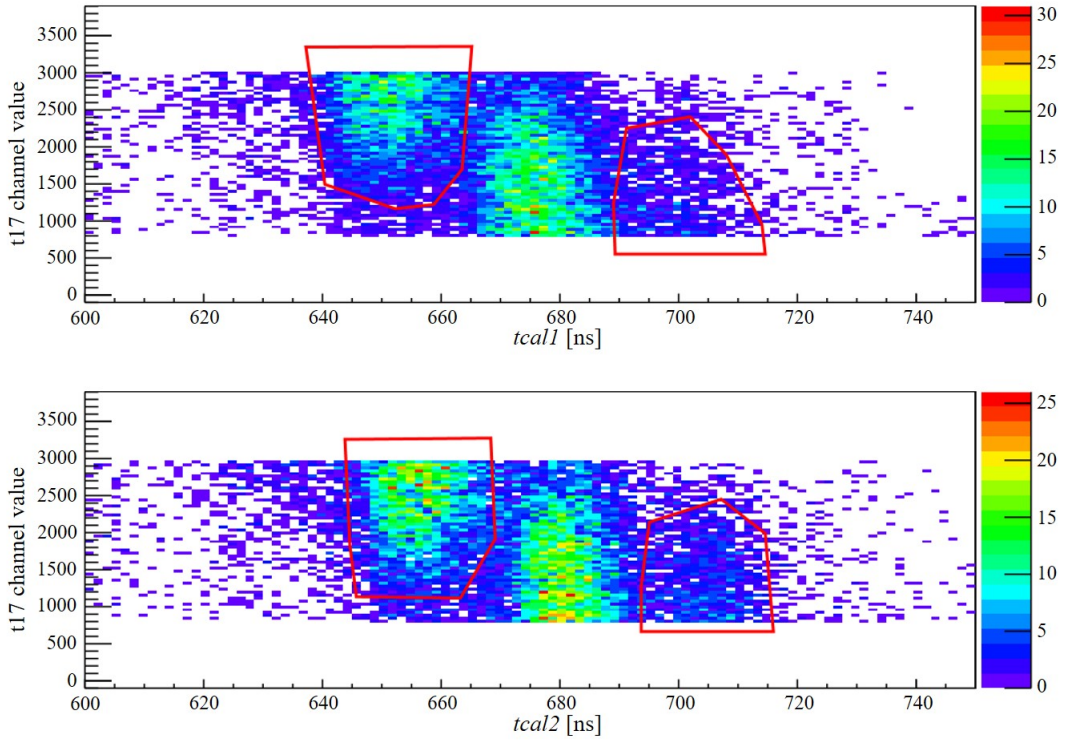

Figure 4.6.2: The upper plot is for photomultiplier 1 and the lower plot is for photomultiplier 2. Plots show the t17 value from the TacQuila[17] vs the extracted tcal values. There are 3 distinguishable vertical features whose centres are separated by 25 ns. The central feature contains data which have not been affected by the 25 ns time shift. The features on the left and right have been shifted by -25 ns and +25 ns respectively. Two graphical cuts are marked on each plot in red. The graphical cuts are referred to as follows: clockwise from the upper right hand cut - Cut1R, Cut1L, Cut2L and Cut2R.

The linear cuts from Figure 4.6.1 and the graphical cuts from Figure 4.6.2 are used to identify events which have suffered a 25 ns TDC shift and to determine how the data can be corrected. In order for an event to be identified as requiring correction it must either fall inside one of the graphical cuts and be outside region B in Figure 4.6.1 or fall inside two of the graphical cuts and be inside region B.

The procedure for correcting the data uses the linear cuts from Figure 4.6.1 and the graphical cuts from Figure 4.6.2 and is outlined in Table 4.6.2. The first column in Table 4.6.2 identifies in which region of Figure 4.6.1 the event

is located. The second and third columns show which graphical cuts the event is inside for the 1st and 2nd photomultipliers. The final two columns show the correction which is applied to the tcal values.

Region	GCut PM1	GCut PM2	Correction to $tcal_1$ (ns)	Correction to $tcal_2$ (ns)
B	None	None	0	0
B	Cut1R	Cut2R	-25	-25
B	Cut1L	Cut2L	+25	+25
A	Cut1R	None	-25	0
A	None	Cut2L	0	+25
C	Cut1L	None	+25	0
C	None	Cut2R	0	-25

Table 4.6.2: Table showing how the corrections are applied using the cuts in Figure 4.6.1 and Figure 4.6.2

The 2D histograms in Figure 4.6.3 and Figure 4.6.4 show the data after the correction has been applied. You can see that most of the corrupted data have been corrected but that a fraction remains uncorrected. The events found in regions A and C of Figure 4.6.3 have been subsequently excluded from the data analysis.

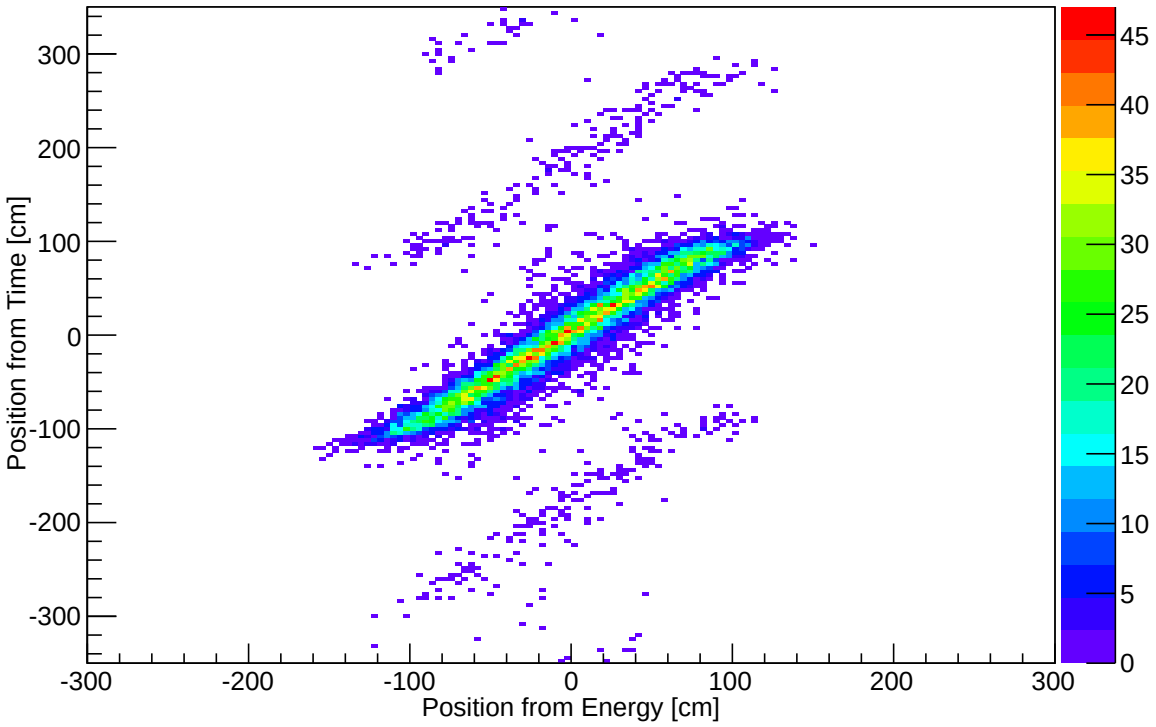

Figure 4.6.3: This histogram corresponds to that of Figure 4.5.1 after the correction has been applied to the data.

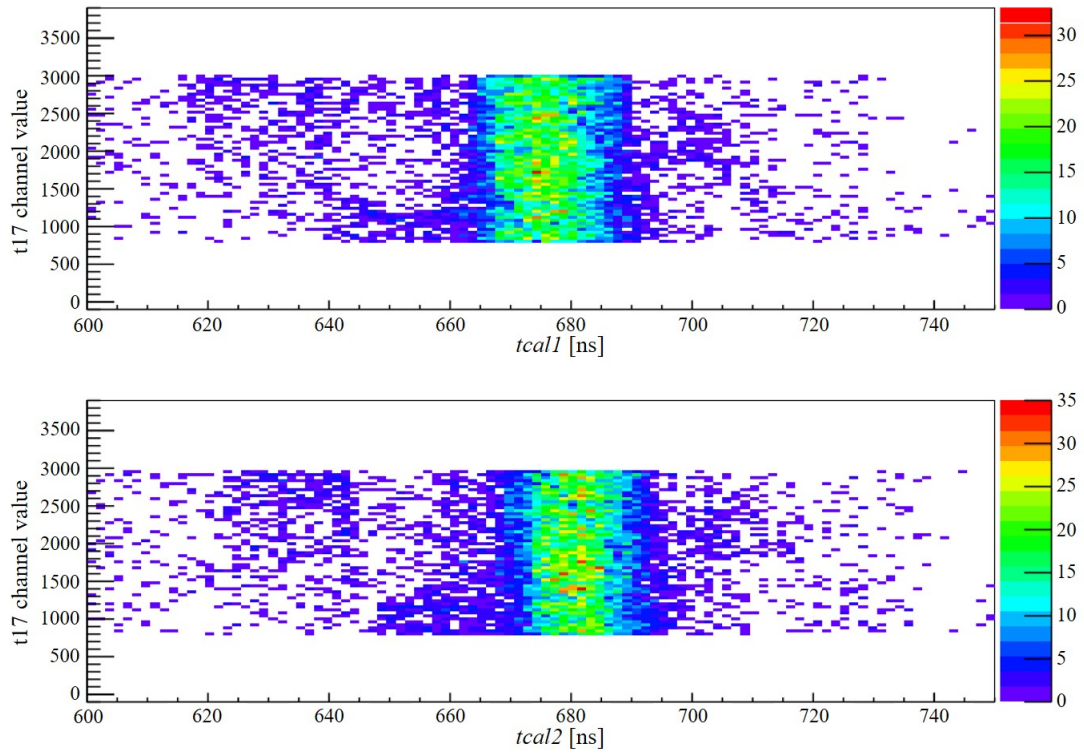

Figure 4.6.4: This histogram coresponds to that of Figure 4.6.2 after the correction has been applied to the data.

We estimate that typically in excess of 90% of the corrupted data are corrected by this procedure but there is some variation from paddle to paddle and it is therefore difficult to know this accurately due to the difficulties involved in identifying the corrupted data. It is expected that a small fraction of the detected particles which were not affected by the 25 ns TDC shift will have been erroneously corrected in such a way as to increase or decrease their extracted time-of-flight but it was expected that these mistakes could be corrected by comparison with the QDC data.

5 LAND Efficiency Simulations

In order to extract a value for γ from the analysis of the LAND data it was necessary to perform a set of simulations using UrQMD code so that the results of the flow analysis could be compared against the UrQMD model predictions. The UrQMD simulations were used to predict the v_2 ratio that should be observed in LAND for the values of $\gamma = 0.5$ and $\gamma = 1.5$ in the power law paramaterization of the symmetry energy. A linear interpolation was then performed between the UrQMD predictions for the v_2 ratio and the values extracted from the ASY-EOS experiment.

It was necessary to know the efficiency of LAND for detecting neutrons and small charged fragments as a function of kinetic energy so that the response of LAND could be accurately modelled in the UrQMD simulations. The efficiency of the detector did not need to be considered in the first stage of the analysis, which was performed by extracting v_2 ratios as a function of normalised rapidity, because the detected particles were divided into narrow rapidity ranges and the efficiency of LAND for neutrons and charged particles did not vary significantly within these rapidity bins. However, the second stage of the analysis (described in 7.2) involved integrating the elliptic flow measurements of neutrons and light charged particles over a very wide range of rapidities which meant that the detection efficiency of LAND would vary significantly across this range. It was essential to know how the detection efficiency varied with energy because particles which

had a higher probability of detection in LAND would make a greater contribution to the value of the integrated v_2 ratio.

The LAND detector has been in operation at GSI for over 2 decades and so the efficiency of the LAND detector for protons, neutrons and light charged fragments is well known [60]. Unfortunately in the ASY-EOS experiment the data from the 2nd plane of LAND were unusable and had to be omitted from the analysis and without the 2nd plane it was not possible to clusterize data from the 1st and 3rd planes accurately. This meant that only data from the VETO wall and the 1st plane of LAND could be used in the analysis and that the efficiency of LAND was effectively reduced. It was therefore necessary to perform Monte-Carlo simulations using Geant 3 to estimate the efficiency of LAND for protons, neutrons and other light charged fragments over the range of energies encountered in the ASY-EOS experiment.

The simulations were performed using the R3BRoot simulation code [63] over a range of energies from 50A.MeV up to 1400A.MeV for neutrons, $^{1}_{1}$H, $^{2}_{1}$H, $^{3}_{1}$H, $^{3}_{2}$He, and $^{4}_{2}$He. Each simulation consisted of 1000 randomly generated tracks spread over the entire area of LAND and each particle and energy was simulated seperately. Table 5.4.1 at the end of the chapter shows the full list of simulations along with their results.

5.1 Modelling LAND and VETO

R3BRoot contained a pre-existing geometry file for LAND which did not include the VETO wall. This file was modified by removing planes 2 to 10 and placing the 5mm thick VETO scintillator wall 13cm in front of the 1st plane of LAND.

5.2 Event Generator

The simulated particles were produced using a modified version of the R3BRoot Box generator. The energy and particle type are specified for each simulation and box generator randomly produces the particle trajectories. The generator had to be modified because it originally generated particle trajectories within a cone shaped region which meant that the simulated particles were only projected onto a circular region of LAND, see Figure 5.2.1. This meant that no particles were incident on the corners of LAND and this did not accurately replicate the conditions of the experiment. Furthermore the particles which hit close to the end of a paddle are important in an efficiency simulation because the efficiency of detection will tend to decrease towards the end of the paddles. This is because the scintillation light has to travel the entire length of the paddle to reach the photomultiplier at the far end so less energy is deposited at this photomultiplier and there is a higher chance that the total deposited energy will be below the threshold for the photomultiplier. This would result in the hit being registered by just one of the photomultipiers and it would be rejected. It was therefore important to ensure that particles were incident on the entire LAND detector to avoid overestimating the efficiency and so the box generator was modified to generate tracks which were incident over the entire detector. This was done by randomly generating the co-ordinates of a hit within the limits of the LAND detector and then generating a particle track that intersected with this point.

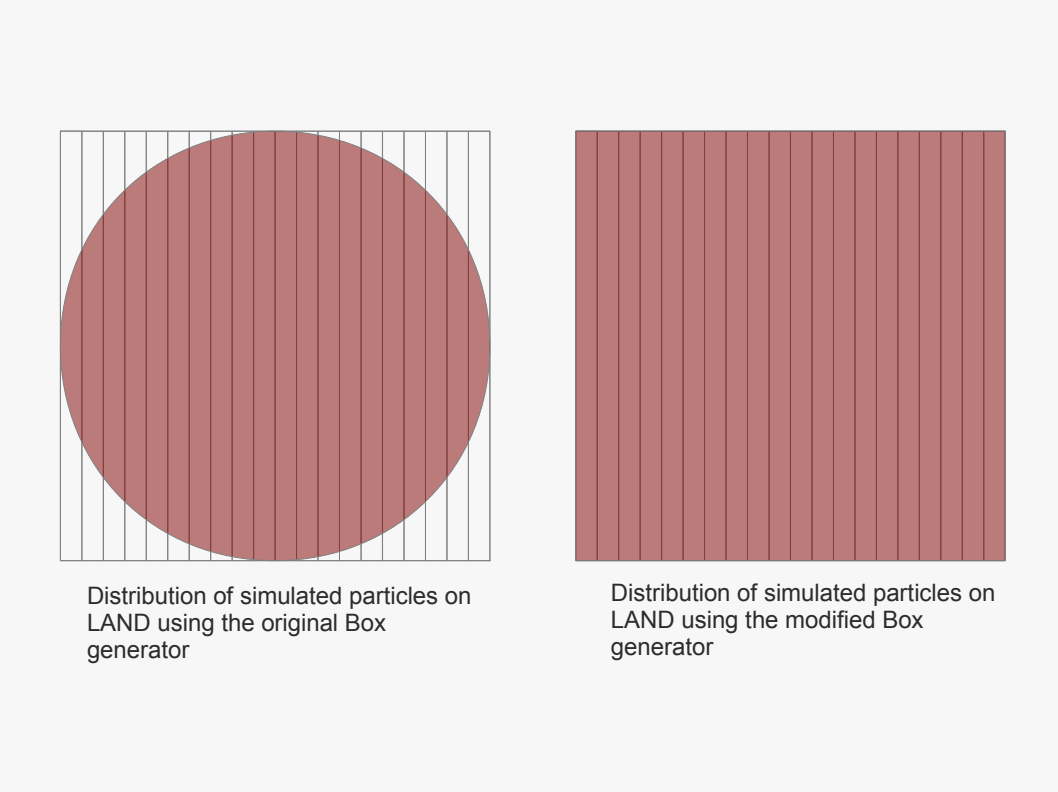

Figure 5.2.1: The figure shows the area of the front face of the VETO wall and LAND where simulated particle trajectories could intersect with the detector before and after the Box generator was modified.

5.3 Response of LAND and VETO

The response of LAND was modelled using the R3B Land Digitizer in R3BRoot. The LAND geometry was modified to include the VETO and all planes except plane 1 were removed. The digitizer simulated the response of the LAND electronics and determined whether a simulated particle would be recorded as a hit by LAND. The output from the digitizer was then analysed in exactly the same way as the real data up to the particle identification stage.

In order for a charged particle to be recorded as a hit it was required that each photomultiplier in the paddle must an energy greater than the pedestal thresholds used in the experiment. The positions of the hits in the VETO and LAND were required to be within 10cm of each other and be detected no more than 1.5ns

apart. Neutrons were required to deposit enough energy in LAND but leave no signal in the VETO.

5.4 Efficiency Simulations

The results of the Geant3 simulations, which are summarised in Table 5.4.1, show that the charged particles do not have enough energy to penetrate the VETO at energies below 50 AMeV making it impossible to detect them in LAND. Protons can penetrate the VETO above energies of 50 AMeV and the efficiency for isotopes of hydrogen increases to a peak of approximately 90% at around 100AMeV and then decreases steadily as the incident kinetic energy increases. This decrease in efficiency at higher energies occurs because the hydrogen isotopes do not deposit enough energy in the VETO to overcome the energy thresholds in the photomultipliers and be recorded as a hit. At very high energies (well in excess of 400AMeV) this leads to some hydrogen particles being erroneously identified as neutrons but this is not thought to be a serious issue because very few of the reaction products will have such high energies. The efficiency of helium isotopes is very stable above 70 AMeV and does not decrease significantly with energy because their higher mass and charge means that they always deposit enough energy in the VETO to be detected. Neutron efficiency increases steadily with energy but is typically around 20%. Figure 5.4.1 displays the simulated efficiency against kinetic energy for all simulated particles. The neutron efficiency is significantly lower than it would have been had we been able to use all the planes of the LAND detector. This will adversely affect the statistics in the experiment but the measurements of the directed and elliptic flow are not dependent upon detector efficiency.

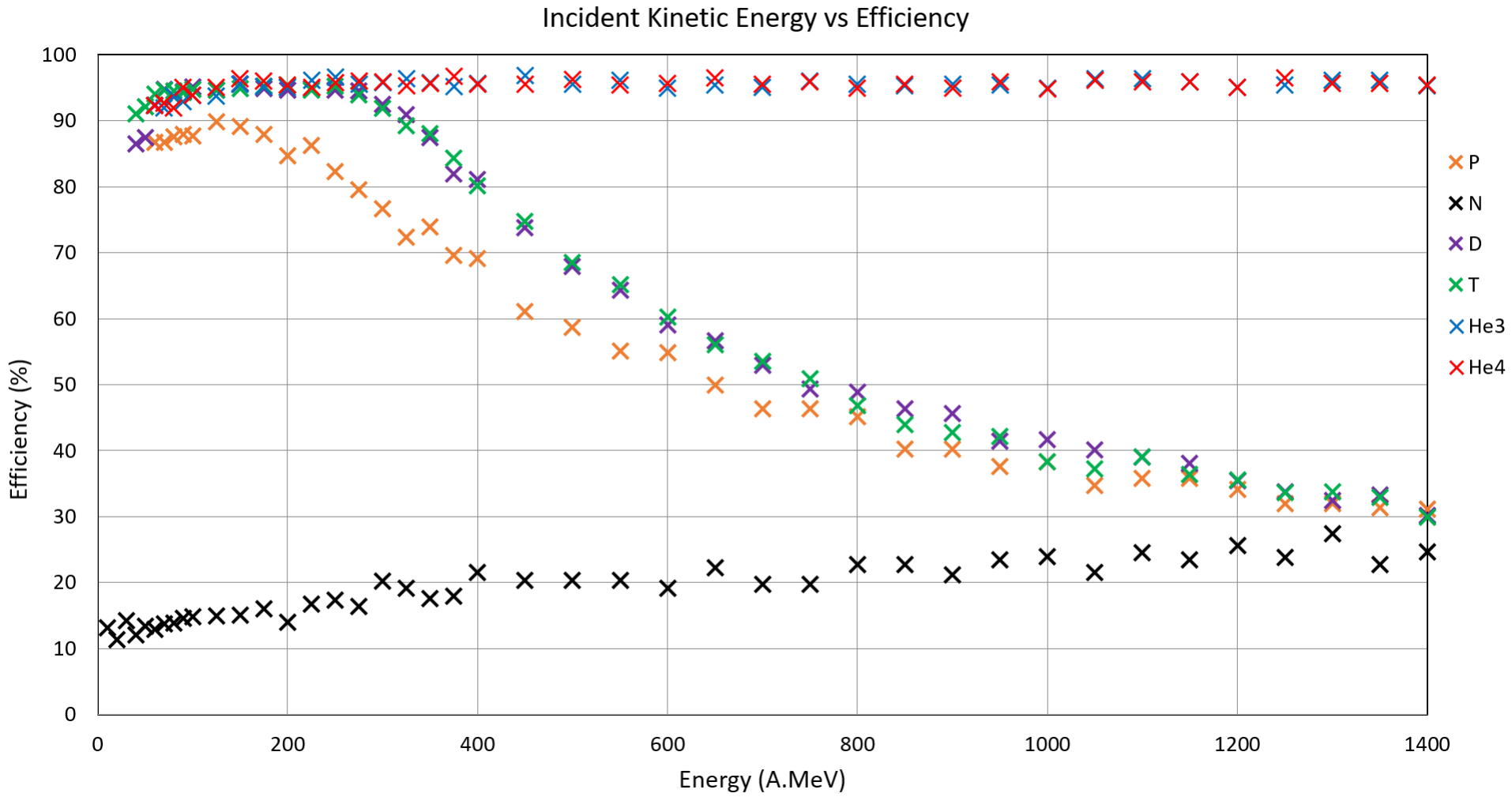

Figure 5.4.1: Plot showing the results of Geant3 simulations of detection efficiency in the VETO and 1st plane of LAND. Results are shown for protons, neutrons, deuteron, tritium, helium-3 and helium-4.

	Detection Efficiency(%)					
Energy(A.MeV)	$^{1}_{1}$H	n	$^{2}_{1}$H	$^{3}_{1}$H	$^{3}_{2}$He	$^{4}_{2}$He
10	0.0	13.1	0.0	0.0	0.0	0.0
20	0.0	11.3	0.0	0.0	0.0	0.0
30	0.0	14.2	0.0	0.9	0.0	0.0
40	0.1	12.1	86.5	91.0	0.0	0.0
50	0.2	13.4	87.5	92.1	0.0	0.0
60	86.7	12.9	92.4	94.1	0.0	92.3
70	86.7	13.7	94.8	94.7	92.0	92.7
80	87.6	13.9	93.7	94.5	93.8	91.9
90	87.9	14.6	94.4	94.3	92.9	95.1
100	87.7	14.8	95.1	94.8	93.9	93.9
125	89.8	15.0	94.6	94.6	93.8	95.1
150	89.1	15.1	95.6	94.9	95.5	96.4
175	87.9	16.0	94.9	95.2	95.2	96.0
200	84.7	14.0	94.7	95.4	95.1	95.4
225	86.2	16.8	94.9	94.7	96.2	95.1
250	82.3	17.4	94.7	95.3	96.6	95.8
275	79.6	16.4	94.5	93.9	95.5	96.0
300	76.7	20.2	92.5	91.9	95.8	95.9
325	72.4	19.2	90.9	89.2	96.4	95.3
350	73.9	17.6	87.4	88.1	95.8	95.7
375	69.6	18.0	82.0	84.3	95.2	96.8
400	69.1	21.6	81.1	80.2	95.7	95.5
450	61.1	20.3	73.8	74.7	96.9	95.6
500	58.7	20.4	67.9	68.5	95.6	96.3
550	55.1	20.4	64.3	65.2	96.2	95.4
600	54.9	19.1	59.1	60.3	95.0	95.7
650	50.0	22.3	56.7	56.0	95.4	96.5
700	46.3	19.7	52.9	53.6	95.1	95.5
750	46.4	19.8	49.3	50.9	96.0	95.9
800	45.1	22.8	48.9	46.8	95.6	95.0
850	40.2	22.8	46.4	44.0	95.3	95.6
900	40.2	21.2	45.6	42.8	95.5	94.9
950	37.6	23.5	41.4	42.2	95.4	95.9
1000	38.3	24.0	41.7	38.3	95.0	94.8
1050	34.7	21.6	40.1	37.2	96.4	96.1
1100	35.8	24.5	39.1	39.0	96.4	95.9
1150	35.8	23.5	38.1	36.4	95.9	95.9
1200	34.1	25.6	35.4	35.6	95.1	95.1
1250	32.0	23.8	33.8	33.6	95.4	96.5
1300	32.0	27.4	32.5	33.8	96.1	95.7
1350	31.4	22.7	33.3	32.9	96.2	95.7
1400	31.1	24.7	30.2	29.9	95.3	95.4

Table 5.4.1: The simulated detection efficiency of the VETO wall and the first plane of LAND, for neutorns and light charged particles.

6 Data Analysis

This chapter gives details of the analysis procedure used to ultimately extract a value of γ.

6.1 Determination of the Reaction Plane and Impact Parameter

As mentioned earlier, CHIMERA, MICROBALL and the TOF Wall were all used to estimate the reaction plane and impact parameter for each event. In order to ensure enough data were available, at least 4 hits were required in CHIMERA and 2 hits in MICROBALL. In order to estimate the reaction plane it is necessary to determine the laboratory rapidity, y_{lab}, and transverse momentum, $p_{\perp}$, of each particle. The estimated reaction plane can be characterised by a quantity called the Q-vector which is defined in equation 2.1.

The value of the weighting factor is determined by the rapidity of the detected particle relative to the centre-of-mass rapidity, y_{cm}. For the heavy-ion collisions. $y_{cm} = 0.448$ for the 400 A.MeV ^{197}Au+^{197}Au events. Particles with forward rapidity ($y_{lab} > y_{cm}$) are given a weighting factor of +1 and particles with backwards rapidity ($y_{lab} < y_{cm}$) are weighted by -1.

The weighting factors can be understood by recalling that the reaction plane is defined by the vector pointing from the target nucleus to the projectile nucleus

which is perpendicular to the beam axis. This means that in a mid-peripheral collision the spectator nucleons from the projectile will be deflected in such a way as to give them an average transverse momentum which is parallel to the reaction plane. Spectator nucleons from the projectile will typically have rapidities higher than the centre-of-mass rapidity and so it follows that the sum of the transverse momenta for high-rapidity particles will be parallel to the reaction plane vector. Conversely the spectators from the target nucleus, which will typically have lower rapidity, will be deflected in the opposite direction and so will have an average transverse momentum which is anti-parallel to the reaction plane.

Table 6.1.1 below summarises the rapidity ranges which were used to assign weighting factors to the detected particles used in the determination of the Q-vector.

w_n	y_{lab} Range
+1	$0.548 \leq y_{lab} < 1.048$
0	$0.348 \leq y_{lab} < 0.548$
-1	$y_{lab} < 0.348$

Table 6.1.1: Weighting factors used in the Q-vector calculations.

Particles in the range $0.348 \leq y_{lab} < 0.548$ are given a weighting factor of zero because this rapidity region is primarily populated by particles which have come from the overlap region of the heavy-ion collision and so the transverse momenta of these particles will not be as strongly related to the orientation of the reaction plane as it is the case for the spectator nucleons.

6.2 Particle Identification

A critical function of LAND was to distinguish between charged particles and neutrons. The principle behind this process was outline in section 3.5. The spe-

cific conditions for a hit in LAND to be classified as a charged particle were that there was also a hit in the VETO which occurred within 1.5 ns and 5 cm of the hit in the 1st plane of LAND. Hits in LAND which did not have coincident hit in the VETO would be classified as neutral. Ideally a neutron would be identified by clusterization of the secondary particles produced when the neutron interacts with one of the iron layers in the paddles. However this was not possible because of problems with the data from the 2nd plane of LAND which made it impossible to use most of the data from that plane. The paddles in the VETO, 1st plane and 3rd plane were all parallel to each other and were orientated to measure the vertical position of a hit. The paddles in the even numbered planes were orientated perpendicularly to the odd numbered planes so that the horizontal position of a hit could be measured. Without the horizontal position data from the 2nd plane it was not possible to clusterize hits in the 1st and 3rd planes which meant that we were only able to use the VETO wall and the first plane of LAND. This decreased the efficiency with which LAND could detect neutrons and meant that the statistics for the neutron data were lower than expected.

6.3 Extraction of Directed and Elliptic Flow

The first stage of the data analysis was to extract the directed and elliptic flow, v_1 and v_2 values respectively, and plot them as a function of rapidity. After events in LAND had been classified as neutral or charged the detected particles were further sub-divided into groups which were defined by cuts in the rapidity of the particles which were be determined using equation 2.2:

$$y_{lab} = \frac{1}{2} ln \frac{E + p_L}{E - p_L} \tag{2.2}$$

The rapidity groups applied in the analysis are detailed in Table 6.3.2 below.

There were 18 groups in total, 9 groups for charged particles and 9 for neutrons.

Group	Rapidity Range
1	$0.05 \leq y_{lab} < 0.15$
2	$0.15 \leq y_{lab} < 0.25$
3	$0.25 \leq y_{lab} < 0.35$
4	$0.35 \leq y_{lab} < 0.45$
5	$0.45 \leq y_{lab} < 0.55$
6	$0.55 \leq y_{lab} < 0.65$
7	$0.65 \leq y_{lab} < 0.75$
8	$0.75 \leq y_{lab} < 0.85$
9	$0.85 \leq y_{lab} < 0.95$

Table 6.3.2: Rapidity ranges used to seperate data into groups before extracting the directed and elliptic flow.

After each event had been placed into the appropriate rapidity group the azimuthal angle relative to the reaction plane was determined for each particle. Histograms were produced to show the azimuthal distributions of charged and neutral particles for each rapidity range shown in Table 6.3.2. These plots are shown in Figure 6.3.1 and Figure 6.3.2.

In Figure 6.3.1 the top row of plots shows the azimuthal distributions of charged particles in the rapidity ranges below mid-rapidity. Particles in these rapidity ranges will predominantly originate from the spectator region of the target nucleus. The plots on the middle row show the azimuthal distributions of the particles from the mid-rapidity region. Particles in this region will mostly originate from the overlap region of the heavy-ion collision. The plots on the bottom row show the azimuthal distributions for particles with higher rapidity.

There are very few charged particles identified in the lowest rapidity group (top left panel in Figure 6.3.1) and the statistics are thus very poor. This is possibly because these particles have the lowest energy and many might have been stopped in the VETO wall before they could reach LAND. This is not a

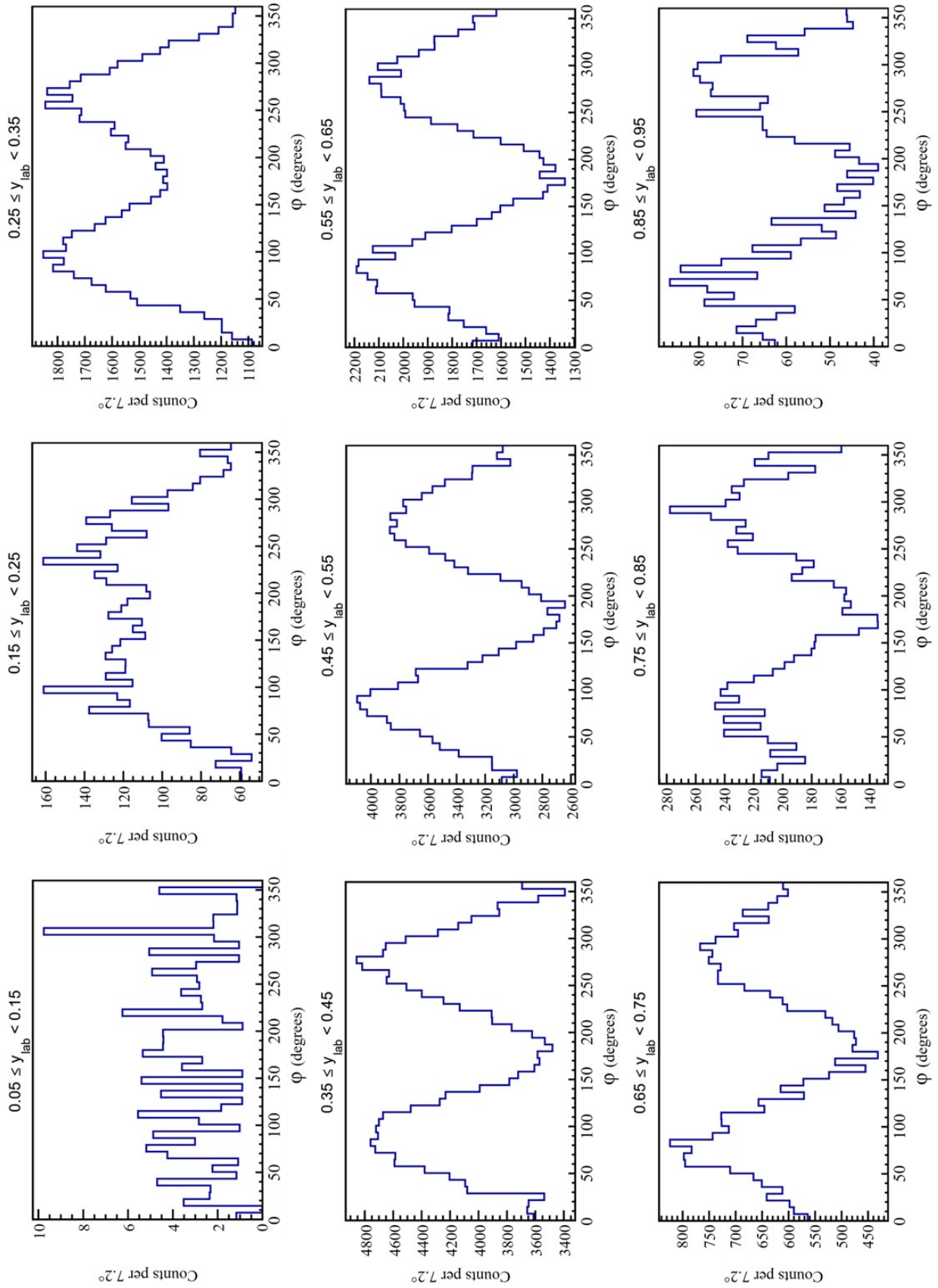

Figure 6.3.1: Azimuthal distributions obtained for charged particles detected in LAND in each rapidity range. Angles are measured relative to the reaction plane. The y-axis for each plot is counts per 7.2°. The x-axis for each plot is the azimuthal angle relative to the reaction plane of the event.

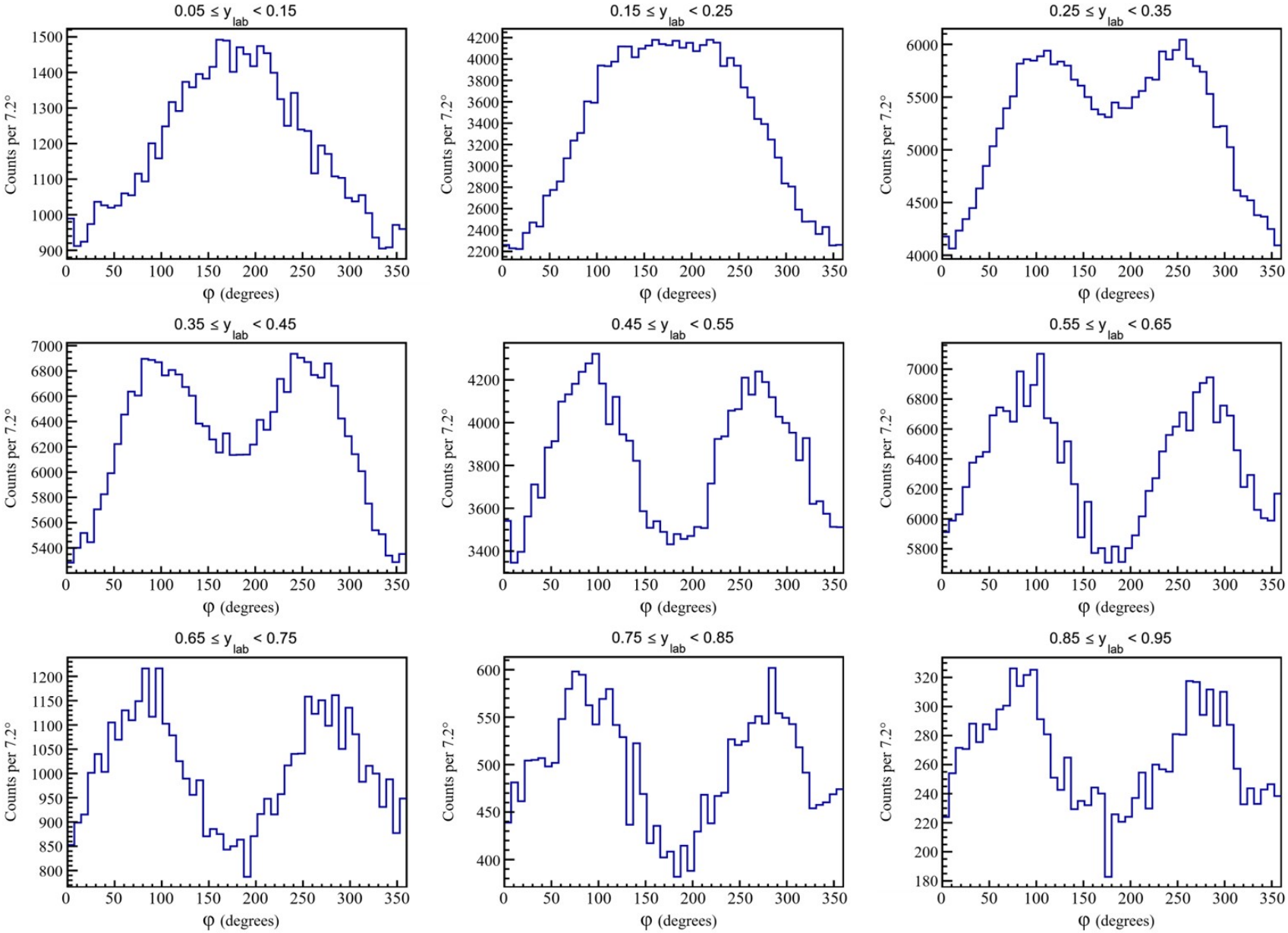

Figure 6.3.2: Azimuthal distributions obtained for neutral particles detected in LAND in each rapidity range. Angles are measured relative to the reaction plane. The y-axis for each plot is c ounts per 7.2°. The x-axis for each plot is the azimuthal angle relative to the reaction plane of the event.

significant issue because most of the particles in this rapidity range will originate from the spectator region of the target nucleus. We expect to see a peak around 180° in the lower rapidity plots which shows the directed flow from the target nucleus but this peak is not visible in the first plot due to the poor statistics.

The statistics for charged particles improve as rapidity increases as the plots move towards the mid-rapidity region. There are two peaks, located around 90° and 270°, which begin to appear as the plots approach the mid-rapidity region. These peaks indicate that a greater number of mid-rapidity charged particles are detected at azimuthal angles which are perpendicular to the reaction plane and this azimuthal anisotropy is the elliptic flow of the charged particles. The 180° peak, due to the directed flow, is visible in the second plot but it is obscured by the elliptic flow in the third plot.

As we move into the high-rapidity ranges the statistics begin to decrease. This is mainly because there are fewer particles ejected from the heavy-ion collision at such high energies but also because some of the high-energy charged particles may not deposit enough energy in the VETO to be detected. This may lead to some high-energy charged particles being incorrectly identified as neutrons. This should only account for a small fraction of the charged particles in this rapidity range and it should not significantly affect the results of the analysis because the majority of these particles will originate from the spectator region of the projectile nucleus.

The particles ejected from the overlap region should be found mainly in the mid-rapidity ranges and so we expect that the 90° and 270° peaks should disappear at higher rapidities. In addition to this a new peak should appear around 0° due to the directed flow of particles from the projectile nucleus. Instead we see

that the elliptic flow peaks are present in all the high-rapidity plots and there is no sign of a peak around 0°.

The unexpected results observed in the high-rapidity regions are most likely caused by the correction procedure described in 4.6. When trying to correct the time jumps in the TacQuila[17] timing system it is possible that a small fraction of the mid-rapidity events were erroneously moved to the higher rapidities. This is possible if the correction procedure was applied to an event which was unaffected by the TacQuila time jumps but was incorrectly identified as being corrupted. If 25 ns was added to the tcal value of such an event then it would appear to have a shorter time-of-flight which would make it appear to have a higher rapidity. It should have been possible to filter out any such events from the analysis by comparing the TDC and QDC data for each event but this was not possible because of the problems with the QDC data from LAND.

A typical heavy-ion collision will produce far more particles in the mid-rapidity region than at high rapidity which means that moving even a very small fraction of the mid-rapidity data into the high rapidity region will dilute the high-rapidity data to the point that they are completely obscured by the transplanted data from the mid-rapidity region. This meant that the high-rapidity data could not be used in the final analysis.

An additional concern is that if the correction procedure moved mid-rapidity particles into the high-rapidity region then it is probable that similar mistakes in the correction procedure have polluted the low and mid-rapidity data with particles from other rapidity regions. However, the effects of these shifts will be less pronounced than what we have seen in the high-rapidity data because there are a greater number of particles detected in the lower to mid-rapidity ranges

which means that the data will not be diluted as strongly.

The neutron data show very similar patterns to the charged particle data. We can still see the elliptic flow appearing at mid rapidity and then extending into high rapidity due to the time jump corrections. The directed flow appears more clearly for neutrons at low rapidity than it does for charged particles, which is probably due to the higher statistics in the neutron data.

6.4 Reaction Plane Anisotropy

After producing these raw azimuthal distributions from the LAND data, the next step was to correct the distributions for anisotropies in the reaction plane determination. Figure 6.4.1 is a histogram showing all orientations of the reaction plane for all good events used in the analysis. The reaction plane is defined by an azimuthal angle measured relative to the laboratory, all the azimuthal angles for the charged and neutral particles in an event are measured relative to the reaction plane of that event. The reaction plane distribution should be flat because the orientation of the reaction plane is random. However, anisotropies can appear due to a bias in the detector systems used to estimate the reaction plane, for example if one side of CHIMERA is more sensitive then it will be more likely that particles are detected on that side and therefore it will be more likely that the determined value of the reaction plane will point in that direction. In Figure 6.4.1 you can see that the estimated reaction plane points most often at a laboratory angle of 0° which implies that the elements of the detector systems on that side of the laboratory were more sensitive.

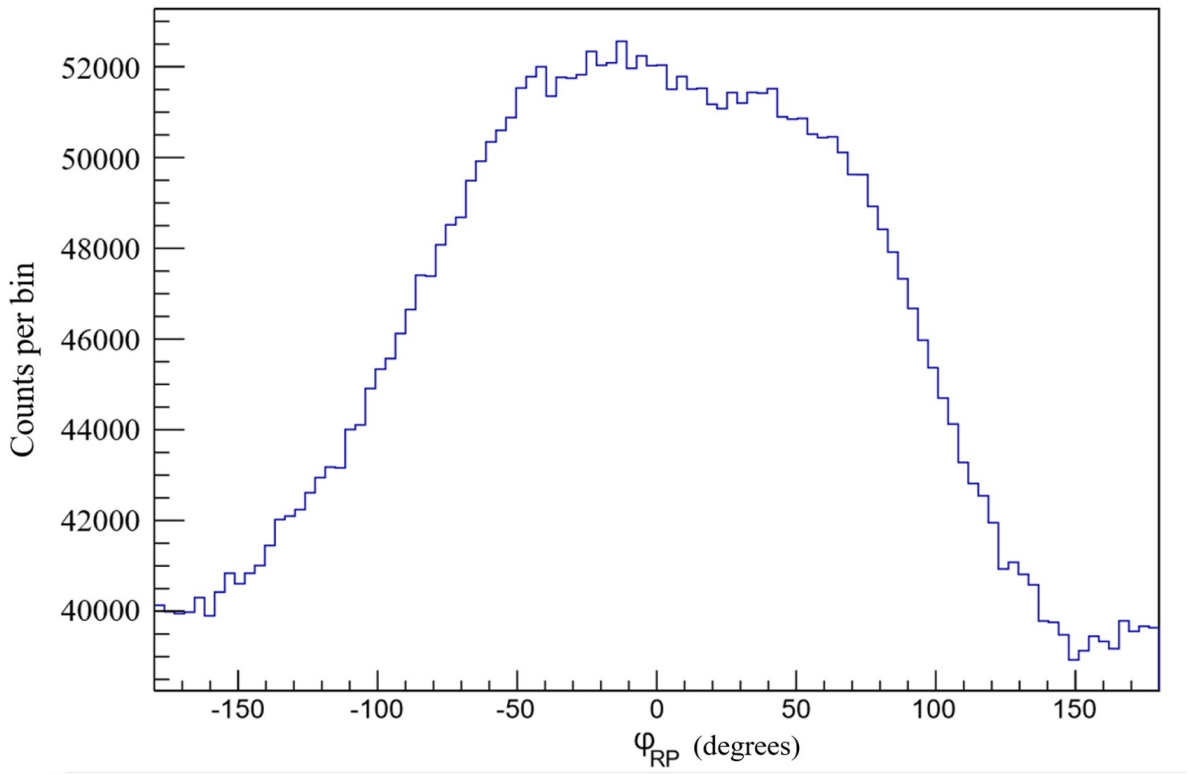

Figure 6.4.1: Plot showing the azimuthal angles of the reaction plane relative to the laboratory frame of reference as determined by CHIMERA, MICROBALL and the TOF Wall for all good events. ϕ_{RP} is the laboratory angle of the reaction plane which is defined in equation 2.1, were $\phi_{RP} = 0$ points to the left when looking down the beam axis (away from LAND).

These anisotropies in the reaction plane distribution will introduce a similar bias into the azimuthal distributions shown in Figure 6.3.1 and Figure 6.3.2 which partly explains why the elliptic flow peaks are not always the same height. The reaction plane bias can be removed from the data by weighting the data for each event based on the value of the reaction plane for that event.

The first step is to calculate the average bin value, b_{ave}, on the reaction plane histogram:

$$b_{ave} = \frac{\text{No. good events}}{\text{No. bins}} \tag{6.1}$$

Then a weighting factor, W_{bin}, is calculated for each bin range of the reaction

plane on the histogram:

$$W_{bin} = \frac{b_{ave}}{binvalue} \tag{6.2}$$

The final step is to apply the weighting factor to the histograms in Figure 6.3.1 and Figure 6.3.2. The histograms are repopulated but this time each hit which is added to the histogram is weighted by the factor W_{bin} according to which bin the event falls into on 2.2. This means that hits detected for an event which had a reaction plane value of 0° will count for less than those for events with a reaction plane value of 180°.

The azimuthal distributions which have been corrected for the reaction plane bias are shown in Figure 6.4.2 and Figure 6.4.3.

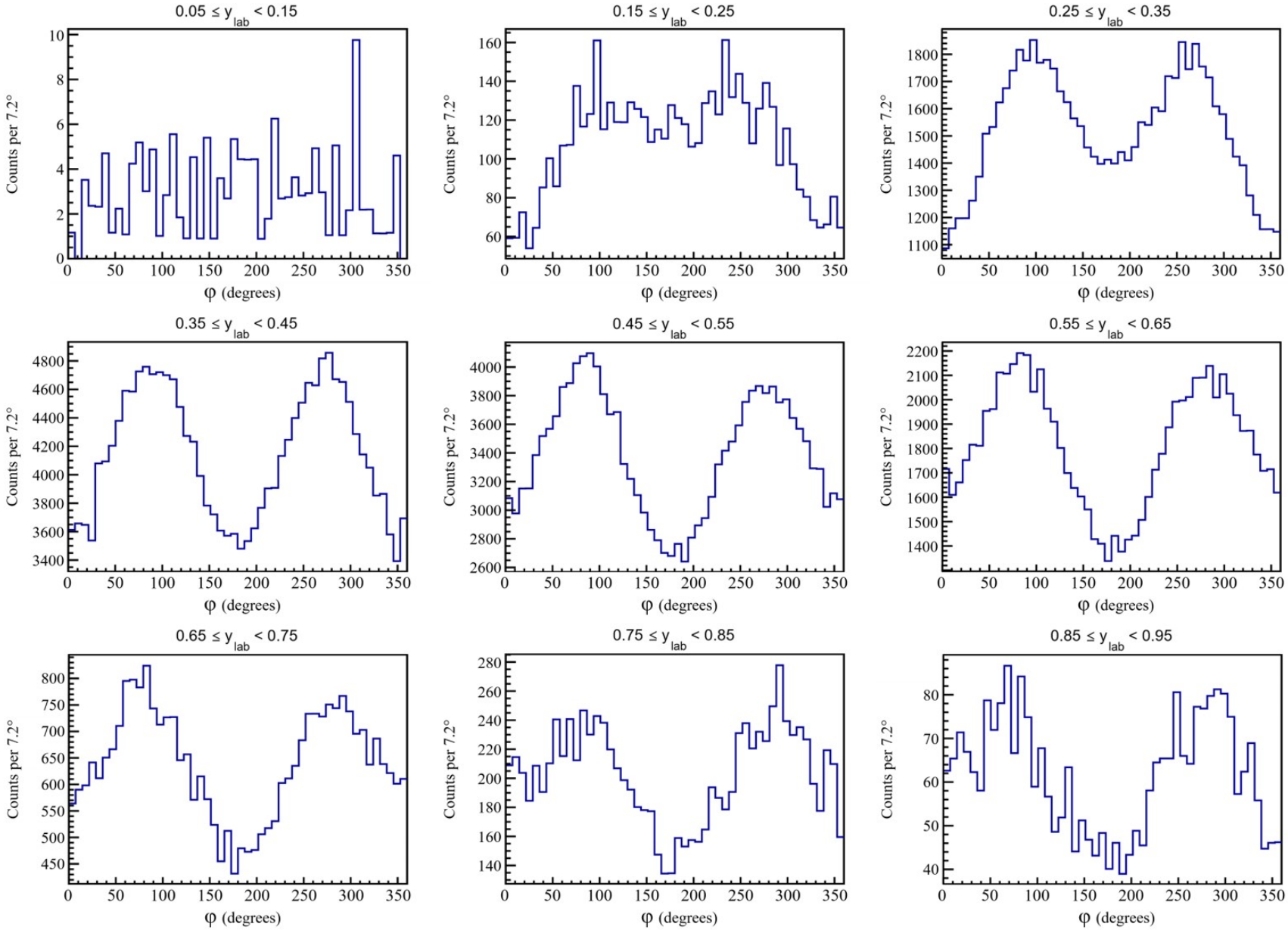

Figure 6.4.2: Azimuthal distributions obtained for charged particles detected in LAND in each rapidity range after correcting for the reaction plane bias. Angles are measured relative to the reaction plane. The y-axis for each plot is counts per 7.2°. The x-axis for each plot is the azimuthal angle relative to the reaction plane of the event.

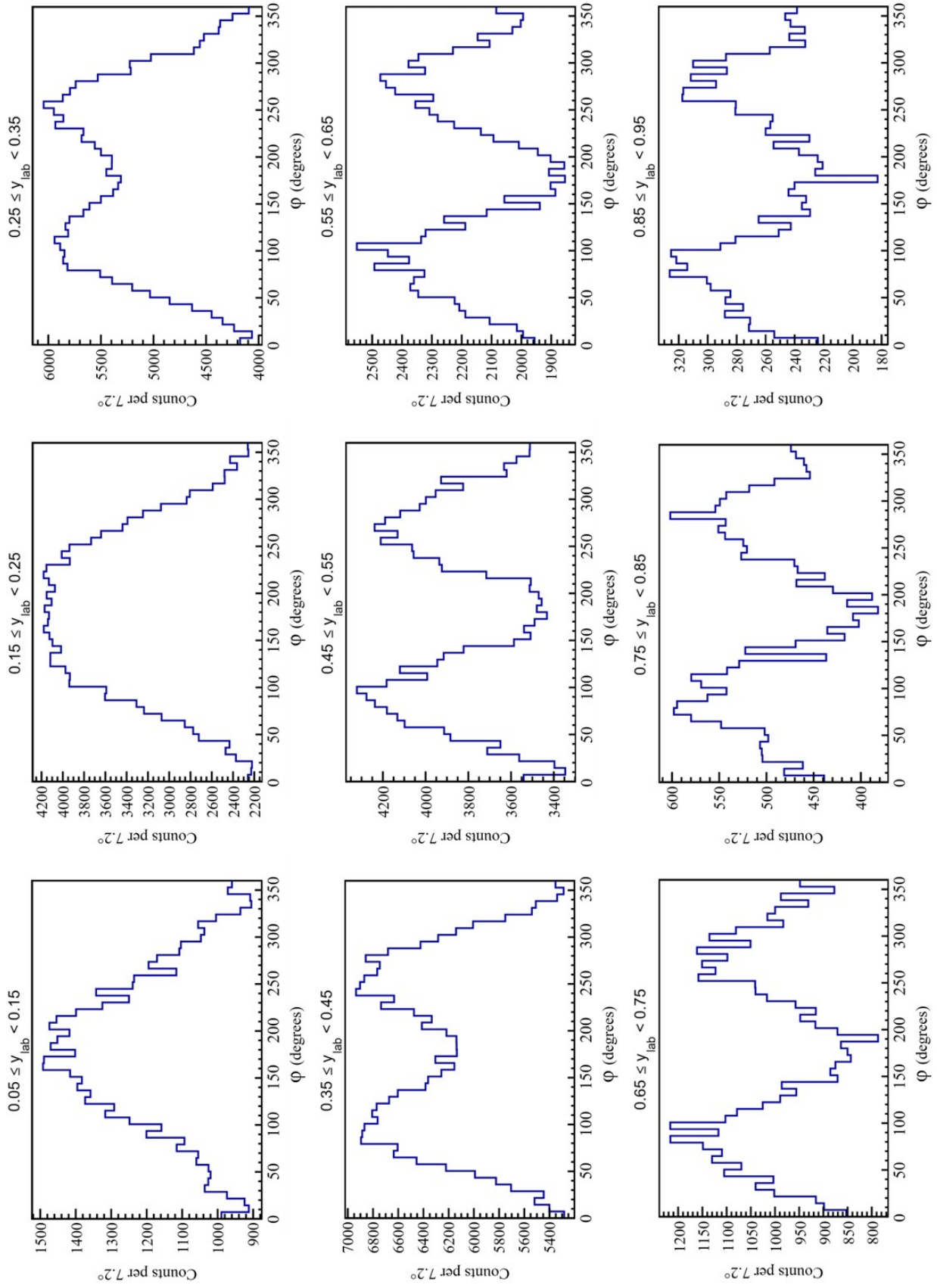

Figure 6.4.3: Azimuthal distributions obtained for neutral particles detected in LAND in each rapidity range after correcting for the reaction plane bias. Angles are measured relative to the reaction plane. The y-axis for each plot is counts per 7.2°. The x-axis for each plot is the azimuthal angle relative to the reaction plane of the event.

6.5 Background Subtraction

The next step in the analysis was to estimate the background radiation and subtract it from the azimuthal distributions. The background was measured in the shadow bar runs which used the same beam and target as were used in the main experimental runs but a large iron shield, called the shadow bar, was placed between the target and LAND. The shadow bar absorbed the particles which were ejected from the heavy ion-collision directly towards LAND but would not have affected any other products of the event. This approach was taken because the background radiation in the experiment cave will be different when the beam is present, due to neutrons produced in the heavy ion collisions being scattered by the apparatus and environment surrounding LAND and producing secondary particles which contribute to the background radiation.

In order to remove the background from the azimuthal plots it is necessary to perform exactly the same correction and analysis procedures on the shadow bar data as were performed on the data taken without the shadow bars. All of the steps outlined from chapter 4 up to and including section 6.4 are applied to the shadow bar data in order to produce azimuthal distributions of charged and neutral particles from the background radiation in the cave when the beam was present. These distributions can be seen in Figure 6.5.1 and Figure 6.5.2.

The statistics in the shadow bar data are much poorer than for the main experimental data. This is because the particle flux through LAND will be far smaller in the shadow bar runs due to the presence of the shadow bar but also because only 20 shadow bar runs are used in the analysis compared with 142 main beam runs for the primary data.

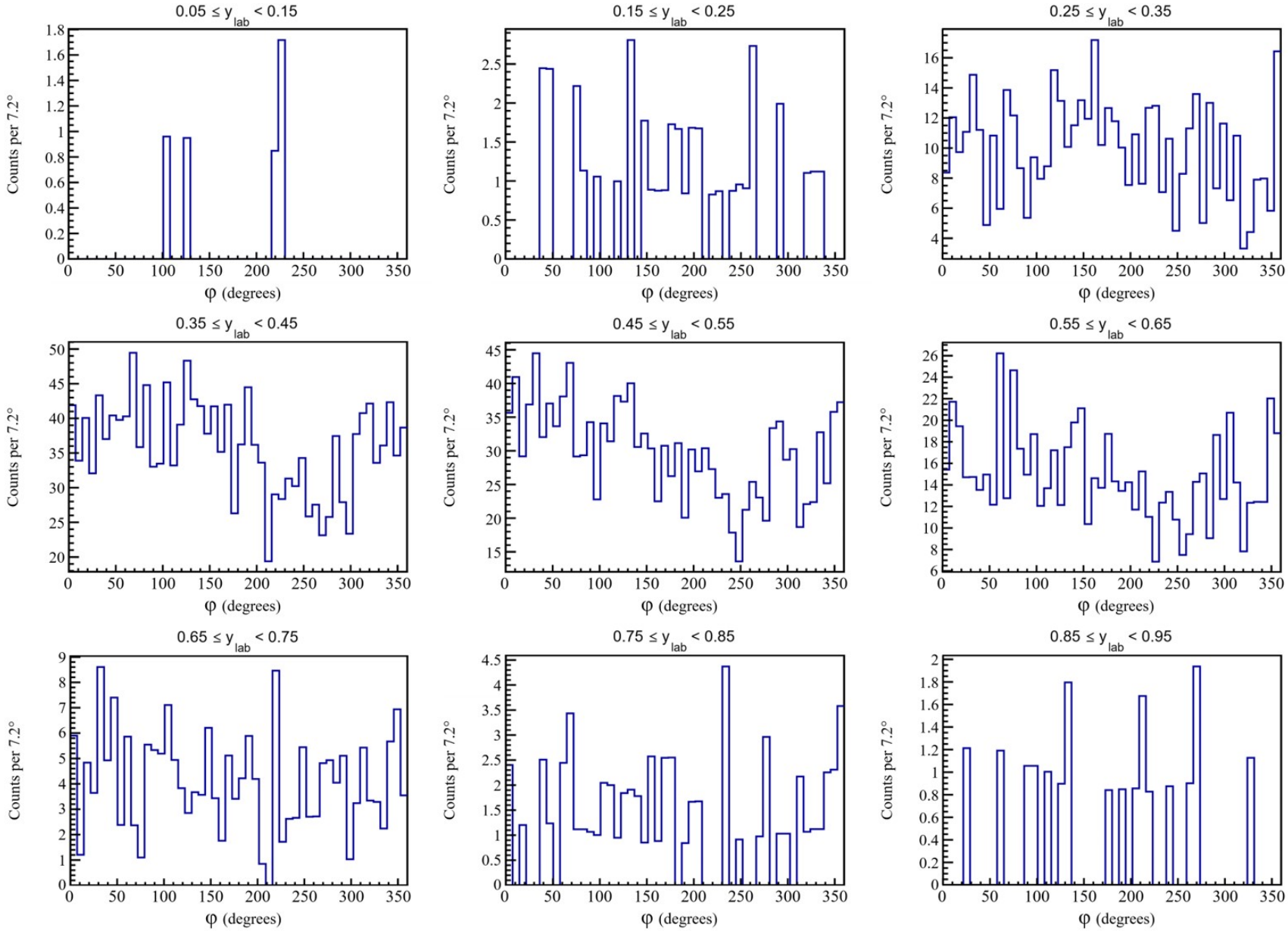

Figure 6.5.1: Azimuthal distributions obtained for charged particles detected in LAND in each rapidity range after correcting for the reaction plane bias, for shadow bar data. Angles are measured relative to the reaction plane. The y-axis for each plot is counts per 7.2°. The x-axis for each plot is the azimuthal angle relative to the reaction plane of the event.

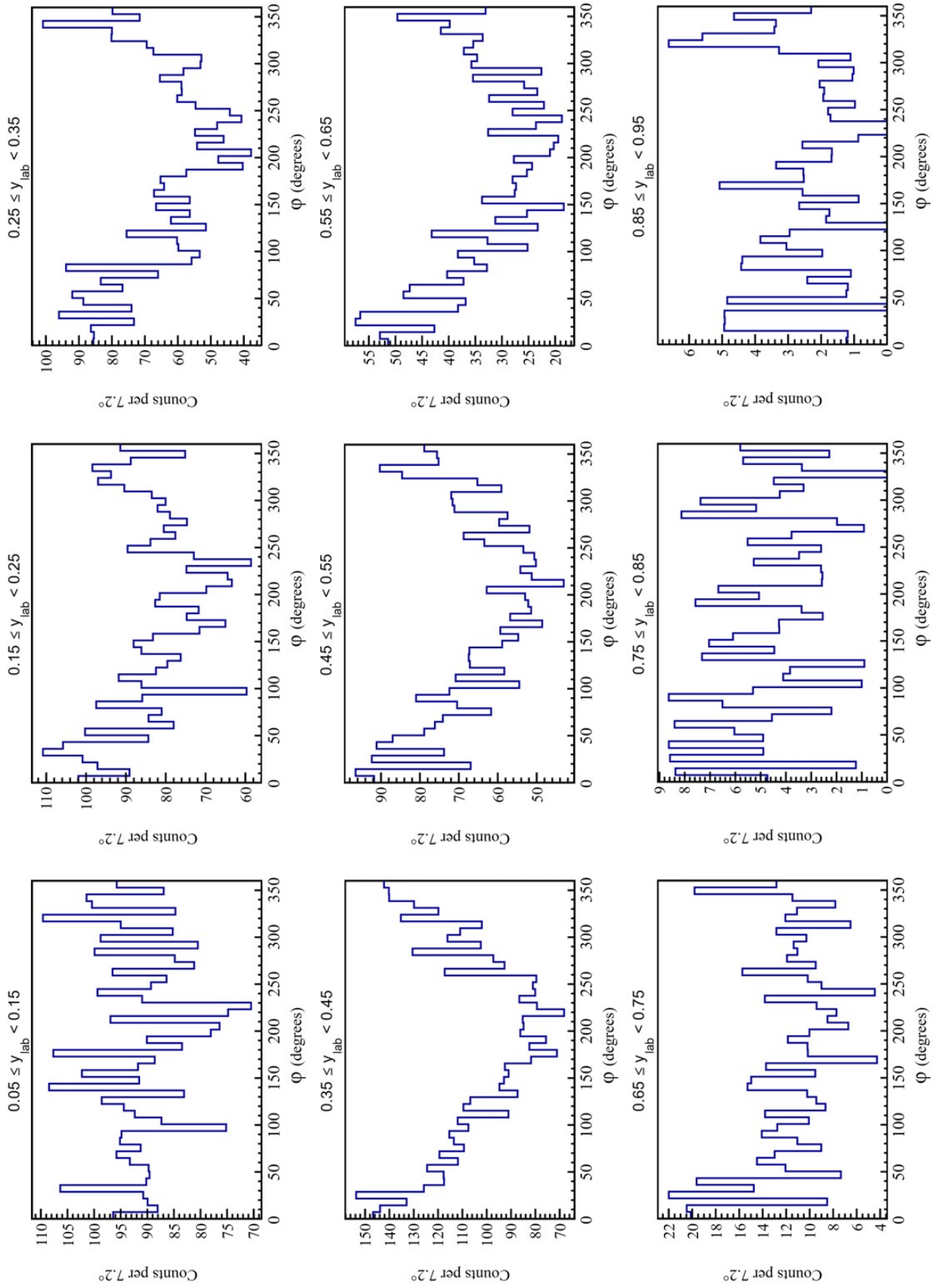

Figure 6.5.2: Azimuthal distributions obtained for neutral particles detected in LAND in each rapidity range after correcting for the reaction plane bias, for shadow bar data. Angles are measured relative to the reaction plane. The y-axis for each plot is counts per 7.2°. The x-axis for each plot is the azimuthal angle relative to the reaction plane of the event.

In order to subtract the background from the azimuthal distributions it is necessary to apply a weighting factor to the background because it was measured over a far smaller number of runs. The weighting factor, W_{bg} is calculated by:

$$W_{bg} = \frac{\text{No. good events in experiment data}}{\text{No. good events in shadow bar data}} \tag{6.3}$$

The background subtraction was performed by subtracting the weighted shadow bar distributions shown in Figure 6.5.1 and Figure 6.5.2 from the main experimental distributions shown in Figure 6.4.2 and Figure 6.4.3 respectively. In practice the subtraction was performed for each bin of the histograms individually and the new histogram was produced from the results. The value of each bin, bin_{bgs}, for the background subtracted data was calculated by:

$$bin_{bgs} = bin_{\phi} - W_{bg} bin_{SB} \tag{6.4}$$

where bin_{ϕ} is the bin value from the main experimental data in Figure 6.4.2 for charged particles and Figure 6.4.3 for neutrons, bin_{SB} is the bin value for the shadow bar data.

After the background subtraction was performed, the new azimuthal distributions can be seen in Figure 6.5.3 and Figure 6.5.4. The elliptic and directed flow can now be extracted from these distributions by fitting each plot with the Fourier expansion:

$$\frac{dN}{d\phi} = \frac{1}{2\pi}(1 + 2\sum_{n=1}^{2} v_n cos[n\phi]) \tag{2.3}$$

where ϕ is defined as the angle relative to the reaction plane:

$$\phi = \phi_{lab} - \phi_{RP}. \tag{6.5}$$

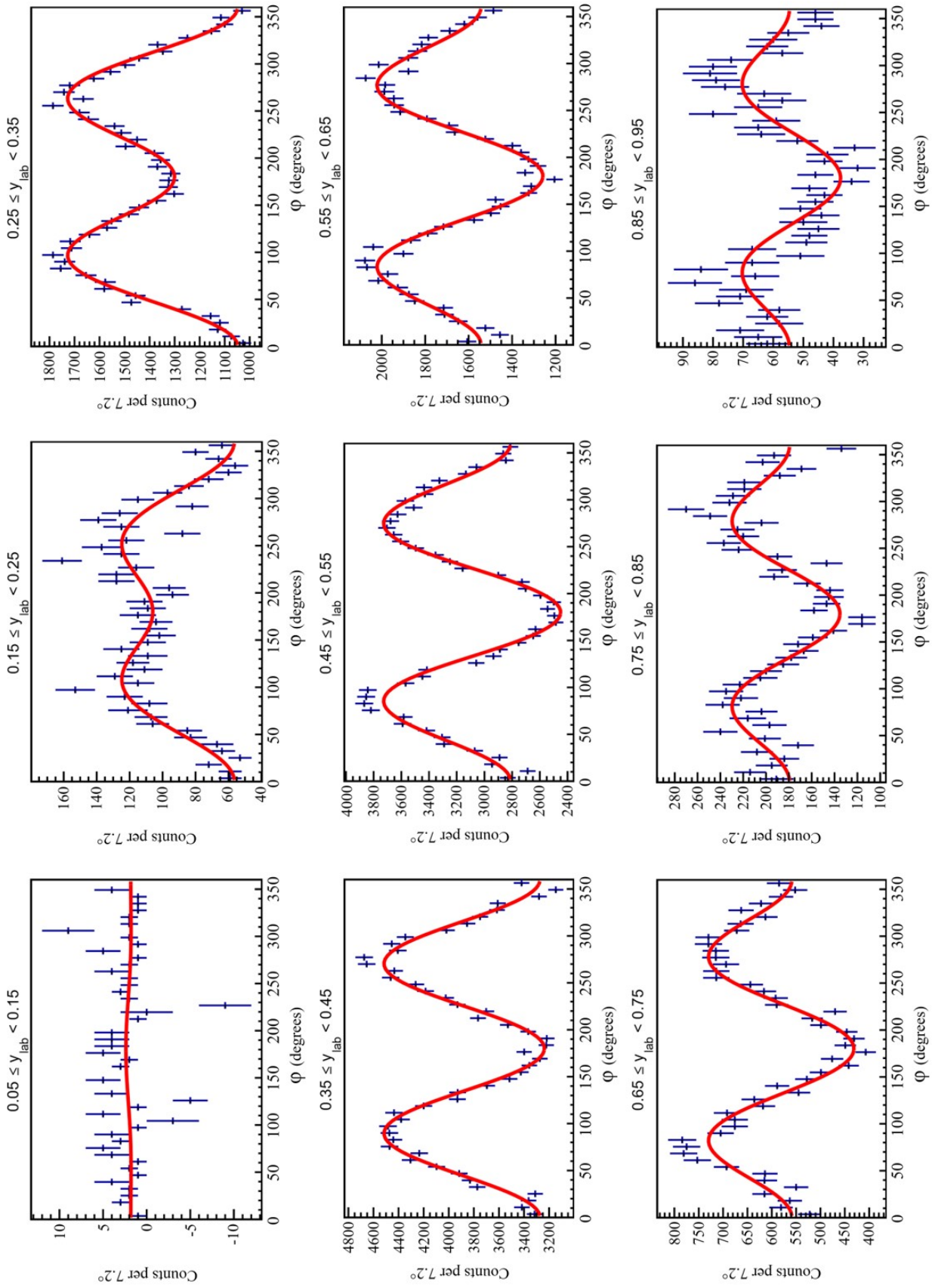

Figure 6.5.3: Azimuthal distributions obtained for charged particles detected in LAND in each rapidity range after correcting for the reaction plane bias and background subtraction. Angles are measured relative to the reaction plane. The y-axis for each plot is counts per 7.2°. The x-axis for each plot is the azimuthal angle relative to the reaction plane of the event.

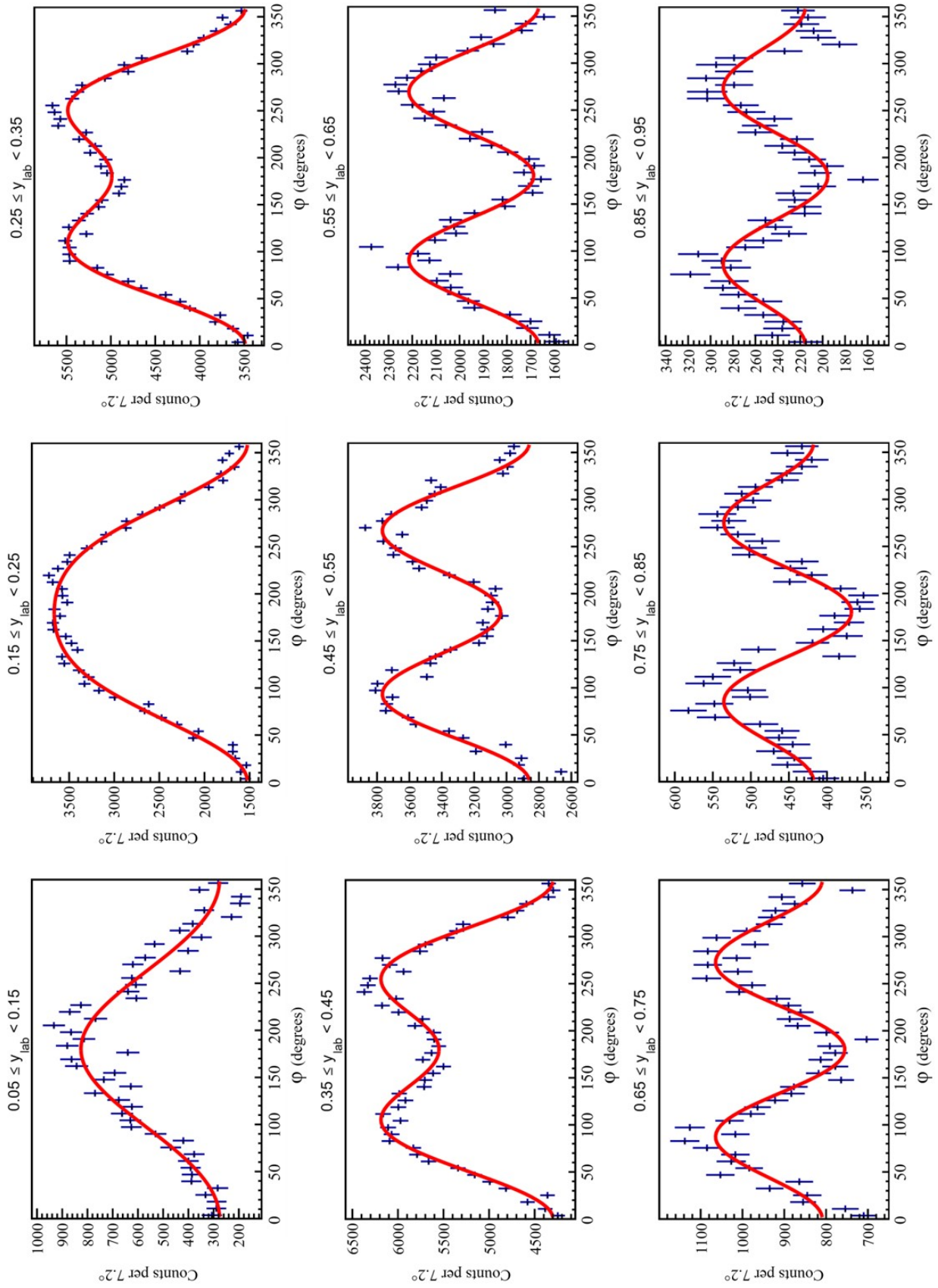

Figure 6.5.4: Azimuthal distributions obtained for neutral particles detected in LAND in each rapidity range after correcting for the reaction plane bias and background subtraction. Angles are measured relative to the reaction plane. The y-axis for each plot is counts per 7.2°. The x-axis for each plot is the azimuthal angle relative to the reaction plane of the event.

The strength of the directed flow is quantified by the parameter v_1 and the elliptic flow is given by v_2. The red line on the plots shows the Fourier expansion which is fitted to each plot.

6.6 Reaction Plane Dispersion

After the v_1 and v_2 values have been extracted from the Fourier fits they need to be corrected for an effect called reaction plane dispersion. This occurs because the reaction plane which is determined for an event is really just an estimate which is based on the distribution of a finite number of particles. These particles will be subject to statistical fluctuations which means that the determined value for the reaction plane, ϕ_{RP}, will differ from the true reaction plane, Φ_{RP}, by an amount $\Delta\phi_{RP}$. This error in the reaction plane determination results in the v_1 and v_2 values, which are extracted from the Fourier fits of the azimuthal distributions, being smaller than the true values [43].

In [43] it is demonstrated that the error in the reaction plane can be estimated for each event and used to determine a correction factor, $cos[n\Delta\phi]$, so as to recover the true values of the directed and elliptic flow parameters, $v_{1\Phi}$ and $v_{2\Phi}$:

$$v_{n\Phi} = \frac{v_n}{cos[n\Delta\phi]} \tag{6.6}$$

The uncertainty in the reaction plane is estimated by taking the particles used to determine the Q-vector, see Figure 2.2.1, and randomly separating them into two sub-events. These sub-events each contain half of the detected particles from the event and are used to find two Q-vectors, Q_I and Q_{II}. The difference between

these two Q-vectors is calculated for each event [64]:

$$\Delta\phi_R = \Delta\phi_I - \Delta\phi_{II} \tag{6.7}$$

The values of $\Delta\phi_R$ are then collected for all events and the fraction of events for which $\Delta\phi_R > 90^\circ$ is related to the quantity χ:

$$\frac{N(90^\circ < \Delta\phi_R < 180^\circ}{N(0^\circ < \Delta\phi_R < 180^\circ} = \frac{e^{(-\chi^2/2)}}{2} \tag{6.8}$$

In reference [43] it is shown that χ measures the accuracy of the reaction plane determination and can be used in conjunction with Figure 6.6.1 to determine the correction factors for the elliptic and directed flow.

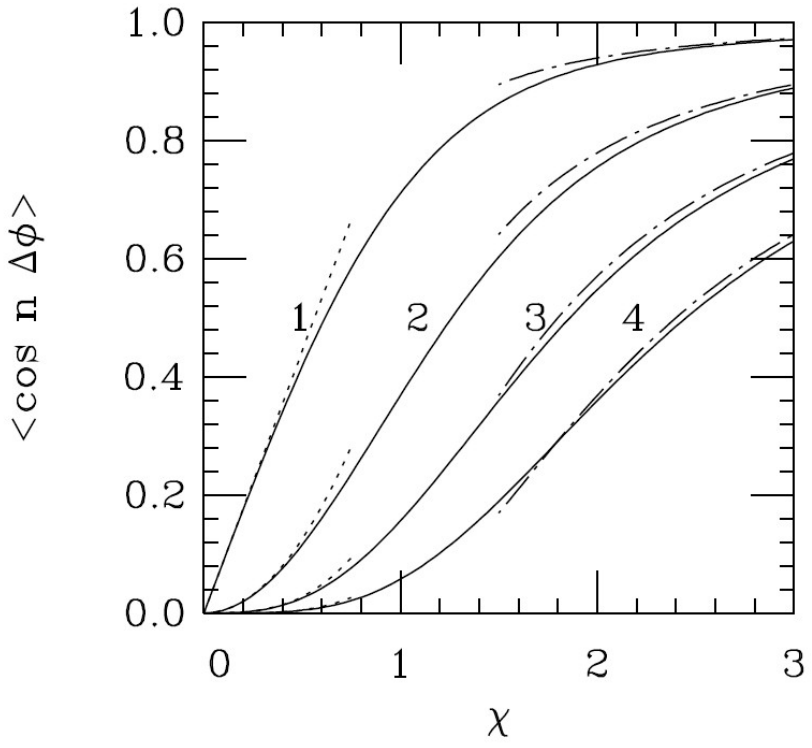

Figure 6.6.1: This plot shows the relationship between χ and the correction factors for the first four Fourier coefficients, v_1, v_2, v_3, and v_4. It was used to determine to correction factors for v_1 and v_2 in the analysis of the ASY-EOS data [43]. These Fourier coefficients are defined in the Fourier expansion (equation 2.3) which was used to fit the azimuthal particle distributions in Figure 6.5.3 and Figure 6.5.4.

Having extracted the strength of the directed and elliptic flow from the data the next step is to determine a value for γ by comparing the neutron to proton ratio of the elliptic flows to the UrQMD transport model predictions.

7 Results

7.1 Extracting Gamma

Equation 6.6 was used to recover the true values of the v_1 and v_2 and the adjusted v_1 and v_2 values were plotted as a function of normalized rapidity in Figure 7.1.1.

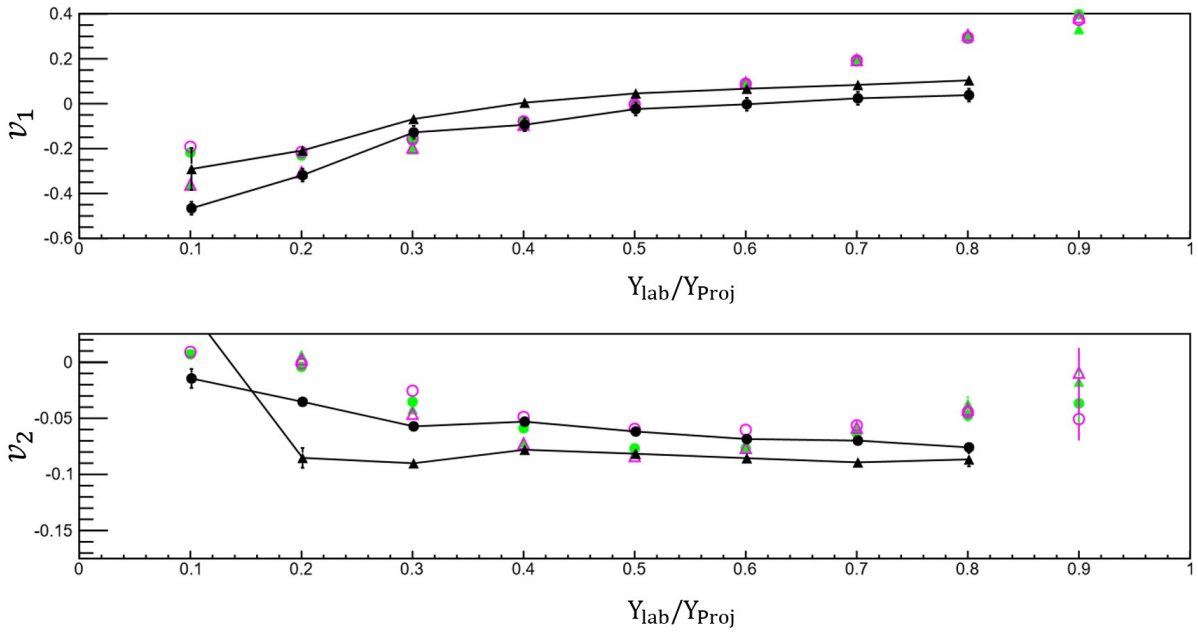

Figure 7.1.1: The top panel shows the v_1 against normalized rapidity for charged particles and neutrons. The charged particle data are represented by triangles and the neutron data by circles. The black points are the experimental data. The green and pink symbols are the theoretical predictions from UrQMD for hard ($\gamma = 0.5$) and soft ($\gamma = 1.5$) symmetry energy, respectively. The lower panel shows the same plot for v_2.

The experimental data give good agreement with the UrQMD predictions

around mid rapidity but deviates at low and high rapidity. The differences seen at low and high rapidity are likely due to a combination of poor statistics and the pollution of the data in these rapidity ranges due to the corrections that were applied to try and correct the TacQuila[17] time jumps. This procedure was discussed in section 4.6. If Figure 7.1.1 is compared to Figure 2.5.1 [53] from the earlier FOPI experiment it can be seen that the v_1 and v_2 values extracted from the ASY-EOS experiment are consistent around mid rapidity. Also note that the statistical uncertainties are reduced in the ASY-EOS data.

A value for γ can be extracted as a function of rapidity using the v_2 values from Figure 7.1.1. UrQMD simulations predict that the ratio of the v_2 values for neutrons and charged particles is sensitive to the strength of the nuclear symmetry energy. It is possible to extract a value for γ by calculating the ratio of the elliptic flow for neutrons and charged particles, v_2^n/v_2^{Ch}, and comparing it against the UrQMD predictions using a linear interpolation which is shown in Figure 7.1.2.

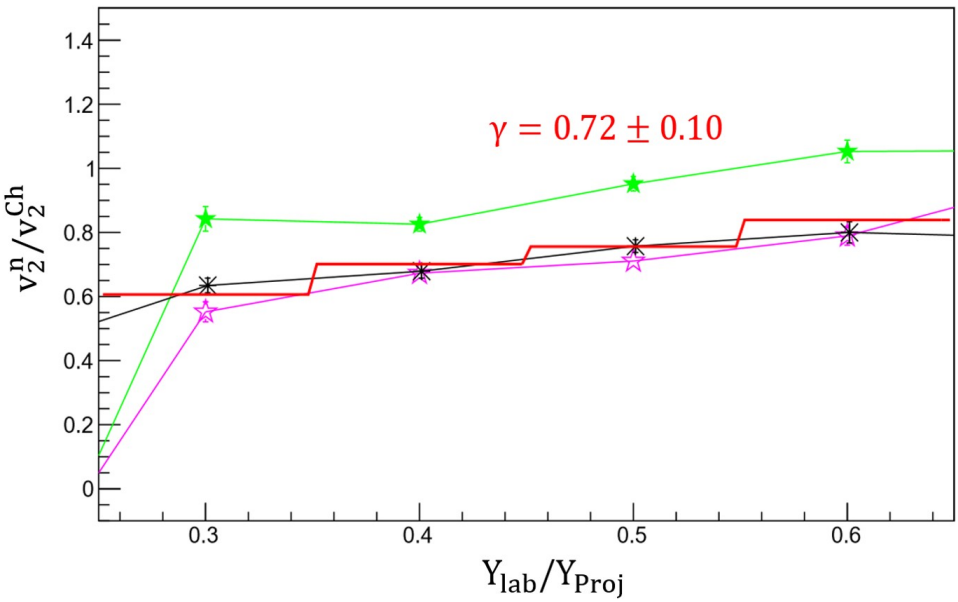

Figure 7.1.2: The plot shows the ratio of v_2 for hydrogen isotopes and neutrons as a function of normalized rapidity compared against the UrQMD model predictions. The UrQMD predictions for "soft" symmetry energy ($\gamma = 0.5$) and "stiff" symmetry energy ($\gamma = 1.5$) are represented by the green symbols and red symbols, respectively. The solid line is produced from a linear interpolation between the two UrQMD model predictions which is averaged over the 4 rapidity bins. This linear interpolations yields a value of $\gamma = 0.72 \pm 0.10$.

The results of this interpolation suggest a moderately soft symmetry energy with $\gamma = 0.72 \pm 0.10$, where $\Delta\gamma = 0.10$ is the statistical uncertainty returned by the analysis procedure.

It was also necessary to consider the systematic errors which were introduced by the corrections that were applied to the LAND data, which were described in 4.6. Most of the corrections were performed on hits which had suffered a 25ns time jump in one of its photomultipliers; these hits were easily identified and corrected because the position calculated from the time data (*post*) of such a hit was outside the physical dimensions of the LAND detector system.

However, a significant number of hits suffered identical 25ns jumps in both photomultipliers which meant that the apparent position of such a hit would be

correct because the effects of the 2 time jumps cancel out when calculating the value of *post*. This made it impossible to correctly identify all of the doubly corrected hits with the result that a significant fraction of these hits might not have been corrected. It was also expected that some uncorrupted hits would be erroneously shifted into higher or lower rapidity bands by the correction process.

The effect of the correction process on the extracted value of γ was investigated by applying the correction to different fractions of the hits which were identified as being doubly corrupted and extracting a value for γ in each case. The fraction of these doubly corrupted hits to which the correction was applied was varied between the limits of 40% and 100% and the range of values extracted for γ and the 1-σ error bars indicated a larger uncertainty of $\Delta\gamma = \pm 0.15$. This larger value of $\Delta\gamma$ was expected to include any systematic errors associated with the correction procedure.

This value of $\gamma = 0.72 \pm 0.15$ is significantly lower than the value determined in the analysis of the FOPI experiment (see Figure 2.5.2) but the values are still consistent and uncertainties are also reduced by at least a factor of 2 in the ASY-EOS data.

7.2 Time Integrated Flow

The initial results extracted gamma as a function of normalized rapidity and were consistent with the FOPI data in the mid rapidity regions. However problems caused by the time jumps in TacQuila, and their subsequent corrections, meant that data from the high and low rapidity regions could not be used to find a value for γ. This also casts uncertainty on the mid rapidity data because it is difficult to know what effect the corrections have had on the value of γ that was extracted from this region. With these issues in mind the data were re-analysed in order to extract a value of gamma which did not depend on the correction of the doubly

corrupted hits in LAND.

The new method of analysing the data involved integrating the extracted elliptic flow ratio (v_2^n/v_2^{Ch}) over a large time of flight window which should include all of the Au-Au reaction products and spectator particles. When analysing the data in this way it did not matter if the corrections had erroneously shifted low rapidity particles into a higher region or vice versa because the extracted value of gamma was independent of rapidity in this analysis method. All that mattered, with regards to the LAND corrections, was that the corrupted hits which returned wrong positions in LAND were corrected so that azimuthal distributions of neutrons and charged particles could be produced.

A new source of systematic error was introduced by this method of analysis because an upper limit needed to be chosen for the time of flight window used in the integration. This upper limit on the time of flight created a lower threshold for the energy of the neutrons which were included in the analysis. The degree of uncertainty introduced by the choice of the time of flight limit was investigated by varying the limit from 20 ns up to 90 ns and extracting γ values for each limit The variation of γ as a function of the upper TOF limit was used to quantify this systematic uncertainty. It should be noted that protons required at least 60 MeV in order to pass through the VETO paddles and leave a signal in LAND and a 60 MeV proton would have had a time of flight, from the target to LAND, of 49 ns. This means that the uncorrupted proton data should not have been affected by the any time of flight limit above this value.

The value for γ was extracted from this integrated flow analysis in the same way as described in the previous section except that the data were no longer divided into rapidity bands. The top panel in Figure 7.2.1 shows the v_2 ratios extracted by this method of analysis compared against new UrQMD simulations

for each chosen upper limit on the time of flight and the results of the linear interpolation between the UrQMD predictions are displayed on the lower panel. The extracted values for γ are unrealistically small at very low time of flight limits but the values start to become consistent with the γ values extracted in Figure 7.1.2 as the maximum time of flight limit was increased to include more of the hits that had been shifted to lower rapidity regions. The variation of γ and its 1-σ statistical error bars ($\Delta\gamma_{stat} = 0.10$) in the range from 60 ns to 90 ns is used to quantify the size of the total uncertainty on the extracted value of γ.

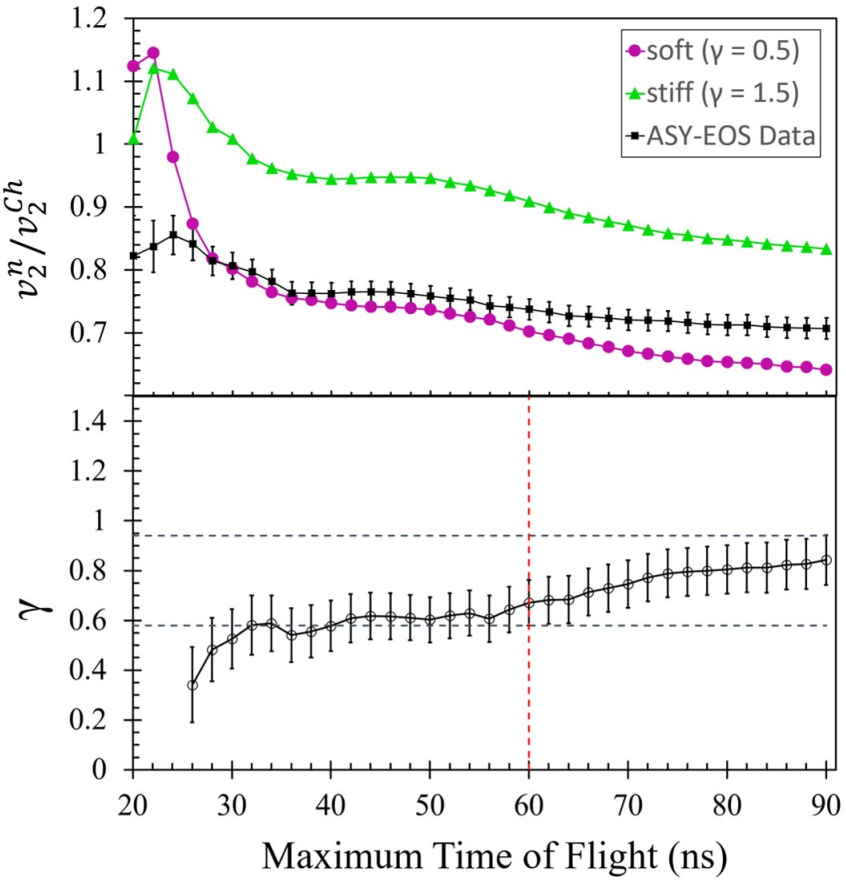

Figure 7.2.1: The top panel shows the time integrated elliptic flow ratios as a function of the upper limit on the time of flight window. Data are shown for collisions of ^{197}Au+^{197}Au at 400 MeV/nucleon, which had impact parameters smaller than 7.5 fm. The integrated flow ratios are displayed against the UrQMD predictions for "soft" ($\gamma = 0.5$) and "stiff" ($\gamma = 1.5$) formulations of the symmetry energy. The bottom panel shows the value of γ which was extracted from the experiment data by a linear interpolation between the two UrQMD predictions. Error bars represent the statistical uncertainties that were returned by the analysis routine.

This method of analysis yields a value of $\gamma = 0.76 \pm 0.18$ which is slightly higher than the value extracted from Figure 7.1.2 and moves the ASY-EOS result closer to the FOPI data. The top panel of Figure 7.2.1 shows how the value of gamma evolves as the integrated TOF range is increased and it can be seen that there is a significant increase in the γ value as the integration is extended to higher maximum TOF values. Particles with such large TOF values should not have such a significant effect on the elliptic flow ratio and so this observation is perhaps evidence of the effect of mid-rapidity particles which have been erroneously shifted to lower rapidity regions. This result was consistent with the value of $\gamma = 0.77 \pm 0.17$ which was extracted from the parallel analysis, performed by P.Russotto [65] (see Figure 7.2.2).

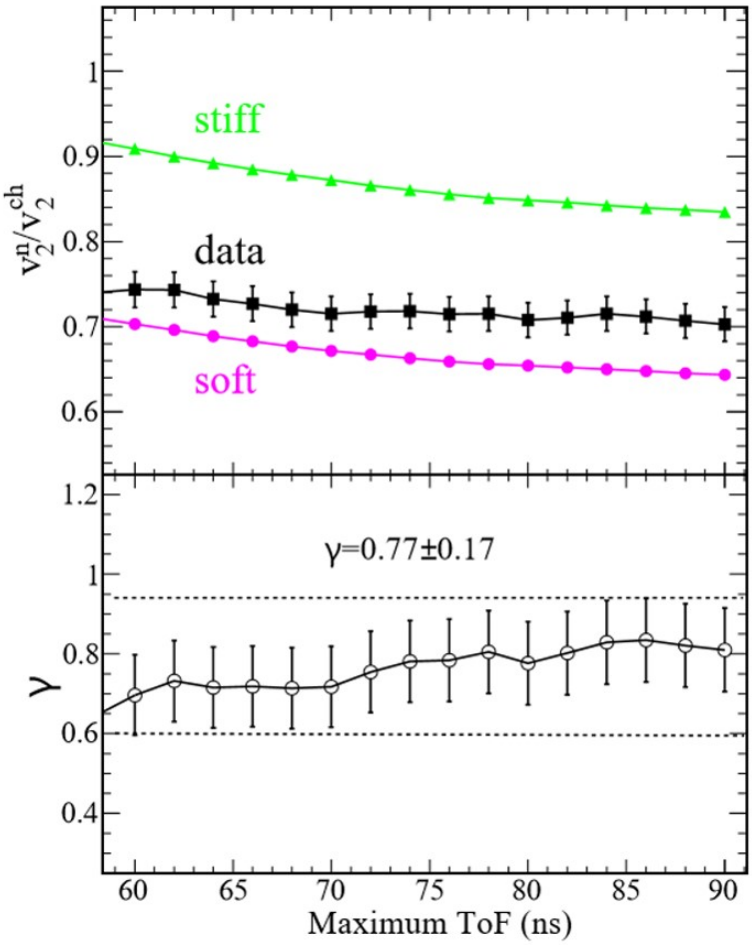

Figure 7.2.2: This figure is adapted from analysis performed by P.Russotto and is shown here for comparison against the results of my parallel analysis. The top panel shows the ratio of v_2 for neutrons and hydrogen isotopes against time of flight. The experiment data point shows the integrated v_2 ratio for upper TOF limits of 60 ns up to 90 ns. The results of the UrQMD simulations are shown alongside the experiment data. A linear interpolation was used to extract a value for gamma which is shown on the same scale in the lower panel of the figure.

A further correction was performed on the extracted value of γ to correct for a systematic error in which charged particles were misidentified as neutrons in LAND. These misidentifications occurred if a charged particle was not detected in the VETO but was recorded as a hit in the first plane of LAND. The most likely cause of this type of particle misidentification was a 1mm gap between the paddles of the VETO wall. This meant that approximately 1% of the area of the first plane of LAND did not have a VETO paddle directly in front of it and so

any charged particles which were incident on these areas would not leave a signal in the VETO and would therefore be identified as a neutron. Such a misidentification would tend to decrease the difference between v_2^n and v_2^{Ch} and shift the elliptic flow ratio closer to a value of 1. This would increase the measured value of the elliptic flow ratio and cause an increase in the extracted value of γ, which would make the density dependence of the symmetry energy appear stiffer than it should. This misidentification could cause an increase in the extracted value of γ of between $\Delta\gamma = +0.03$ and $\Delta\gamma = +0.07$. The extracted value for γ was therefore reduced by 0.05 ± 0.02 to correct for this systematic error leading to a final value of $\gamma = 0.72 \pm 0.19$.

Other sources of systematic error, such as neutrons being detected in the VETO [60] and nuclear charge-exchange reactions [66] [67], were considered but these processes are much less likely to occur and were not expected to contribute significantly to the systematic uncertainty.

8 Conclusions and Perspectives

The work presented in this thesis has focused on the measurement of the elliptic flow ratio of neutrons and light charged particles (v_2^n/v_2^{Ch}) with the aim of placing more stringent constraints on the strength of the nuclear symmetry energy at supra-saturation densities. The magnitude of the elliptic flow was quantified by the v_2 coefficient of the Fourier expansion which was used to fit the azimuthal distributions of the neutrons and charged particles which were produced from heavy ion collisions of ^{197}Au $+^{197}$ Au at an energy of 400 AMeV. The process of extracting the elliptic flow was complicated by the 25ns jumps which randomly corrupted the timing data from the LAND detector. These timing jumps necessitated the development of procedures to correct the corrupted data which extended the analysis process by several years and led to a significant increase in the total error on the measured value of the v_2 ratio of neutrons over charged particles.

The ASY-EOS measurement of v_2^n/v_2^{Ch} was compared against the predictions of UrQMD simulations [45] [46] [47] and a value of $\gamma = 0.72 \pm 0.19$ was extracted which has allowed more stringent constraints to be placed on the symmetry energy at densities up to 2 times the saturation density, as illustrated in Figure 8.0.1. This value is consistent with the earlier FOPI measurement of $\gamma = 0.9 \pm 0.4$ and confirms the moderately soft to linear density dependence of the nuclear symmetry energy. The ASY-EOS result is deduced from a much greater volume of data

than the FOPI experiment and this has reduced the statistical uncertainty to $\Delta\gamma_{stat} = \pm 0.10$, compared to the FOPI statistical error of $\Delta\gamma_{stat} = \pm 0.27$. The results from the ASY-EOS experiment are consistent with several sub-saturation density studies of the symmetry energy which are shown in Figure 8.0.1. These results also corroborate the conclusion of the FOPI data that the "super-soft" and "super-stiff" behaviour of the symmetry energy suggested by pion ratio studies [68] [69] can be ruled out.

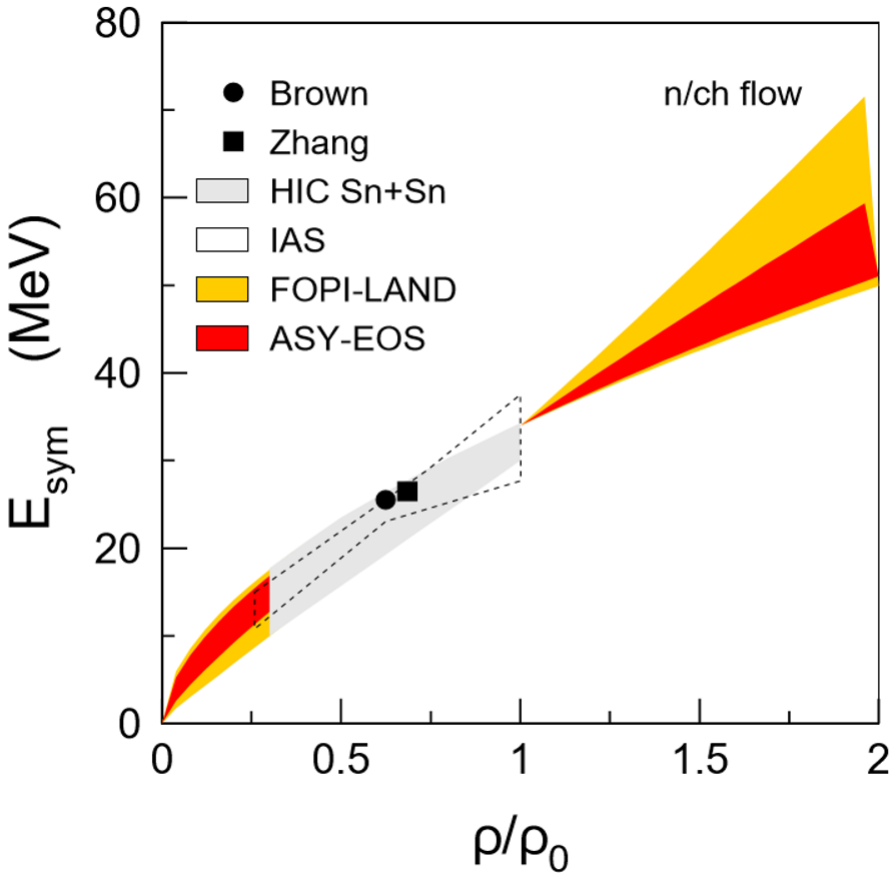

Figure 8.0.1: This plot shows the constraints placed on the symmetry energy from the ASY-EOS experiment compared against the constraints from the FOPI experiment. The plot also shows constraints on the symmetry energy at sub-saturation densities that were deduced from studies of, ^{112}Sn + ^{124}Sn collisions (grey region) [11], isobaric analog states (dashed region) [70], and neutron skin thickness measurements (black symbols) [71] [72]. For clarity, the ASY-EOS and FOPI results are not shown in the interval $0.3 < \rho/\rho_0 < 1.00$. This plot is adapted from the ASY-EOS results paper [65].

The results of the ASY-EOS analysis suggest values for the slope parameter of the symmetry energy at saturation densities of $L = 72 \pm 13$ MeV and a symmetry pressure of $p_0 = \frac{\rho_0 L}{3} = 3.8 \pm 0.7$ MeV/fm^{-3} ($6.1 \pm 1.1 \times 10^{32}$ Pa). This corresponds to the pressure of pure neutron matter at saturation densities and should be higher than the pressure in a neutron star which contains a small fraction of protons. The pressure deduced from the ASY-EOS results is consistent with the estimate for the pressure in a neutron star, deduced from equilibrium yields [73], of 34 MeVfm^{-3} for neutron star matter with a 5% proton fraction. These results are also consistent with the estimates of neutron star radii presented in references [27] and [3] and with recent measurements of neutron star radii [13]. These pressure estimates are only speculative at present but the agreement between the various sources does suggest that there is the potential for making pressure measurements using heavy ion collisions in the future as improved transport models become available [74]. Some recent experiments have investigated short range correlations in the nucleus [75] [76] and the incorporation of such interactions into transport codes could improve the transport model descriptions of heavy ion collisions [77].

In future studies it would be useful to compare experimental results against a range of different transport model predictions in an effort to work towards model-independent constraints on the symmetry energy at high densities [47]. It should be noted that more recent transport models were available [78] [79] for the analysis of the ASY-EOS data but the version of UrQMD used in the FOPI experiment was used again so that the two results could be directly compared.

The results of the ASY-EOS experiment make a strong case for extending the study of neutron and charged particle flows to other collision systems at higher energies in order to place tighter constraints on the density dependence of the nuclear symmetry energy. Any such future experiments will benefit from the new

R^3B experimental setup [80] and the improved capabilities of the NeuLAND detector [81] which is currently being constructed. Furthermore the FAIR facility, currently under construction in Darmstadt (Germany) [82], should be able to produce heavy ion collision systems capable of probing the symmetry energy at densities greater than 3 times the saturation density. FAIR will also be able to produce radioactive beams which should make it possible to study observables, such as double differential flow [83] [73], that are expected to be more sensitive to the effects of the symmetry energy.

List of Figures

Bibliography

[1] R. Lemmon, P. Russotto, *et al.*, "Asyeos experiment beam time request," *https://192.84.151.50/joomla/index.php?option=com$_c$ontentview = articleid = 85Itemid = 80, 2008.*

[2] J. Lattimer and M. Prakash, "Nuclear matter and its role in supernovae, neutron stars and compact object binary mergers," *Phys. Rep.*, vol. 333, p. 121, 2000.

[3] J. Lattimer and M. Prakash, "Neutron star structure and the equation of state," *The Astrophysical Journal*, vol. 550, p. 426, 2001.

[4] J. Lattimer and M. Prakash, "The physics of neutron stars," *Science*, vol. 304, p. 536, 2004.

[5] P. Danielewicz *et al.*, "Determination of the equation of state of dense matter," *Science*, vol. 298, pp. 1592–1596, 2002.

[6] J. Lattimer and Y. Lim, "Constraining the symmetry parameters of the nuclear interaction," *The Astrophysical Journal*, vol. 771, p. 51, 2013.

[7] M. Kortelainen *et al.*, "Nuclear energy density optimization," *Phys. Rev. C*, vol. 82, p. 024313, 2010.

[8] L.-W. Chen *et al.*, "Density slope of the nuclear symmetry energy from the neutron skin thickness of heavy nuclei," *Phys. Rev. C*, vol. 82, p. 024321, 2010.

[9] J. Piekarewicz *et al.*, "Electric dipole polarizability and the neutron skin," *Phys. Rev. C*, vol. 85, p. 041302, 2012.

[10] L. Trippa *et al.*, "Giant dipole resonance as a quantitative constraint on the symmetry energy," *Phys. Rev. C*, vol. 77, p. 061304, 2008.

[11] B. Tsang *et al.*, "Constraints on the density dependence of the symmetry energy," *Phys. Rev. Lett.*, vol. 102, p. 122701, 2009.

[12] A. Steiner *et al.*, "The equation of state from observed masses and radii of neutron stars," *The Astrophysical Journal*, vol. 722, p. 33, 2010.

[13] T. Guver and F. Ozel, "The mass and the radius of the neutron star in the transient low-mass x-ray binary saxj1748.9-2021," *The Astrophysical Journal Letters*, vol. 765, p. 1, 2013.

[14] K. Hebeler *et al.*, "Constraints on neutron star radii based on chiral effective field theory interactions," *Phys. Rev. Lett.*, vol. 105, p. 161102, 2010.

[15] S. Gandolfi *et al.*, "Maximum mass and radius of neutron stars, and the nuclear symmetry energy," *Phys. Rev. C*, vol. 85, p. 032801, 2012.

[16] P. Russotto *et al.*, "The asy-eos experiment at gsi: investigating the symmetry energy at supra-saturation densities," *Journal of Physics: Conference Series*, vol. 420, p. 012092, 2013.

[17] W. Trautmann and H. Wolter, "Elliptic flow and the symmetry energy at supra-saturation density," *Journal of Modern Physics E*, vol. 21, p. 6, 2012.

[18] X. Zhigang *et al.*, "Circumstantial evidence for a soft nuclear symmetry energy at suprasaturation densities," *Phys. Rev. Lett.*, vol. 102, p. 062502, 2009.

[19] F. Zhao-Qing and J. Gen-Ming, "Probing high-density behavior of symmetry energy from pion emission in heavy-ion collisions," *Phys. Lett. B*, vol. 683, p. 140, 2010.

[20] T. Li *et al.*, "Isotopic dependence of the giant monopole resonance in the Even-A $^{112-124}$Sn isotopes and the asymmetry term in nuclear incompressibility," *Phys. Rev. Lett.*, vol. 99, p. 162503, 2007.

[21] A. Klimkiewicz *et al.*, "Nuclear symmetry energy and neutron skins derived from pygmy dipole resonances," *Phys. Rev. C*, vol. 76, p. 051603, 2007.

[22] M. Tsang *et al.*, "Isospin diffusion and the nuclear symmetry energy in heavy ion reactions," *Phys. Rev. Lett.*, vol. 92, p. 062701, 2004.

[23] M. Tsang *et al.*, "Isotopic scaling in nuclear reactions," *Phys. Rev. Lett.*, vol. 86, p. 5023, 2001.

[24] J. Iglio *et al.*, "Symmetry energy and the isoscaling properties of the fragments produced in ^{40}Ar, ^{40}Ca+^{58}Fe, ^{58}Ni reactions at 25, 33, 45, and 53 MeV/nucleon," *Phys. Rev. C*, vol. 74, p. 024605, 2006.

[25] M. Tsang *et al.*, "Constraints on the symmetry energy and neutron skins from experiments and theory," *Phys. Rev. C*, vol. 86, p. 015803, 2012.

[26] B. Brown, "Neutron radii in nuclei and the neutron equation of state," *Phys. Rev. Lett.*, vol. 85, p. 5296, 2000.

[27] J. Lattimer and A. Steiner, "Constraints on the symmetry energy using the mass-radius relation of neutron stars," *Eur. Phys. J*, vol. A50, p. 40, 2014.

[28] M. Famiano *et al.*, "Neutron and proton transverse emission ratio measurements and the density dependence of the asymmetry term of the nuclear equation of state," *Phys. Rev. Lett.*, vol. 97, p. 052701, 2006.

[29] B.-A. Li and L. Chen, "Equation of state of asymmetric nuclear matter and collisions of neutron-rich nuclei," *Phys. Rev. Lett.*, vol. 78, p. 1644, 1997.

[30] B.-A. Li *et al.*, "Double neutron/proton ratio of nucleon emissions in isotopic reaction systems as a robust probe of nuclear symmetry energy," *Phys. Lett. B*, vol. 634, p. 378, 2006.

[31] B.-A. Li *et al.*, "Single and double $\pi-/\pi+$ ratios in heavy-ion reactions as probes of the high-density behavior of the nuclear symmetry energy," *Phys. Rev. C*, vol. 73, p. 051601, 2006.

[32] B.-A. Li, "Neutron-proton differential flow as a probe of isospin-dependence of nuclear equation of state," *Phys. Rev. Lett.*, vol. 85, p. 4221, 2000.

[33] B.-A. Li *et al.*, "Proton differential elliptic flow and the isospin dependence of the nuclear equation of state," *Phy. Rev. C*, vol. 64, p. 054604, 2001.

[34] B.-A. Li, "Probing the high density behavior of the nuclear symmetry energy with high energy heavy-ion collisions," *Phys. Rev. Lett.*, vol. 88, p. 192701, 2002.

[35] G.-C. Yong *et al.*, "Double neutron-proton differential transverse flow as a probe for the high density behavior of the nuclear symmetry energy," *Phys. Rev. C*, vol. 74, p. 064617, 2006.

[36] V. Greco *et al.*, "Relativistic effects in the search for high density symmetry energy," *Phys. Lett. B*, vol. 562, p. 215, 2003.

[37] B.-A. Li, "Observable effects of symmetry energy in heavy-ion collisions at intermediate energies," *Phys. Rev. C*, vol. 69, p. 034614, 2004.

[38] G.-C. Yong *et al.*, "Single and double $\pi-/\pi+$ ratios in heavy-ion reactions as probes of the high-density behavior of the nuclear symmetry energy," *Phys. Rev. C*, vol. 73, p. 034603, 2006.

[39] G. Ferini *et al.*, "Isospin effects on subthreshold kaon production at intermediate energies," *Phys. Rev. Lett.*, vol. 97, p. 202301, 2006.

[40] B.-A. Li *et al.*, "Probing the isospin dependence of the in-medium nucleon-nucleon cross sections with radioactive beams," *Phys. Rev. C*, vol. 71, p. 054907, 2005.

[41] H. Gustafsson *et al.*, "Collective flow observed in relativistic nuclear collisions," *Physical Review Letters*, vol. 52, pp. 1590–1593, 1984.

[42] A. Andronic *et al.*, "Systematics of stopping and flow in au+au collisions," *European Physical Journal A*, vol. 30, pp. 31–46, 2006.

[43] J.-Y. Ollitrault, "Reconstructing azimuthal distributions in nucleus-nucleus collisions," *arxiv*, vol. 9711003, p. v2, 2008.

[44] S. Voloshin *et al.*, "Collective phenomena in non-central nuclear collisions," *Landolt-Bornstein - Group I Elementary Particles, Nuclei and Atoms*, vol. 23, pp. 293–333, 2010.

[45] Q. Li *et al.*, "Probing the density dependence of the symmetry potential in intermediate-energy heavy ion collisions," *Journal of Physics G*, vol. 31, p. 1359, 2005.

[46] Q. Li *et al.*, "Probing the equation of state with pions," *Journal of Physics G*, vol. 32, p. 151, 2006.

[47] Q. Li *et al.*, "Medium modifications of the nucleonnucleon elastic cross section in neutron-rich intermediate energy hics," *Journal of Physics G*, vol. 32, p. 407, 2006.

[48] S. Bass *et al.*, "Microscopic models for ultrarelativistic heavy ion collisions," *Prog. Part. Nucl. Phys.*, vol. 41, p. 255, 1998.

[49] Q. Li and M. Bleicher, "A model comparison of resonance lifetime modifications, a soft equation of state and non-gaussian effects on correlations at fair/ags energies," *Journal of Physics G*, vol. 36, p. 015111, 2009.

[50] Y. Leifels *et al.*, "Exclusive studies of neutron and charged particle emission in collisions of ^{197}Au+^{197}Au at 400 MeV/nucleon," *Phys. Rev. Lett.*, vol. 71, p. 963, 1993.

[51] W. Reisdorf *et al.*, "Central collisions of au on au at 150, 250 and 400 A MeV," *Nuclear Physics A*, vol. 612, p. 493, 1997.

[52] D. Lambrecht *et al.*, "Energy dependence of collective flow of neutrons and protons in ^{197}Au +^{197} Au collisions," *Z Phys. A*, vol. 350, p. 115, 1994.

[53] P. Russotto *et al.*, "Symmetry energy from elliptic flow in ^{197}Au +^{197} Au," *Phys Lett B*, vol. 697, pp. 471–476, 2011.

[54] Q. Li *et al.*, "Probing the momentum-dependent medium modifications of the nucleon-nucleon elastic cross section," *Modern Physics Letters A*, vol. 25, p. 669, 2010.

[55] M. Centelles *et al.*, "Nuclear symmetry energy probed by neutron skin thickness of nuclei," *Phys. Rev. Lett.*, vol. 102, p. 122502, 2009.

[56] A. Andronic *et al.*, "Excitation function of elliptic flow in Au + Au collisions and the nuclear matter equation of state," *Physics Letters B*, vol. 612, pp. 173–180, 2005.

[57] A. Schuttauf *et al.*, "Universality of spectator fragmentation at relativistic bombarding energies," *Nuclear Physics A*, vol. 607, pp. 457–486, 1996.

[58] D. Sarantites *et al.*, "The microball design, instrumentation and response characteristics of a 4π-multidetector exit channel-selection device for spec-

troscopic and reaction mechanism studies with gammasphere," *Nuclear Instrumentation and Methods A*, vol. 381, pp. 418–432, 1996.

[59] A. Pagano *et al.*, "Fragmentation studies with the chimera detector at lns in catania: recent progress," *Nuclear Physics A*, vol. 734, pp. 504–511, 2004.

[60] T. Blaich *et al.*, "A large area detector for high-energy neutrons," *Nuclear Instruments and Methods A*, vol. 314, pp. 136–154, 1992.

[61] J. Lukasik *et al.*, "Kratta, a versatile triple telescope array for charged reaction products," *Nuclear Instruments and Methods A*, vol. 709, pp. 120–128, 2013.

[62] C. Ceasar, *Beyond the Neutron Drip-Line: Superheavy Oxygen Isotopes*. PhD thesis, Vom Fachbereich Physik der Technischen Universitat Darmstadt, 2012.

[63] "R3BRoot Homepage," *http://fairroot.gsi.de/*.

[64] J.-Y. Ollitrault, "Determination of the reaction plane in ultrarelativistic nuclear collisions," *Phys. Rev.*, vol. D48, p. 1132, 1993.

[65] P. Russotto *et al.*, "Results of the asy-eos experiment at gsi: The symmetry energy at suprasaturation density," *Physics Review C*, vol. 94, p. 034608, 2016.

[66] B. Anderson *et al.*, "^{12}C(p,n)^{12}N reaction at 135 MeV," *Physics Review C*, vol. 54, p. 237, 1996.

[67] I. Tanihata *et al.*, "Observations of large enhancement of charge exchange cross sections with neutron-rich carbon isotopes," *arXiv:1512.00590*, 2015.

[68] Z. Xiao *et al.*, "Circumstantial evidence for a soft nuclear symmetry energy at suprasaturation densities," *Physical Review Letters*, vol. 102, p. 062502, 2009.

[69] Z.-Q. Feng *et al.*, "Probing high-density behaviour of symmetry energy from pion emission in heavy-ion collisions," *Physical Letters B*, vol. 683, p. 140, 2010.

[70] P. Danielewicz and J. Lee, "Symmetry energy II: Isobaric analog states," *Nuclear Physics A*, vol. 922, p. 1, 2014.

[71] B. Brown, "Constraints on the skyrme equations of state from properties of doubly magic nuclei," *Physical review letters*, vol. 111, p. 232502, 2013.

[72] Z. Zhang and L.-W. Chen, "Constraining the symmetry energy at subsaturation densities using isotope binding energy difference and neutron skin thickness," *Physics Letters B*, vol. 726, p. 234, 2013.

[73] B.-A. Li *et al.*, "Recent progress and new challenges in isospin physics with heavy-ion reactions," *Physics Reports*, vol. 464, p. 113, 2008.

[74] J. Xu *et al.*, "Understanding transport simulations of heavy-ion collisions at 100 a and 400 amev: Comparison of heavy-ion transport codes under controlled conditions," *Physical review C*, vol. 93, p. 044609, 2016.

[75] R. Subedi *et al.*, "Probing cold dense nuclear matter," *Science*, vol. 320, p. 1476, 2008.

[76] O. Hen *et al.*, "Momentum sharing in imbalanced fermi systems," *Science*, vol. 346, p. 614, 2014.

[77] O. Hen *et al.*, "Symmetry energy of nucleonic matter with tensor correlations," *Physical review C*, vol. 91, p. 025803, 2015.

[78] Y. Wang *et al.*, "Collective flow of light particles in au + au collisions at intermediate energies," *Physical Review C*, vol. 89, p. 034606, 2014.

[79] Y. Wang *et al.*, "Constraining the high-density nuclear symmetry energy with the transverse-momentum-dependent elliptic flow," *Physical Review C*, vol. 89, p. 044603, 2014.

[80] "R3B Homepage," *http://www.gsi.de/r3b*.

[81] "Technical Report for the Design, Construction and Commissioning of NeuLAND," *http://www.fair-center.eu/fileadmin/fair/publications*$_e$*xp/*$NeuLAND - TDR - Web.pdf$.

[82] G. Rosner, "Future facility: FAIR at GSI," *Nuclear physics B - Proceedings supplements*, vol. 167, p. 77, 2007.

[83] P. Wu, *An exploratory study of the nuclear equation of state and the symmetry energy at supra-saturation densities using Au + Au collisions*. PhD thesis, University of Liverpool, 2011.